

# POLITECNICO DI TORINO

Master's Degree in Aerospace Engineering



**Politecnico  
di Torino**

Master's Degree Thesis

## Topology Optimization of Origami Structures based on Crease Pattern and Axial Rigidity

Supervisors

Prof. Alfonso PAGANI

Prof. Afzal SULEMAN

Prof. Abdolrasoul SOHOULI

Candidate

Vincenzo CRETELLA

October 2023



# Abstract

Origami structures exhibit desirable stowage properties for application in deployable space structures. This work presents a description of their kinematics and proposes a design method using topology optimization. Using a truss model, the objective is to find the optimal configuration of the trusses based on axial rigidity and the crease pattern that maximizes the displacement at set locations, under prescribed forces and boundary conditions. First, a linear method is used to determine small strain and small rotation mechanics of flexible origami, with the aim of studying the behavior at the initiation of folding. Subsequently, a nonlinear method is implemented to consider large displacement and large rotation mechanics. To carry out the optimization process, constraints on the number of active fold lines and on the axial rigidity distribution are applied. Previous studies on topology optimization of origami structures have considered only folding and bending in their analyses. Here it is shown that, including the axial rigidity as a design variable, multi-material topology optimization can be achieved and new promising origami designs can be discovered.

# Sommario

Le strutture origami presentano buone proprietà per l'applicazione in strutture dispiegabili nello spazio. Il lavoro corrente contiene una descrizione della cinematica degli origami e propone un metodo di progettazione basato sull'ottimizzazione topologica, utilizzando un modello trave per caratterizzare tali strutture. L'obiettivo è ottenere la configurazione ottimale delle travi in base alla rigidità assiale e la distribuzione delle linee di piegatura che massimizza lo spostamento in posizioni prestabilite della struttura, considerando note le forze e le condizioni al contorno. Inizialmente, viene applicato un metodo lineare per studiare la meccanica delle piccole deformazioni e delle piccole rotazioni in origami flessibili, con lo scopo di studiare il comportamento all'inizio del piegamento. Successivamente, viene implementato un metodo non lineare per considerare la meccanica dei grandi spostamenti e delle grandi rotazioni, tipica degli origami. Per eseguire il processo di ottimizzazione topologica, vengono applicati vincoli sul numero di pieghe attive e sulla distribuzione della rigidità assiale. Precedenti studi riguardanti l'ottimizzazione topologica degli origami tengono conto, nella loro analisi, solo del movimento di piegatura e di flessione in tali strutture. In questo lavoro viene dimostrato che, includendo la rigidità assiale come variabile di progetto, è possibile ottenere un'ottimizzazione topologica multi-materiale che permette di scoprire nuove configurazioni promettenti per le strutture origami.

# Acknowledgements

To begin, I would like to thank my supervisors, who have contributed with their tireless support to the present paper. Prof. Alfonso Pagani followed me with availability and kindness, providing me with the necessary support and practical suggestions. Prof. Afzal Suleman, with his advice and constructive criticism, has always intervened decisively in my moments of difficulty, since the choice of the topic. Prof. Abdolrasoul Sohoulı has guided me step by step with great patience during these months, imparting knowledge that I will treasure for my future. Finally, I would like to thank Prof. Kazuko Fuchi for her crucial intervention and for providing me with the codes that I modified to realize my work.

# Ringraziamenti

Per cominciare, vorrei ringraziare i miei relatori, che hanno contribuito con il loro instancabile supporto, alla stesura del presente elaborato. Il Prof. Alfonso Pagani mi ha seguito con disponibilità e gentilezza, fornendomi il supporto necessario e suggerimenti pratici. Il Prof. Afzal Suleman, con i suoi consigli puntuali e le sue critiche costruttive è sempre intervenuto in maniera risolutiva nei miei momenti di difficoltà, fin dalla scelta dell'argomento. Il Prof. Abdolrasoul Sohoulì mi ha guidato con grande pazienza passo dopo passo nel corso di questi mesi, trasmettendomi conoscenze che custodirò per il mio futuro. Infine vorrei ringraziare la Prof.ssa Kazuko Fuchi per il suo intervento cruciale e per avermi fornito i codici da me modificati per la realizzazione del mio lavoro.

# Table of Contents

<b>List of Tables</b>	VIII
<b>List of Figures</b>	X
<b>1 Introduction to Origami Structures</b>	<b>2</b>
1.1 Introduction . . . . .	2
1.2 Basics of Origami . . . . .	4
1.3 Advantages and Disadvantages of Origami Structures . . . . .	6
1.4 Space Applications of Origami Structures . . . . .	7
1.5 Objectives . . . . .	13
1.6 Chapters Overview . . . . .	14
<b>2 Kinematics of Origami Structures With Creased Folds</b>	<b>15</b>
2.1 Origami Structures With Creased Folds . . . . .	15
2.2 Fold Pattern Description . . . . .	18
2.3 Kinematic Constraints . . . . .	21
2.3.1 Developability Constraint . . . . .	21
2.3.2 Loop Closure Constraint . . . . .	21
2.4 Folding Map Formulation . . . . .	24
2.4.1 Parameters for the folding map formulation . . . . .	24
2.4.2 Working Principles of the Folding Map Formulation . . . . .	27
2.5 Computational Implementation of the Model . . . . .	28
2.5.1 Iterative Process . . . . .	29
2.6 Simulation Example of the Kinematic Model . . . . .	30
<b>3 Topology Optimization Based on Linear Analysis</b>	<b>34</b>
3.1 Introduction on Topology Optimization . . . . .	34
3.2 Linear truss model . . . . .	36
3.3 Optimization Methods . . . . .	37
3.3.1 Fold Constraint . . . . .	37
3.3.2 Truss Model with Axial Rigidity as Design Variable . . . . .	38

3.4	Optimization Framework . . . . .	40
3.4.1	Sensitivity analysis . . . . .	42
3.5	Numerical Examples . . . . .	44
3.5.1	Chomper Fold Pattern . . . . .	44
3.5.2	Zigzag Structure . . . . .	47
3.5.3	Miura-Ori Fold Pattern . . . . .	49
<b>4</b>	<b>Topology Optimization Based on Nonlinear Analysis</b>	<b>54</b>
4.1	Nonlinear truss model . . . . .	54
4.2	Principle of Minimum Energy . . . . .	57
4.3	Linearization of the nonlinear problem . . . . .	58
4.4	Optimization Framework . . . . .	59
4.4.1	Sensitivity analysis . . . . .	62
4.5	Numerical Examples . . . . .	63
4.5.1	Chomper fold pattern . . . . .	64
4.5.2	Square Twist fold pattern . . . . .	71
<b>5</b>	<b>Conclusions and Future Works</b>	<b>75</b>
5.1	Conclusions . . . . .	75
5.2	Future Works . . . . .	76
	<b>Bibliography</b>	<b>78</b>
<b>A</b>	<b>Inclusion of a Genetic Algorithm to the Optimization Process</b>	<b>87</b>
<b>B</b>	<b>Origami Structures with Tessellation Patterns</b>	<b>91</b>
<b>C</b>	<b>Critical Points Analysis in Origami Structures</b>	<b>94</b>
<b>D</b>	<b>Equilibrium Bifurcations Analysis in Origami Structures</b>	<b>97</b>
<b>E</b>	<b>Topology Optimization for Auxetic Origami Structures</b>	<b>102</b>



# List of Tables

3.1	Final configurations of the Chomper pattern (design variable: $\alpha$ ). Dashed lines in Optimized Crease Pattern: active folds with $G = G_{soft} = 10^2 Pa \cdot m^2$ . . . . .	46
3.2	Final configurations of the zigzag structure. Dashed lines in Optimized Crease Pattern: active folds with $G = G_{soft} = 10^2 Pa \cdot m^2$ . Magenta and black lines in Axial Rigidity Distribution: $EA = EA_{min} = 10^4 Pa \cdot m^2$ and $EA = EA_0 = 10^8 Pa \cdot m^2$ . . . . .	48
3.3	Final configurations of the Miura-Ori pattern (design variable: $\alpha$ ). Dashed lines in Optimized Crease Pattern: active folds with $G = G_{soft} = 10^2 Pa \cdot m^2$ . . . . .	51
3.4	Final configurations of the Miura-Ori pattern. Dashed lines in Optimized Crease Pattern: active folds with $G = G_{soft} = 10^2 Pa \cdot m^2$ . Magenta and black lines in Axial Rigidity Distribution: $EA = EA_{min} = 10^4 Pa \cdot m^2$ and $EA = EA_0 = 10^8 Pa \cdot m^2$ . . . . .	52
4.1	Final configurations of the Chomper pattern, Case 1. Dashed lines in Optimized Crease Pattern: active folds with $G = G_{soft} = 10^3 Pa \cdot m^2$ . Magenta and black lines in Projected Axial Rigidity Distribution: $EA = EA_{min} = 10^5 Pa \cdot m^2$ and $EA = EA_0 = 10^7 Pa \cdot m^2$ . . . . .	66
4.2	Final configurations of the Chomper pattern, Case 2. Dashed lines in Optimized Crease Pattern: active folds with $G = G_{soft} = 10^1 Pa \cdot m^2$ . Magenta and black lines in Projected Axial Rigidity Distribution: $EA = EA_{min} = 10^5 Pa \cdot m^2$ and $EA = EA_0 = 10^7 Pa \cdot m^2$ . . . . .	68
4.3	Axial rigidity distribution of Case 1 and Case 2 of the Chomper pattern. . . . .	70
4.4	Final configuration of the Square Twist pattern. Dashed lines in Optimized Crease Pattern: active folds with $G = G_{soft} = 10^1 Pa \cdot m^2$ . White and black lines in Axial Rigidity Distribution: $EA = EA_{min} = 10^6 Pa \cdot m^2$ and $EA = EA_0 = 10^8 Pa \cdot m^2$ . . . . .	72

4.5 Projected final configuration of the Square Twist pattern. Dashed lines in Optimized Crease Pattern: active folds with  $G = G_{soft} = 10^1 Pa \cdot m^2$ . Magenta and black lines in Projected Axial Rigidity Distribution:  $EA = EA_{min} = 10^6 Pa \cdot m^2$  and  $EA = EA_0 = 10^8 Pa \cdot m^2$ . . . . . 74

# List of Figures

1.1	Two paper origami. (a) Origami butterfly; (b) Origami crane. . . .	4
1.2	(a) A conventional origami sheet having creased folds of zeroth-order geometric continuity. (b) A sheet having smooth folds of nonzero surface area and higher-order geometric continuity. . . . .	5
1.3	Identification of folds and facets of a foldable cube and pyramid. . .	5
1.4	Miura-Ori fold pattern. . . . .	7
1.5	Solar sail inspired from the Miura-Ori fold pattern. . . . .	8
1.6	Flasher fold pattern. (a) Folded configuration; (b) Unfolded configuration. . . . .	9
1.7	Simulation of an origami-based deployable solar array for spacecraft applications. . . . .	9
1.8	Starshade deployment motion. . . . .	10
1.9	Hanaflex solar array. . . . .	11
1.10	Self-folding solar array. . . . .	11
1.11	Demonstration of unfolding-based expansion of the Bigelow Expandable Activity Module (BEAM). . . . .	12
1.12	Square Twist fold pattern. . . . .	13
2.1	Sheet with creased folds: (a) Reference configuration $\mathcal{S}_0$ ; (b) Current configuration $\mathcal{S}_t$ . . . . .	16
2.2	Schematics showing unfolded and folded configurations of a creased fold. . . . .	17
2.3	Reference configuration $\mathcal{S}_0$ of an origami sheet: (a) Vertices numeration; (b) Position vectors of the third and fourth vertices; (c) Fold lines numeration; (d) Fold vectors. . . . .	18
2.4	Parameters associated with the interior fold intersection of the origami sheet. (a) Vectors along the fold line that emanates from the intersection; (b) Angles between two fold vectors. . . . .	19
2.5	Generic closed path around the $j$ -th fold intersection. . . . .	22
2.6	Interior fold intersection with: (a) 1 incident fold; (b) 2 incident folds; (c) 3 incident folds. . . . .	24

2.7	Positive and negative crossing of the fold by the path $\check{\gamma}^j(\eta)$ . . . . .	25
2.8	Parameters involved in the folding transformation of an origami sheet. (a) Path $\check{\gamma}^j(\eta)$ ; (b) Vectors $\check{\mathbf{m}}^{jk}$ ; (c) Folding transformation. . . . .	26
2.9	Numerical procedure to determine valid configurations at each increment in the folding motion for origami sheets with creased folds. (a) Illustration of the hypersurface $\mathfrak{R} = \mathbf{0}_{3N_{\mathcal{I}}+2N_{\mathcal{F}}}$ , the initial point $\mathfrak{R}(\hat{\theta}^{l-1})$ and the projected fold angle increment $\Delta\hat{\theta}^{l*}$ ; (b) Subsequent corrections $\Delta\hat{\theta}^{l(k)}$ . . . . .	31
2.10	(a) Configurations of a sheet with eight creased folds, enumerated in counterclockwise order, converging in one interior fold intersection ( $N_{\mathcal{I}} = 1$ ); (b) Folded configuration from the guess increment in Eq. (2.31); (c) Folded configuration from the guess increment in Eq. (2.32); (d) Trend of fold angles and sum of guess increments for the fold angles vs. increment number of the more complex guess increment in Eq. (2.33); (e) Final configurations of the sheet obtained from the guess increments in Eq. (2.33). . . . .	32
2.11	Output plots of the kinematic model for a sheet with eight creased folds: (a) Vertices and fold lines positions; (b) Reference configuration $\mathcal{S}_0$ ; (c) Fold angles vs. number of increments; (d),(e),(f) Configurations at the requested increments. . . . .	33
3.1	Reference grid of an origami sheet in the linear truss method. . . . .	36
3.2	Scheme of the origami element in the linear truss model. . . . .	37
3.3	Flow chart of the linear optimization process. . . . .	41
3.4	Starting configuration of the Chomper pattern. (a) Reference grid; (b) Load and boundary conditions ( $L_x = 1.7 \text{ m}$ , $L_y = 1.0 \text{ m}$ , $F = 100 \text{ N}$ ). . . . .	45
3.5	Objective function over iteration for different $l_0$ in the Chomper pattern. . . . .	46
3.6	Starting configuration of the zigzag structure. (a) Reference grid; (b) Load and boundary conditions ( $L_x = 2.0 \text{ m}$ , $L_y = 1.0 \text{ m}$ , $F = 250 \text{ N}$ ). . . . .	47
3.7	Objective function over iteration for different $m_0$ in the zigzag structure ( $l_0 = 0.5$ ). . . . .	49
3.8	Starting configuration of the Miura-Ori pattern. (a) Reference grid; (b) Load and boundary conditions ( $L_x = 1.0 \text{ m}$ , $L_y = 1.0 \text{ m}$ , $F = 600 \text{ N}$ ). . . . .	50
3.9	Objective function over iteration for different $l_0$ in the Miura-Ori pattern. . . . .	51
3.10	Objective function over iteration for different $m_0$ in the Miura-Ori pattern ( $l_0 = 0.5$ ). . . . .	53

4.1	Scheme of the origami element in the modified nonlinear truss model.	56
4.2	Reference grid of the nonlinear truss model. . . . .	56
4.3	Flow chart of the linear optimization process. . . . .	61
4.4	Starting configuration of the Chomper pattern. (a) Reference grid; (b) Load and boundary conditions ( $L_x = 0.2\ m$ , $L_y = 0.2\ m$ , $F = 10\ 000\ N$ ). . . . .	64
4.5	Case 1, objective function over iteration for different $m_0$ ( $l_0 = 0.44$ ).	67
4.6	Case 2, objective function over iteration for different $m_0$ ( $l_0 = 0.44$ ).	69
4.7	Objective function over iteration with SQP and MMA methods of the Chomper pattern, for $l_0 = 0.44$ , $m_0 = 0.80$ . (a) Case 1; (b) Case 2.	70
4.8	Starting configuration of the Square Twist pattern. (a) Reference grid; (b) Load and boundary conditions ( $L_x = 0.4\ m$ , $L_y = 0.4\ m$ , $F = 10\ 000\ N$ ). . . . .	71
A.1	Crossover operators for an origami with eight fold lines, where $\alpha_k = 0$ represents a soft active fold, while $\alpha_k = 1$ represents a stiff inactive fold. (a) Reference grid and parent chromosome vectors, $\alpha_{p_1}$ and $\alpha_{p_2}$ ; (b) single-point crossover and relative next iteration children, $\alpha_{c_1}$ and $\alpha_{c_2}$ ; (c) Uniform crossover and relative next iteration children, $\alpha_{c_1}$ and $\alpha_{c_2}$ . . . . .	89
A.2	Results for the Square Twist pattern using GA (design variable: $\alpha$ ), where the dashed lines are the soft active folds. (a) Optimized Crease Pattern; (b) Folded Configuration ( $f = -0.775\ mm$ ). . . . .	90
A.3	Mirrored results of Fig. A.2. (a) Optimized Crease Pattern; (b) Flat Folded Configuration ( $f = -0.830\ mm$ ). . . . .	90
B.1	Square Twist Tessellation. (a) Single unit cell; (b) Tessellation pattern of (a). . . . .	91
B.2	Enforcement of Dirichlet boundary conditions using Lagrange multi- plier approach for a unit cell. . . . .	93
D.1	Starting configuration of the unit cell of the Square Twist Tessellation pattern. (a) Reference grid; (b) Crease pattern ( $L_x = 0.8\ m$ , $L_y = 0.8\ m$ ). . . . .	99
D.2	Modal analysis for the Square Twist unit cell tessellation carried out with the optimizer to obtain the deformed configurations of the lowest energy positive mode shapes. . . . .	100
D.3	Loading conditions to carry out the nonlinear simulation with peri- odic boundary conditions and MGDCM. . . . .	101
D.4	4x4 Final folded Square Twist Tessellation pattern obtained with periodic boundary conditions. . . . .	101

E.1	Parameters for the Optimization framework. . . . .	103
E.2	Interpolation of the solution between arc-length steps. . . . .	104
E.3	Flowchart of the optimization process for a gradient-based optimization and the Genetic Algorithm. . . . .	105
E.4	Starting configuration. (a) Reference grid; (b) Load and boundary conditions ( $F = 10^6 N$ , $EA/G_{soft} = 10^6$ and $EA/G_{stiff} = 10^1$ ). . . . .	106
E.5	Initial fold pattern for the modal analysis. . . . .	107
E.6	Modal analysis for the fold pattern in Fig. E.5. . . . .	107
E.7	Nonlinear actuation of mode 30. . . . .	107
E.8	Miura-Ori auxetic design discovered with the described optimization method based on the Genetic Algorithm. . . . .	108



# Chapter 1

## Introduction to Origami Structures

### 1.1 Introduction

Origami is the ancient Japanese art of paper folding that has deep roots and its own philosophy. In the seventies of the last century, some researchers discovered that in theory, through conventional origami, an infinite number of shapes could be obtained [1]. This enabled new applications, allowing the discovery of new promising designs for many engineering structures. Therefore, through origami, the engineer gets the opportunity to transform a true work of art into a structure that is tailored for a specific application.

The reason why origami are so versatile, especially in the aerospace field, is that they make a two-dimensional component (like a plate) into a three-dimensional one through folding and unfolding. Moreover, space structures must be lightweight and compact during launch, while being deployable in space to maximize the surface area. Therefore, the most relevant applications of space origami are deployable space arrays and antennas [2, 3, 4, 5]. To this end, it is necessary to develop models and analysis methods to allow for the understanding and computational implementation of their kinematics and mechanics. Such a task is quite complex because of the intricate designs and folding motions of these structures.

At the foundation of every origami design approach, there are many theoretical notions to consider such as the definition of folds and the fold constraints [6, 1]. Numerous studies have considered rigidly foldable fold patterns [7] and various kinematic approaches have been applied [7, 8, 1], using the assumptions that the facets are rigid and do not bend nor stretch and that the folds are creases (i.e.



straight lines with zeroth-order geometric continuity). To improve on this analysis, Schenk et al. [9] introduced a truss model to allow for facet deformations using a linear method, hence considering only small strains and small deformations. The truss model simplifies the configuration of the origami: each vertex in the folded sheet is represented by a pin-joint and every border and fold line by a truss element. This method was applied to topology optimization by Fuchi et al. [10, 11], with the objective of discovering origami crease patterns that maximize displacements at set locations.

In order to take into account the large deformations and large rotations typical of origami, nonlinear models are required. Filipov et al. [12] and Liu et al. [13] introduced a truss and hinge model to consider material and geometric nonlinearities. Also, Filipov et al. [14] verified the accuracy of these truss models by comparing them to shell and 3D continuum elements. A nonlinear truss model was introduced by Gillman et al. [15], based on the positional finite element truss proposed by Greco et al. [16], considering a torsional spring around each truss element of the origami. There, periodic boundary conditions were described to analyze origami tessellation patterns.

Origami structures exhibit one or more critical points during their folding motions, therefore the arc-length method, first introduced by Risks [17, 18] and Wempner [19], and later analyzed by Leon et al. [20], was included in the formulation by Gillman et al. [15]. Also, the Modified Generalized Displacement Control Method (MGDCM) as introduced by Leon et al. [21] was employed to find efficient solutions for the system of nonlinear equations while adjusting the step size based on the loading profile curvature.

Lastly, modal analysis is required to distinguish and follow the multiple bifurcation branches off the flat state typical of origami structures with complex designs. To consider this bifurcation problem, Tachi and Hull [22] focused on fully rigid facets, while Santangelo [23] neglected fold stiffness, considering only fold stretching. Therefore, Gillman et al. [15] introduced a formulation to consider both fold stiffness and fold stretching in modal analysis.

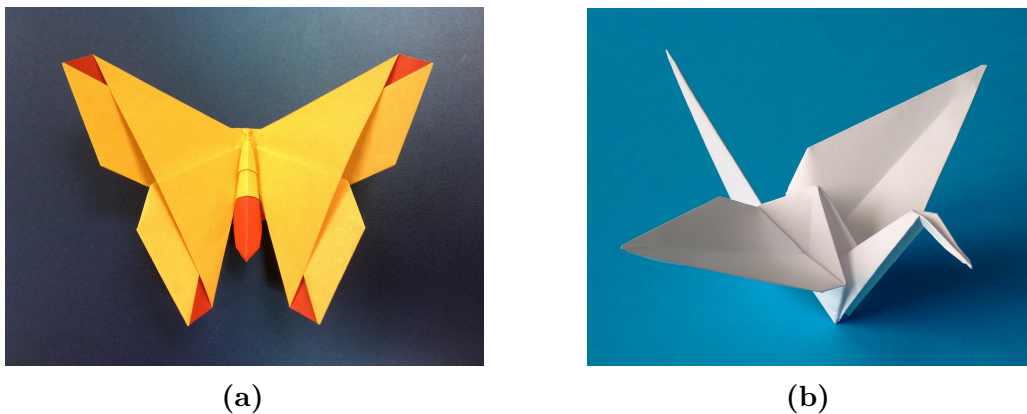
The modified nonlinear truss model by Gillman et al. [15] was later applied to topology optimization [24, 25], however employing a simple Newton-Raphson method to solve the system of nonlinear equations introduced by the problem. There, a procedure to find an origami crease pattern that achieves desired large deformation through folding for a given input force was provided, using the fold stiffness as a design variable and applying a constraint on the number of fold lines.

Lastly, Gillman et al. [26] applied the topology optimization method with the truss model to discover origami structures with auxetic behavior, like the Miura-Ori fold pattern [27].

## 1.2 Basics of Origami

The term *origami* comes from the Japanese word *ori* or *oru* which means "fold" and *gami* or *kami* which means "paper". The *art of paper folding* traces its roots to China shortly after the invention of paper in the second century. However, it was later introduced in Japan during ceremonies for decoration purposes, also acquiring philosophical meaning [28].

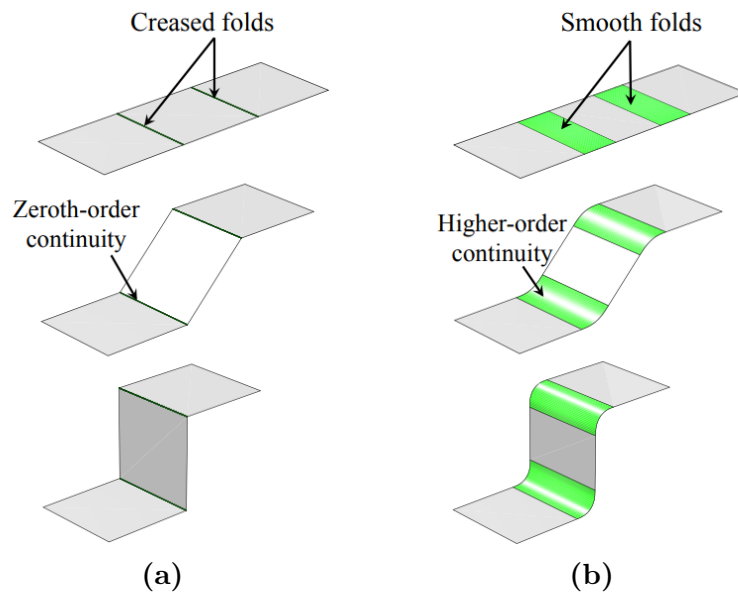
Two examples of origami are presented in Fig. 1.1: Fig. 1.1a shows an origami butterfly, symbol of a soul set free, while Fig. 1.1b shows an origami crane, symbol of peace, love, hope, and healing.



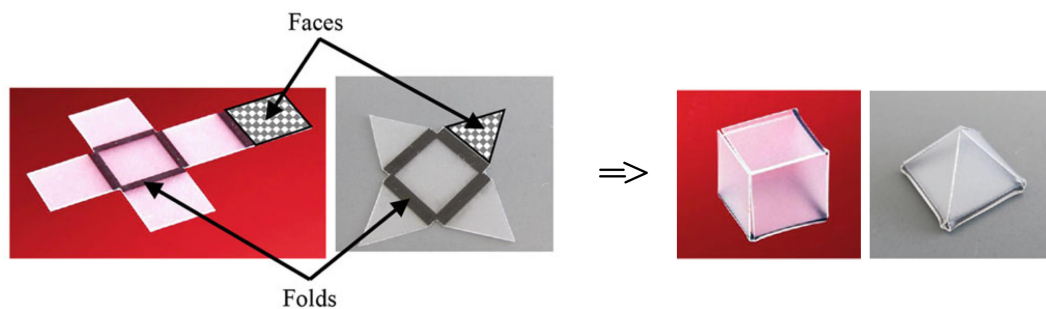
**Figure 1.1:** Two paper origami. (a) Origami butterfly [29]; (b) Origami crane [30].

For origami, the final shape is obtained from folding an initially planar sheet along the *folds*, i.e. deformations in which the in-surface distance between any two points in the plane is constant and the sheet does not self-intersect. In the case of *creased folds*, the folds are straight line segments (zeroth-order continuity), while in the case of *smooth folds*, they are localized regions with a certain area (higher-order continuity), as shown in Fig. 1.2. The layout of the folds in the planar configuration of the sheet is termed the *fold pattern*.

Other identifiable regions are the *facets*, surfaces bounded by the folds and by the boundary of the sheet. Folds and facets are indicated in two examples in Fig. 1.3, representing a foldable cube and a pyramid.



**Figure 1.2:** (a) A conventional origami sheet having creased folds of zeroth-order geometric continuity. (b) A sheet having smooth folds of nonzero surface area and higher-order geometric continuity [31].



**Figure 1.3:** Identification of folds and facets of a foldable cube and pyramid [1].

This work will be focused on the idealization of creased folds, which permits the development of simpler models and designs for origami structures. Therefore, folds will be referred to as creases arbitrarily. However, this simplification is not appropriate for structures with non-negligible fold thickness or produced from materials that do not provide sufficient strains to sustain the high curvature required for the creased folds [32].

Frequently, the folding motion of origami structures is imposed by external mechanical loads. Nevertheless, for certain cases like remote applications in space, this method is impractical. For this reason, structures with self-folding capabilities have been studied, i.e. structures with the ability to fold and unfold without applying external loads. A solution is given by active materials, which convert various forms of energy into mechanical work, to generate the desired folding behavior. These structures are called *active origami structures*, extensively discussed by Peraza et al. [1].

### 1.3 Advantages and Disadvantages of Origami Structures

Origami structures have been widely used in the space industry. Meloni et al. [33] summarized the key aspects that permitted their success, which are the following:

- *Stowability*: Capability to be stowed, i.e. compacted and stored inside the limited dimensions of launch vehicles minimizing the occupied volume;
- *Deployability*: Capability to be deployed from a  $2D$  reference configuration to a  $3D$  final configuration. This allows the structures to be deployed in their final shape in space.
- *Scalability*: Capability to be changed in scale through folding and unfolding. This improves the range of applications of origami-based designs, making them basically scale-independent.
- *Self-actuation*: Capability to fold and unfold without an external actuation, like in the case of active origami structures.
- *Reconfigurability*: Capability to dynamically change the shape according to specific design constraints, without altering the geometrical configuration of the structure.
- *Tunability*: Capability to be tailored for a specific task changing their geometrical properties, achieving specific behaviors not present in conventional materials.
- *Easiness in manufacturing*: Capability to be manufactured in  $2D$  and then assembled in the final  $3D$  configuration, simplifying the production process, the storage and the material usage in comparison to traditional designs.

Also, like in the case of origami mechanisms, they allow to reach a targeted actuation without the need for multiple mechanical parts. Other advantages are reduced

friction, elimination of lubricants, increased precision, and ease of miniaturization.

Although origami structures are particularly suitable for the design of space structures, their application in space missions is still limited. This is due to the *complexity* of the nonlinear dynamics of deployment, of the mechanical systems and the impossibility of being tested in orbit. For this reason, it is often mandatory to use simplified design processes, but that still provide reliable results [1].

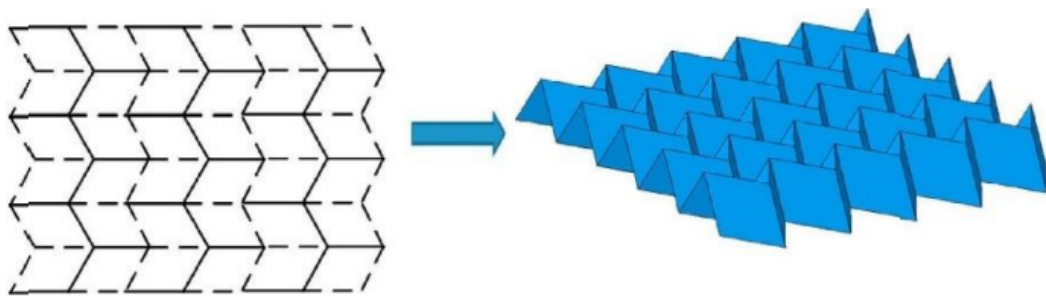
## 1.4 Space Applications of Origami Structures

Space structures like solar arrays, solar sails, sun shades, antennas, etc must be lightweight, compact and small during transportation to space, and of large size when deployed in orbit (for example to maximize their energy absorption in the case of solar arrays). Therefore, efficient packing methods in launch vehicles are always under study.

Using multiple complex mechanisms that act along different directions for the deployment of space structures would be inefficient in space. This makes origami the best choice since they allow the folding and unfolding of the space structure in one continuous movement. Therefore, they provide the possibility of carrying more equipment in space. Various examples of origami applications for space are shown as follows.

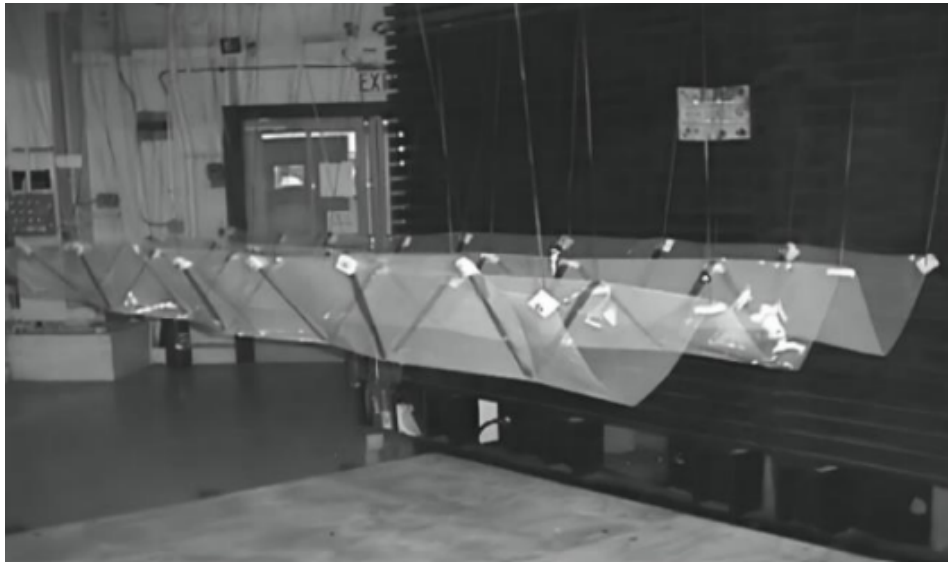
### Miura-Ori fold pattern

One of the first origami designs used in space was the *Miura-Ori* fold pattern [27] illustrated in Fig. 1.4, proposed by Koryo et al. [34], designed during research on deployable structures in space.



**Figure 1.4:** Miura-Ori fold pattern [35].

This fold pattern was first successfully applied to the design of a solar sail (as shown in Fig. 1.5) [36].



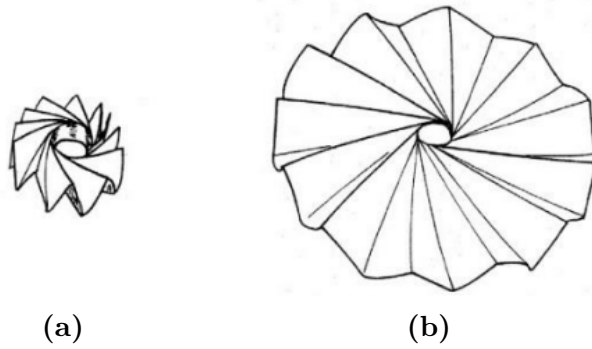
**Figure 1.5:** Solar sail inspired from the Miura-Ori fold pattern [37].

One example of its applications was the *Space Flyer Unit (SFU)* [38, 39, 40, 41], a satellite launched in 1995 for space experiments and observation purposes. The Miura-Ori fold was used as a method of deploying and stowing the solar array of the satellite. It allowed the solar panels to be stowed compactly in a restricted space as well as to be easily deployed. Various experiments on the stowage and deployment of solar panels using the Miura-Ori fold have been successfully carried out in space. A peculiar characteristic of this fold pattern is its *auxetic* behavior, i.e. the global Poisson coefficient of this structure is negative, therefore it expands in the orthogonal directions under uniaxial tension and collapses under compression [42, 43].

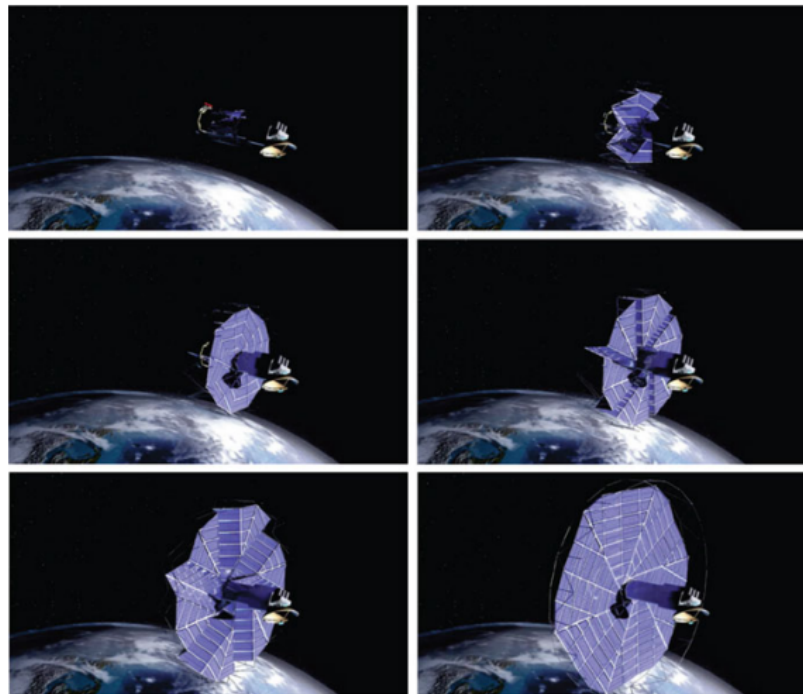
## Flasher fold pattern

Another efficient origami design used in space is the *Flasher* fold pattern in Fig. 1.6. A simulation of a solar array deployed with this configuration is shown in Fig. 1.7.

This design for the solar array would be able to fit in a relatively small volume during launch while achieving a larger deployed area than other configurations that do not use origami, providing more energy to the satellite to which the solar array is attached.



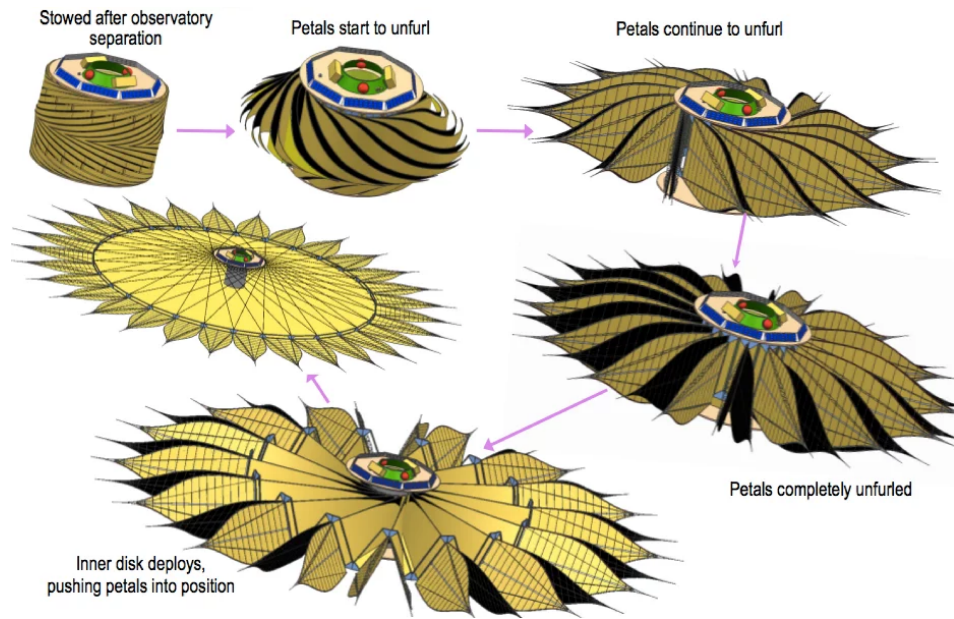
**Figure 1.6:** Flasher fold pattern. (a) Folded configuration; (b) Unfolded configuration [44].



**Figure 1.7:** Simulation of an origami-based deployable solar array for spacecraft applications [45].

## Star Shade

Fig. 1.8 illustrates the folding/unfolding motion of *Starshade* [46], an innovative origami-based design from an ongoing NASA project.



**Figure 1.8:** Starshade deployment motion [47].

It works in parallel with a space telescope and has the aim to shade it from the light of the stars, enabling the imagining of exoplanets orbiting around those stars [46]. The structure is able to fit within the 5m diameter constraint of launch vehicles but has a deployed diameter of 34m. The inner disk is an optimized version of the Flasher origami pattern covered with layers of carbon-impregnated black Kapton (a high-performance plastic, used for example in space blankets). The petals are made of a thin carbon fiber structure covered with Kapton as well and their shape, when seen from far away, creates a softer edge that causes less bending of light waves and therefore a darker shadow. For its design, an inverse design workflow algorithm was applied to determine the best crease pattern geometry [33].

## Hanaflex solar array

Fig. 1.9 shows yet another use of the Flasher pattern, implemented by Zirbel and co-workers, who proposed *Hanaflex* [48], an origami-based deployable system for solar arrays that can reach a deployed dimension 10 times greater than the stowed one. An advantage of this architecture is that additional rings can be added to the base without altering the height of the stowed geometry, yet increasing its diameter. However, despite the high deployment ratio, Hanaflex is composed of a higher number of segments that may lead to limitations.



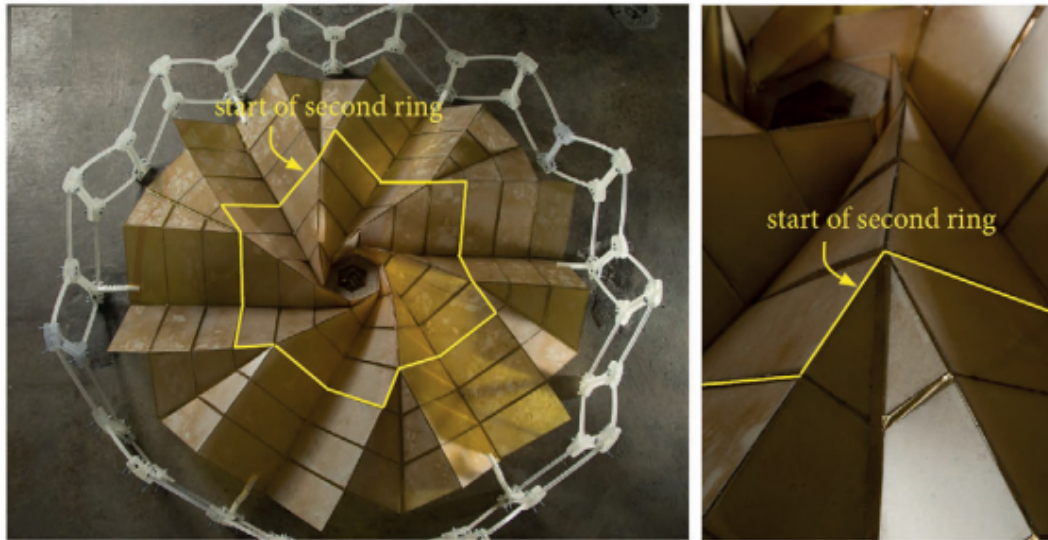


Figure 1.9: Hanaflex solar array [48].

## Active Origami Structures

Fig. 1.10 shows an example of an active origami structure that avoids the complexity of the actuation systems [49].

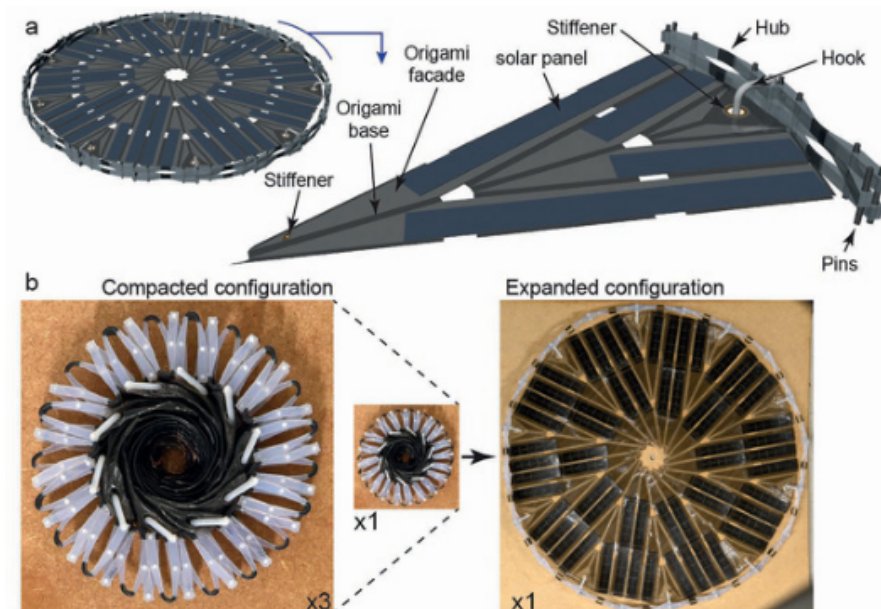
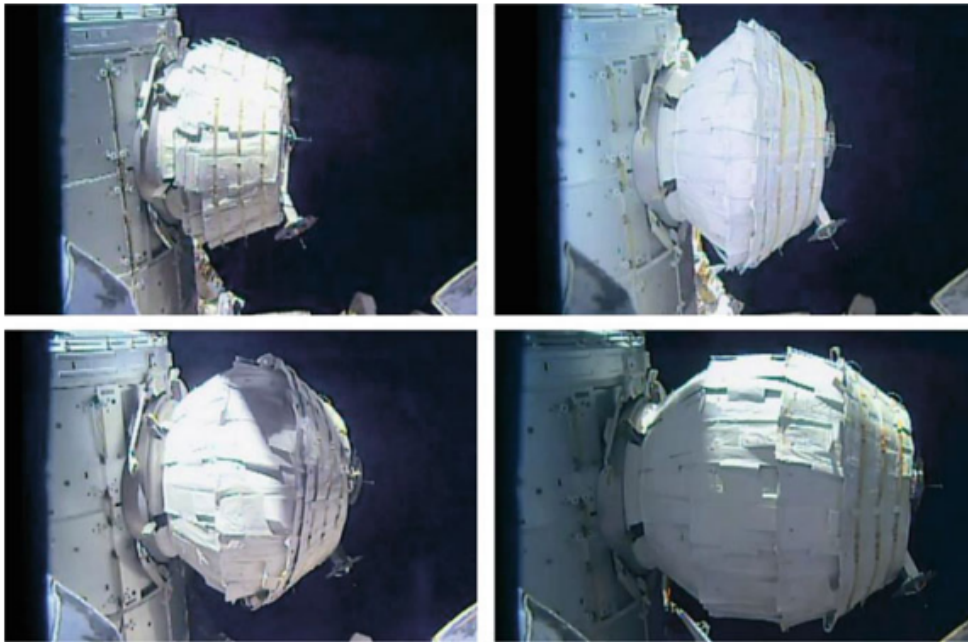


Figure 1.10: Self-folding solar array [33].

This origami-based self-deployable solar array is 3D printed with shape memory polymers and is programmed to activate in response to changes in the surrounding temperature. The deployment actuation consists in an initial actuation performed by the outer ring followed by a second actuation due to the active materials. The final prototype showed an expansion ratio of 1000% without external actuators. Nevertheless, it must be noted that its deployment mechanism is not reversible.

## Bigelow Expandable Activity Module (BEAM)

Another example is given in Fig. 1.11, which illustrates an origami-inspired *Bigelow Expandable Activity Module* (BEAM), an expandable habitat technology demonstration for the International Space Station (ISS).

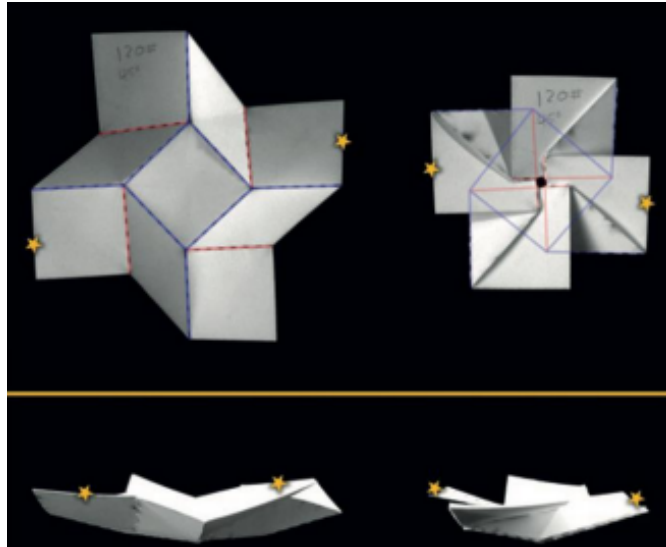


**Figure 1.11:** Demonstration of unfolding-based expansion of the Bigelow Expandable Activity Module (BEAM) [NASA TV] [45].

Since future space missions might require a significantly smaller transport volume, a solution could be given by these expandable habitats. They only take up a small amount of room in a spacecraft, but once they are released into space they expand to provide a spacious environment for humans [50].

## Square Twist fold pattern

Lastly, the *Square Twist* fold pattern is illustrated in Fig. 1.12.



**Figure 1.12:** Square Twist fold pattern [51].

This configuration has extensive applications in aerospace engineering thanks to its symmetrical rotation and it is applied to the design of antennas in space [52].

## 1.5 Objectives

The main objective of this work is to improve the topology optimization method proposed by Fuchi et al. [11] regarding linear analysis and by Gillman et al. [25] regarding nonlinear analysis, introducing axial rigidity as a design variable thus allowing each truss to stretch in an optimized way. Although the complexity of the problem is slightly increased with respect to these works, this modification enables to obtain new promising origami designs.

Gillman et al. [24, 25] applied both gradient and non-gradient-based methods to topology optimization, making comparisons between the different obtained results. Here, in order to emphasize convergence speed, two gradient-based methods are used to perform the optimization: the Method of Moving Asymptotes (MMA) [53] and the Sequential Quadratic Programming (SQP) [54]. Also, the axial rigidity distribution is optimized through the modified Solid Isotropic Material with Penalization (SIMP) method, introduced by Bendsoe and Kikuchi [55] and Rozvany and Zhou [56], later modified by Andreassen et al. [57].

Throughout this thesis, the reader can begin to understand both the potential and the complexity of origami-inspired structures, in the hope that this work will inspire the development of more design methods that will ease the introduction of origami in various engineering fields, especially in space applications.

## **1.6 Chapters Overview**

In this first Chapter, origami structures were introduced providing some necessary definitions. Advantages and disadvantages were discussed, along with some applications of these structures in space.

Next, Chapter 2 will provide a description of the kinematics of origami with the idealization of rigid origami and creased folds, allowing for the understanding of their complex motion.

Subsequently, in Chapters 3 and 4, the modified topology optimization methods with linear and nonlinear analysis will be described, with the objective of finding the axial rigidity distribution of the trusses and the crease pattern that maximizes displacement at set locations.

Then, in Chapter 5, the discussed topics will be restated.

Lastly, in the Appendix, some further developments of the described optimization method will be discussed with the intention of expanding its field of applications.

## Chapter 2

# Kinematics of Origami Structures With Creased Folds

In this Chapter, the kinematics of origami is described. This kind of analysis is the first step in the study of these complex structures since it allows for the understanding of their folding behavior.

### 2.1 Origami Structures With Creased Folds

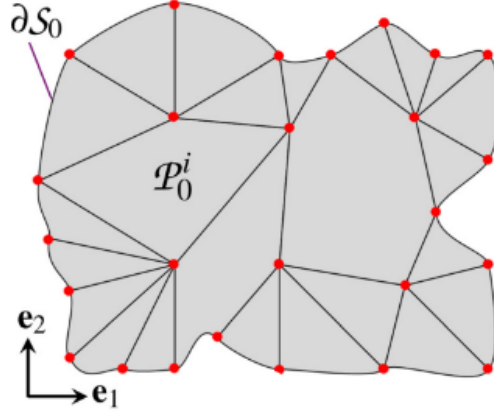
Origami Structures are significantly complex in their geometry and motion. Therefore, in order to develop a simpler mathematical model, it is convenient to apply the following assumptions:

1. Folds are straight creases (creased folds);
2. The facets are rigid, i.e. they do not bend nor stretch;
3. The sheet is not torn;
4. The sheet does not self-intersect.

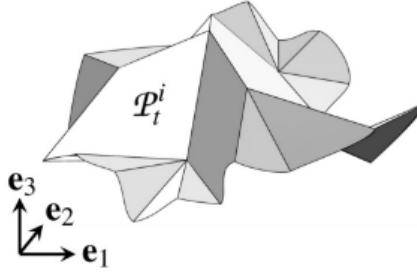
A configuration that satisfies the properties 2, 3 and 4 is said to be a *valid configuration*.

Following the description presented by Peraza et al. [1, 8], this chapter is going to describe the kinematic modeling of origami structures based on such assumptions, which is the study of their motion without considering their constituent materials or the physical stimuli causing such a motion.

Considering  $t \in [0, t_f]$  as the *time parameter*, the folding motion starts with a planar reference configuration  $\mathcal{S}_0$  at  $t = 0$  and reaches the final configuration  $\mathcal{S}_{t_f}$  at  $t = t_f$  passing through an intermediate configuration  $\mathcal{S}_{t_i}$  (Fig. 2.1).



(a)

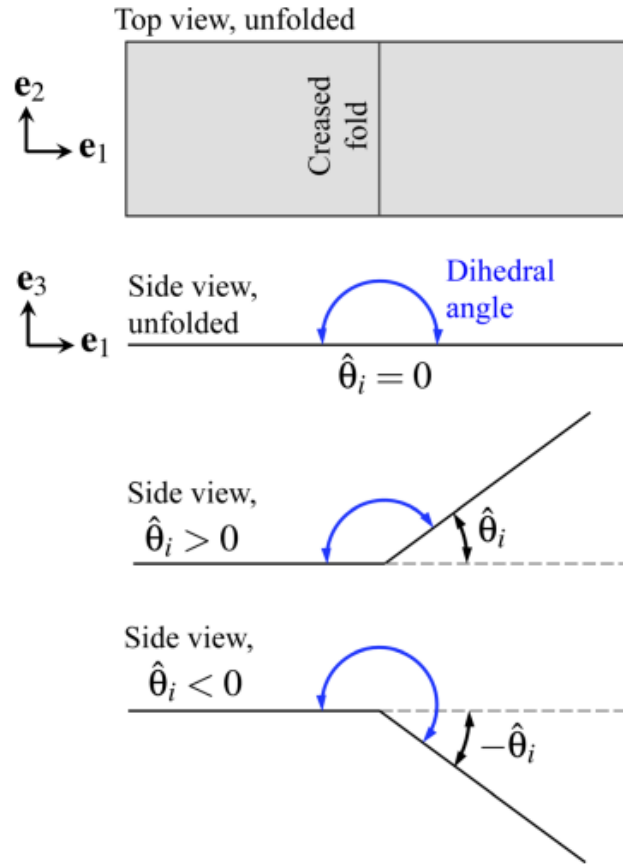


(b)

**Figure 2.1:** Sheet with creased folds: (a) Reference configuration  $\mathcal{S}_0$ ; (b) Current configuration  $\mathcal{S}_t$  [8].

In order to identify the position of the points in a given configuration of the sheet, it is useful to introduce the orthonormal vectors  $\mathbf{e}_i \in \mathbb{R}^3$ ,  $i = 1, 2, 3$ , that define the fixed global coordinate system.  $\mathcal{S}_0$  is assumed planar, so it is fully contained in the plane spanned by  $\mathbf{e}_1$  and  $\mathbf{e}_2$  and has no overlaps. The configuration of the facets comprising  $\mathcal{S}_t$  is denoted  $\mathcal{P}_t^i \subset \mathcal{S}_t$ ,  $i = 1, \dots, N_{\mathcal{P}}$  where  $N_{\mathcal{P}}$  is the number of facets in the sheet (i.e.  $\mathcal{S}_t = \bigcup_{i=1}^{N_{\mathcal{P}}} \mathcal{P}_t^i$ ).

To fully describe the configuration of an origami sheet, the only kinematic variable needed is the *fold angle*  $\hat{\theta}_i(t)$ , angle between two joined facets defined as  $\pi$  radians less the dihedral angle between the positive sides of the two facets joined by the  $i$ -th creased fold (Fig. 2.2).

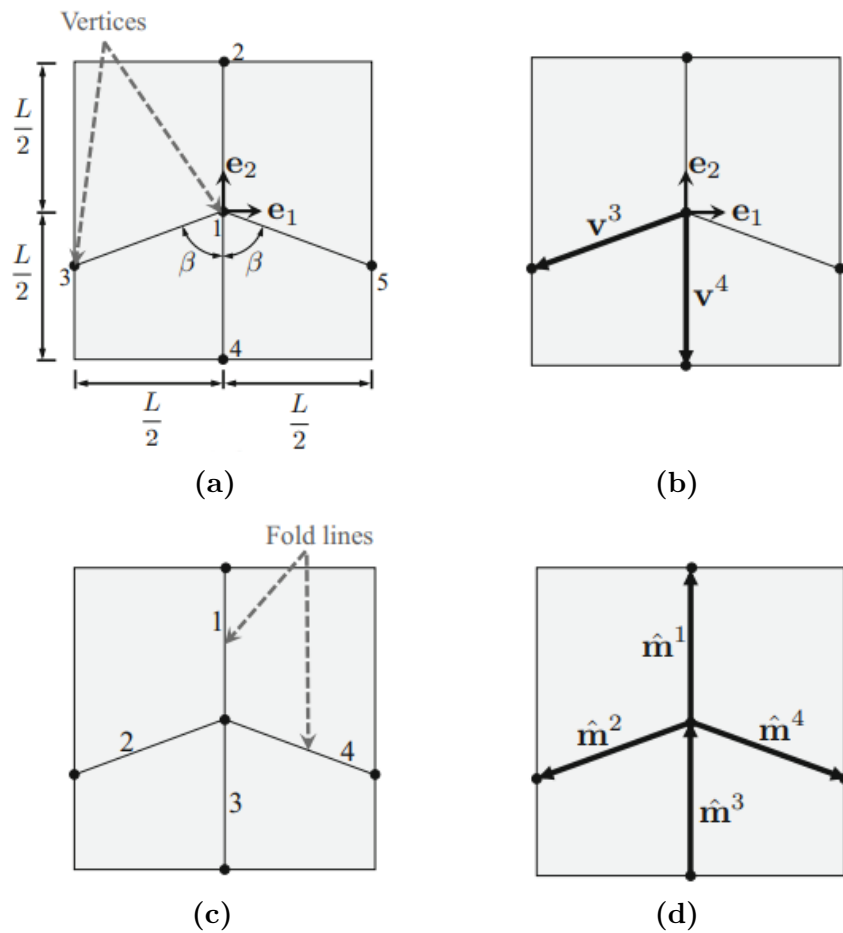


**Figure 2.2:** Schematics showing unfolded and folded configurations of a creased fold [8].

Each fold angle  $\hat{\theta}_1(t), \dots, \hat{\theta}_{N_{\mathcal{F}}}(t)$ , where  $N_{\mathcal{F}}$  is the number of creased folds in the sheet, is a continuous function with respect to the time parameter  $t$  since the motion of the sheet must be continuous. Lastly, to prevent self-intersection of any pair of facets connected by a creased fold, the value of the associated fold angle must be contained in the interval  $[-\pi, \pi]$ .

## 2.2 Fold Pattern Description

The layout of the fold lines in the reference configuration  $\mathcal{S}_0$  is known as the *fold pattern* that, along with the history of folding motion, determines the final configuration of the sheet. Fig. 2.3 shows the reference configuration  $\mathcal{S}_0$  of a sheet with a simple fold pattern. In Fig. 2.3a the *fold lines* are coincident with the creased folds. They are typically defined by their endpoints i.e. the *vertices*, each of which has an associated position vector denoted  $\mathbf{v}^j \in \text{span}(\mathbf{e}_1, \mathbf{e}_2)$ ,  $j = 1, \dots, N_{\mathcal{I}}, N_{\mathcal{I}} + 1, \dots, N_{\mathcal{I}} + N_{\mathcal{B}}$ , where  $N_{\mathcal{I}}$  is the number of the vertices located at the interior of  $\mathcal{S}_0$  while  $N_{\mathcal{B}}$  at its boundary.



**Figure 2.3:** Reference configuration  $\mathcal{S}_0$  of an origami sheet: (a) Vertices numeration; (b) Position vectors of the third and fourth vertices; (c) Fold lines numeration; (d) Fold vectors [1].



In order to be consistent with the numeration in the fold pattern, it is necessary to define the *fold connectivity matrix*  $\mathbf{C}^{\mathcal{F}} \in \mathbb{R}^{N_{\mathcal{F}} \times 2}$  with components  $C_{ij}^{\mathcal{F}}$ ,  $i = 1, \dots, N_{\mathcal{F}}$ , defined as:

- $C_{i1}^{\mathcal{F}}$  = Index of the vertex corresponding to the start point of the  $i$ -th fold line;
- $C_{i2}^{\mathcal{F}}$  = Index of the vertex corresponding to the endpoint of the  $i$ -th fold line;

Moreover, the following parameters must be introduced:

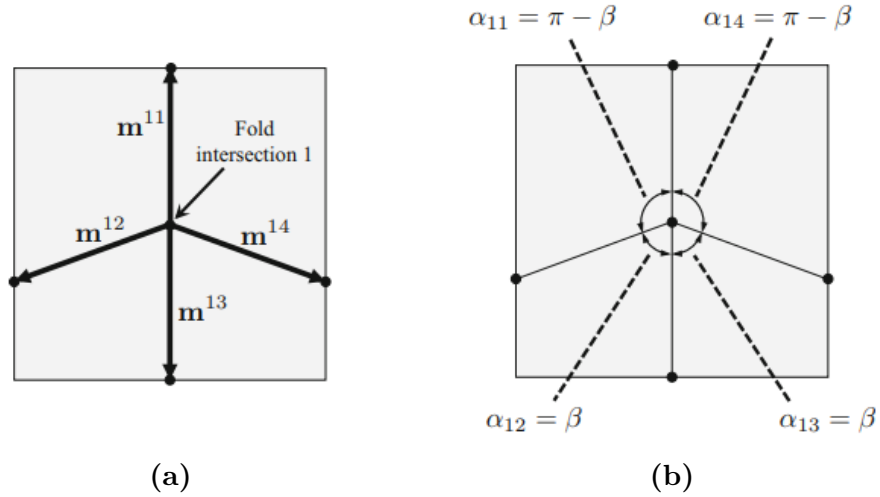
- $\hat{\mathbf{v}}^{i1}, \hat{\mathbf{v}}^{i2} \in \text{span}(\mathbf{e}_1, \mathbf{e}_2)$  are the position vectors of the vertices from which each fold line in the sheet emanates and ends, respectively. They are defined as:

$$\hat{\mathbf{v}}^{i1} = \mathbf{v}^{C_{i1}^{\mathcal{F}}}, \quad \hat{\mathbf{v}}^{i2} = \mathbf{v}^{C_{i2}^{\mathcal{F}}}; \quad (2.1)$$

- $\hat{\mathbf{m}}^1, \dots, \hat{\mathbf{m}}^{N_{\mathcal{F}}} \in \text{span}(\mathbf{e}_1, \mathbf{e}_2)$  are the *fold vectors* along the fold lines: They are defined as:

$$\hat{\mathbf{m}}^i = \hat{\mathbf{v}}^{i2} - \hat{\mathbf{v}}^{i1}; \quad (2.2)$$

- $n_1, \dots, n_{N_{\mathcal{I}}}$  are the number of fold lines incident to each interior fold intersection of  $\mathcal{S}_0$ ;
- $\mathbf{m}^{jk} \in \text{span}(\mathbf{e}_1, \mathbf{e}_2)$ ,  $j = 1, \dots, N_{\mathcal{I}}$ ,  $k = 1, \dots, n_j$  are the vectors along the length of the  $k$ -th fold line incident to the  $j$ -th interior fold intersection that emanates from such an intersection (Fig. 2.4a).



**Figure 2.4:** Parameters associated with the interior fold intersection of the origami sheet. (a) Vectors along the fold line that emanates from the intersection; (b) Angles between two fold vectors [1].

The vectors  $\mathbf{m}^{j1}, \dots, \mathbf{m}^{jn_j}$  in the  $j$ -th interior fold intersection are arranged in counterclockwise order. To identify and order the folds incident to the interior fold intersection, the *fold intersection connectivity matrix*  $\mathbf{C}^{\mathcal{I}} \in \mathbb{R}^{N_{\mathcal{I}} \times \max(n_j)}$  is introduced, with components  $C_{jk}^{\mathcal{I}}$  defined as:

$C_{jk}^{\mathcal{I}}$  = Index of the  $k$ -th fold line incident to the  $j$ -th interior fold intersection  
(multiplied by  $-1$  if the fold line ends at the interior fold intersection).

This way it is possible to correlate the fold vectors  $\hat{\mathbf{m}}^1, \dots, \hat{\mathbf{m}}^{N_{\mathcal{F}}}$  in Eq. (2.2) to the vectors  $\mathbf{m}^{j1}, \dots, \mathbf{m}^{jn_j}$  with the following system:

$$\mathbf{m}^{jk} = \begin{cases} \hat{\mathbf{m}}^{C_{jk}^{\mathcal{I}}} & C_{jk}^{\mathcal{I}} > 0 \\ -\hat{\mathbf{m}}^{|C_{jk}^{\mathcal{I}}|} & C_{jk}^{\mathcal{I}} < 0 \end{cases}, \quad (2.3)$$

where the minus sign in the case where  $C_{jk}^{\mathcal{I}} < 0$  is needed to always emanate the vector from the interior fold intersection.

Let  $\varphi(\mathbf{y}, \mathbf{z})$  be the angle between the vectors  $\mathbf{z} \in \text{span}(\mathbf{e}_1, \mathbf{e}_2)$  and  $\mathbf{y} \in \text{span}(\mathbf{e}_1, \mathbf{e}_2)$ , defined as:

$$\varphi(\mathbf{y}, \mathbf{z}) = \begin{cases} \cos^{-1} \frac{\mathbf{y} \cdot \mathbf{z}}{\|\mathbf{y}\| \|\mathbf{z}\|} & (\mathbf{e}_3 \times \mathbf{z}) \cdot \mathbf{y} \geq 0 \\ 2\pi - \cos^{-1} \frac{\mathbf{y} \cdot \mathbf{z}}{\|\mathbf{y}\| \|\mathbf{z}\|} & (\mathbf{e}_3 \times \mathbf{z}) \cdot \mathbf{y} < 0 \end{cases}. \quad (2.4)$$

The angles between two fold vectors associated with the interior fold intersection are  $\alpha_{j1}, \dots, \alpha_{jn_j}$  (Fig. 2.4b), defined as:

$$\alpha_{jk} = \begin{cases} \varphi(\mathbf{m}^{jk+1}, \mathbf{m}^{jk}) & k = 1, \dots, n_j - 1 \\ \varphi(\mathbf{m}^{j1}, \mathbf{m}^{jk}) & k = n_j \end{cases}. \quad (2.5)$$

## 2.3 Kinematic Constraints

As shown by Peraza et al. [1, 8], the fundamental kinematic constraints for origami with creased folds are the *developability constraint* and the *loop closure constraint*.

### 2.3.1 Developability Constraint

A *developable surface* has zero Gaussian curvature everywhere. Developability allows a surface to be flattened onto a plane without stretching or overlapping. Since in a valid configuration the facets must remain planar and joined at straight creased folds, the Gaussian curvature is non-trivially zero only in the singular points corresponding to the interior fold intersections. In these points, a *discrete Gaussian curvature*  $\mathbf{K}_j$  must be considered. It is defined as:

$$\boxed{\mathbf{K}_j = 2\pi - \sum_{k=1}^{n_j} \alpha_{jk} = 0}, \quad (2.6)$$

where  $\alpha_{jk}$  are the facet corner angles surrounding each interior fold intersection in Eq. (2.5). If this equation is satisfied for any fold intersection in the sheet, the structure is developable.

### 2.3.2 Loop Closure Constraint

Each constraint is formulated in order to satisfy the assumption of valid configuration described in Section 2.1. The constraints on the configuration space depend on the constraints for the fold angles  $\hat{\theta}_i$ , which can be formulated as a set of constraints for the fold angles associated with the folds incident to each interior vertex  $\theta_{jk}$ , with the following equation:

$$\theta_{jk} = \hat{\theta}_{|C_{jk}^{\mathcal{I}}|}. \quad (2.7)$$

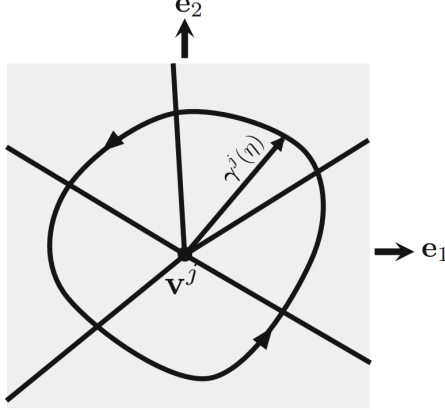
Let  $\gamma^j(\eta) : [0,1] \rightarrow \mathcal{S}_0$  be a generic counterclockwise closed path around the  $j$ -th fold intersection as in Fig. 2.5. Moreover, a point in the reference configuration  $\mathcal{S}_0$  is defined by the position vector  $\mathbf{X} \in \text{span}(\mathbf{e}_1, \mathbf{e}_2)$ , while a point in the current configuration  $\mathcal{S}_t$  is defined by  $\mathbf{x} \in \mathbb{R}^{3 \times 3}$ . To determine the mapping between reference and current configurations of the facets crossed by  $\gamma^j(\eta)$ , i.e.  $\mathbf{X} \mapsto \mathbf{x}$ , two rotation matrices are required:

- $\mathbf{R}_1(\phi) \in \mathbb{R}^{3 \times 3}$ : transformation matrix associated with a rotation by  $\phi$  about an axis of rotation aligned to  $\mathbf{e}_1$

$$\mathbf{R}_1(\phi) := \begin{bmatrix} 1 & 0 & 0 \\ 0 & \cos(\phi) & -\sin(\phi) \\ 0 & \sin(\phi) & \cos(\phi) \end{bmatrix}; \quad (2.8)$$

- $\mathbf{R}_3(\phi) \in \mathbb{R}^{3 \times 3}$ : transformation matrix associated with a rotation by  $\phi$  about an axis of rotation aligned to  $\mathbf{e}_3$

$$\mathbf{R}_3(\phi) := \begin{bmatrix} \cos(\phi) & -\sin(\phi) & 0 \\ \sin(\phi) & \cos(\phi) & 0 \\ 0 & 0 & 1 \end{bmatrix}. \quad (2.9)$$



**Figure 2.5:** Generic closed path around the  $j$ -th fold intersection [1].

The transformation related to a rotation by  $\phi$  about an axis aligned with a vector  $\mathbf{y} \in \text{span}(\mathbf{e}_1, \mathbf{e}_2)$  can be represented as

$$\mathbf{R}_3(\varphi(\mathbf{y}))\mathbf{R}_1(\phi)\mathbf{R}_3^{-1}(\varphi(\mathbf{y})), \quad (2.10)$$

where the axis of rotation is first aligned to  $\mathbf{e}_1$  through  $\mathbf{R}_3^{-1}(\varphi(\mathbf{y}))$ , then rotated by  $\phi$  about  $\mathbf{e}_1$  through  $\mathbf{R}_1(\phi)$ , lastly re-aligned to its original orientation through  $\mathbf{R}_3(\varphi(\mathbf{y}))$ . From Eq. (2.10) it is possible to describe the transformation associated with the folding of the  $k$ -th creased fold crossed by  $\gamma^j(\eta)$ . This transformation can be considered as a rotation of  $\theta_{jk}$  about an axis of rotation aligned to  $\mathbf{m}^{jk}$  in the following way:

$$\mathbf{R}_3(\varphi(\mathbf{m}^{jk}))\mathbf{R}_1(\theta_{jk})\mathbf{R}_3^{-1}(\varphi(\mathbf{m}^{jk})). \quad (2.11)$$

Therefore, the mapping  $\mathbf{X} \mapsto \mathbf{x}$  is the composition of these transformations associated with the folds crossed by the segment of path  $\gamma^j(\eta)$ :

$$\mathbf{x} = \left( \prod_{k=1}^{n_\gamma} \mathbf{R}_3(\varphi(\mathbf{m}^{jk}))\mathbf{R}_1(\theta_{jk})\mathbf{R}_3^{-1}(\varphi(\mathbf{m}^{jk})) \right) \mathbf{X}. \quad (2.12)$$

where  $n_\gamma$  is the number of folds crossed by  $\gamma^j(\eta)$ .

The fold angles  $\theta_{jk}$  must be constrained to prevent the tearing of the facets joined to each interior vertex. For this reason, it can be noted that the mapping between reference and current configurations in Eq. (2.12) must result in  $\mathbf{x} = \mathbf{X}$  for any point in the fixed facet. Therefore, during a rigid deformation, the following constraint must be satisfied:

$$\prod_{k=1}^{n_j} \mathbf{R}_3(\varphi(\mathbf{m}^{jk})) \mathbf{R}_1(\theta_{jk}) \mathbf{R}_3^{-1}(\varphi(\mathbf{m}^{jk})) = \mathbf{I}_3, \quad (2.13)$$

which can be simplified in:

$$\boxed{\mathbf{R}^j := \prod_{k=1}^{n_j} \mathbf{R}_1(\theta_{jk}) \mathbf{R}_3(\alpha_{jk}) = \mathbf{I}_3}. \quad (2.14)$$

If this equation is satisfied for each interior vertex of the sheet, it is ensured that no tearing will occur in the facets. Moreover, from Eq. (2.14) it can be proven that for non-trivial folding motion, any interior fold intersection must have at least 4 incident creased folds. Considering Fig. 2.6, the trivial cases are:

- 1 incident fold ( $n_j = 1$ , Fig. 2.6a):

$$\theta_{j1} = 0 \quad (2.15)$$

thus no folding can occur;

- 2 incident fold ( $n_j = 2$ , Fig. 2.6b):

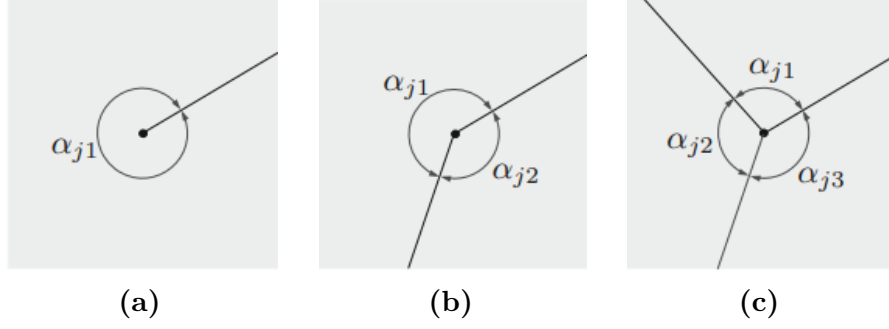
$$\begin{aligned} \theta_{j1} = \theta_{j2} = 0; \quad \alpha_{j1} \neq \pi \\ \theta_{j1} = \theta_{j2}; \quad \alpha_{j1} = \pi \end{aligned} \quad (2.16)$$

thus no folding can occur *or* the two folds must be collinear, resulting in a single combined fold;

- 3 incident fold ( $n_j = 3$ , Fig. 2.6c):

$$\begin{aligned} \theta_{j1} = \theta_{j2} = \theta_{j3} = 0; \quad \alpha_{j1} \neq \pi, \alpha_{j2} \neq \pi, \alpha_{j3} \neq \pi \\ \theta_{j1} = \theta_{j2}, \theta_{j3} = 0; \quad \alpha_{j1} = \pi \\ \theta_{j2} = \theta_{j3}, \theta_{j1} = 0; \quad \alpha_{j2} = \pi \\ \theta_{j3} = \theta_{j1}, \theta_{j2} = 0; \quad \alpha_{j3} = \pi \end{aligned} \quad (2.17)$$

thus no folding can occur *or* two folds must be collinear, resulting in a single combined fold, while the third fold remains flat.



**Figure 2.6:** Interior fold intersection with: (a) 1 incident fold; (b) 2 incident folds; (c) 3 incident folds [1].

## 2.4 Folding Map Formulation

The objective of this Section is to determine the position vector of any point in the reference configuration  $\mathcal{S}_0$  to the current configuration  $\mathcal{S}_t$ , namely the *folding map*. To do so, the following steps are needed:

1. A facet in the sheet is assumed fixed in its reference configuration;
2. Paths  $\check{\gamma}^j(\eta) : [0,1] \rightarrow \mathcal{S}_0$ ,  $j = 1, \dots, N_{\mathcal{P}}$  connect the fixed facet to the others, crossing  $\check{n}_j$  folds;
3. The *folding transformation*, that is the formulation of the transformation associated with folding each of the creased folds crossed by the paths  $\check{\gamma}^j(\eta)$ , is determined;
4. Assembling all the folding transformations, the folding map of any point from  $\mathcal{S}_0$  to  $\mathcal{S}_t$  is finally obtained.

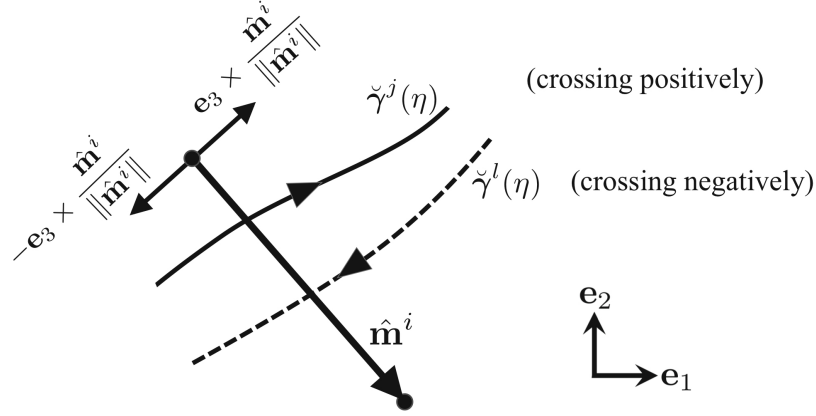
### 2.4.1 Parameters for the folding map formulation

The *input parameters* required to define the folding transformation of an origami sheet with creased folds are the facet connectivity matrix  $\mathbf{C}^{\mathcal{P}}$  and the fold angles  $\hat{\theta}_1, \dots, \hat{\theta}_{N_{\mathcal{F}}}$ . The *calculated parameters* required to define the folding map of an origami sheet with creased folds are the vectors along the fold lines crossed by  $\check{\gamma}^j(\eta)$  ( $\check{\mathbf{m}}^{j1}, \dots, \check{\mathbf{m}}^{j\check{n}_j}$ ), the fold angles of the folds crossed by  $\check{\gamma}^j(\eta)$  ( $\check{\theta}_{j1}, \dots, \check{\theta}_{j\check{n}_j}$ ) and the position vectors of points on the fold lines crossed by  $\check{\gamma}^j(\eta)$  ( $\check{\mathbf{b}}^{j1}, \dots, \check{\mathbf{b}}^{j\check{n}_j}$ ).

The vector  $\mathbf{C}^{\mathcal{P}} \in \mathbb{R}^{N_{\mathcal{P}} \times \max(\check{n}_j)}$  identifies and orders the folds crossed by each path  $\check{\gamma}^j(\eta)$ . Its components  $C_{jk}^{\mathcal{P}}$  ( $j = 1, \dots, N_{\mathcal{P}}, k = 1, \dots, \check{n}_j$ ) are defined as:

$$C_{jk}^{\mathcal{P}} = \text{Index of the } k\text{-th fold crossed by the path } \check{\gamma}^j(\eta) \text{ (multiplied by } -1 \text{ if the fold is negatively crossed by } \check{\gamma}^j(\eta)\text{)}.$$

As shown in Fig. 2.7, a path  $\check{\gamma}^j(\eta)$  crosses the  $i$ -th fold in the sheet positively if it crosses from the facet adjacent to the fold in the direction  $-\mathbf{e}_3 \times \hat{\mathbf{m}}^i$  to the facet in the direction  $\mathbf{e}_3 \times \hat{\mathbf{m}}^i$ , where  $\hat{\mathbf{m}}^i$  is fold vector along the length of the  $i$ -th fold in Eq. (2.2), and vice versa.



**Figure 2.7:** Positive and negative crossing of the fold by the path  $\check{\gamma}^j(\eta)$  [1].

The mapping from all the fold vectors  $\hat{\mathbf{m}}^1, \dots, \hat{\mathbf{m}}^{N_{\mathcal{F}}}$  to those along the fold lines crossed by  $\check{\gamma}^j(\eta)$  ( $\check{\mathbf{m}}^{jk} \in \text{span}(\mathbf{e}_1, \mathbf{e}_2)$ ) is defined such that the path  $\check{\gamma}^j(\eta)$  crosses it positively and it is given by:

$$\check{\mathbf{m}}^{jk} = \begin{cases} \hat{\mathbf{m}}^{C_{jk}^{\mathcal{P}}} & C_{jk}^{\mathcal{P}} > 0 \\ -\hat{\mathbf{m}}^{|C_{jk}^{\mathcal{P}}|} & C_{jk}^{\mathcal{P}} < 0 \end{cases}. \quad (2.18)$$

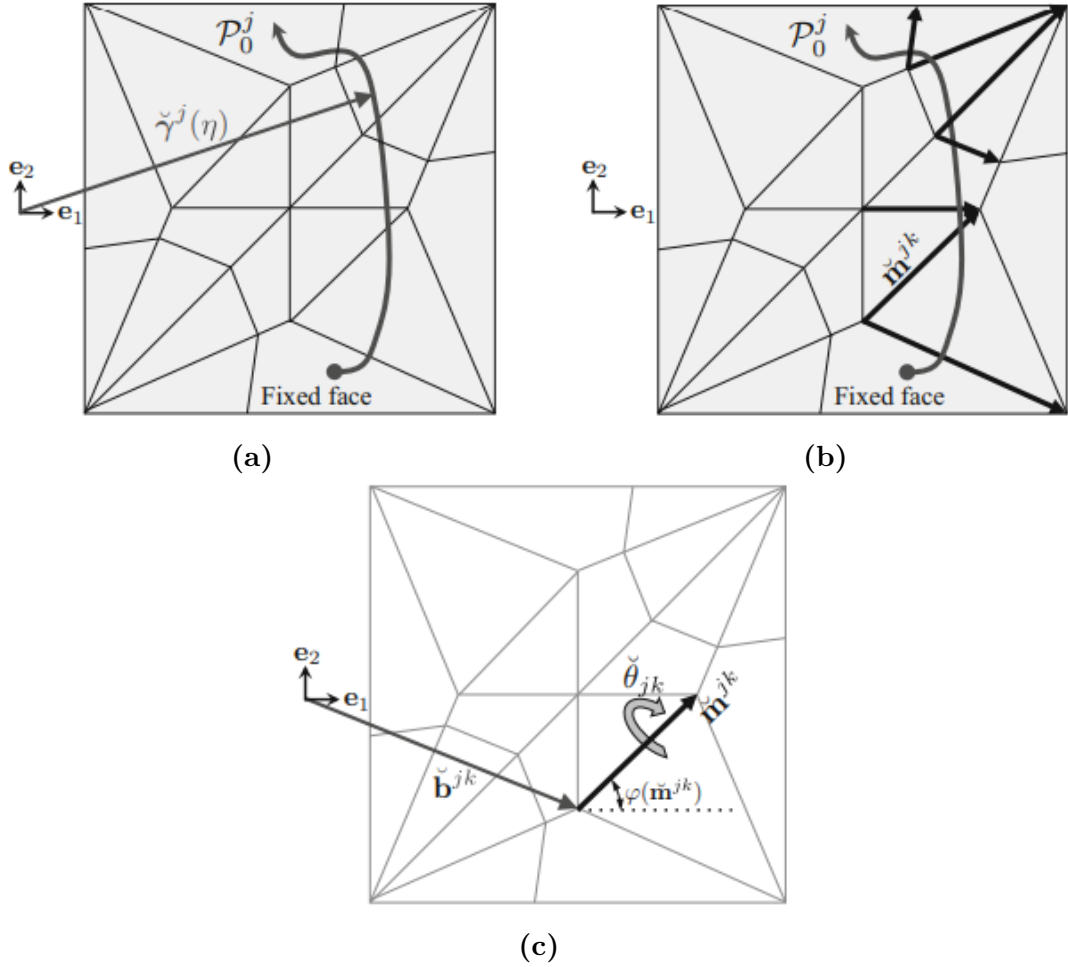
The mapping from all the fold angles  $\hat{\theta}_1, \dots, \hat{\theta}_{N_{\mathcal{F}}}$  to those crossed by  $\check{\gamma}^j(\eta)$  ( $\check{\theta}_{j1}, \dots, \check{\theta}_{j\check{n}_j}$ ) is:

$$\check{\theta}_{jk} = \hat{\theta}_{C_{jk}^{\mathcal{P}}}. \quad (2.19)$$

Lastly, to calculate the vector  $\check{\mathbf{b}}^{j1}, \dots, \check{\mathbf{b}}^{j\check{n}_j}$  it is necessary to consider the position vectors  $\hat{\mathbf{v}}^{11}, \dots, \hat{\mathbf{v}}^{N_{\mathcal{F}}1}$  in Eq. (2.1), using the following formula:

$$\check{\mathbf{b}}^{jk} = \hat{\mathbf{v}}^{|C_{jk}^{\mathcal{P}}|1}. \quad (2.20)$$

In Fig. 2.8 it is possible to notice all the parameters involved in the folding transformation of an origami sheet. In particular, Fig. 2.8a shows the path  $\check{\gamma}^j(\eta)$  that crosses  $\check{n}_j$  fold lines from the fixed facet to a facet  $\mathcal{P}_0^j$ , while Fig. 2.8b shows the vectors  $\check{\mathbf{m}}^{jk}$  along the  $k$ -th fold line crossed by  $\check{\gamma}^j(\eta)$ .



**Figure 2.8:** Parameters involved in the folding transformation of an origami sheet. (a) Path  $\check{\gamma}^j(\eta)$ ; (b) Vectors  $\check{\mathbf{m}}^{jk}$ ; (c) Folding transformation [1].



## 2.4.2 Working Principles of the Folding Map Formulation

Fig. 2.8c describes the folding transformation, which can be considered as a composition of rotation and translation transformations in the following order:

1. A translation of the axis of rotation by  $-\check{\mathbf{b}}^{jk}$  in order to cross the origin;
2. A rotation of  $-\varphi(\check{\mathbf{m}}^{jk})$  about  $\mathbf{e}_3$  of the axis of rotation to align it with  $\mathbf{e}_1$ ;
3. A rotation of  $\check{\theta}_{jk}$  about  $\mathbf{e}_1$  of the sheet;
4. A rotation of  $\varphi(\check{\mathbf{m}}^{jk})$  about  $\mathbf{e}_3$  of the axis of rotation to align it to its initial orientation;
5. A translation of the axis of rotation by  $\check{\mathbf{b}}^{jk}$  to its original position.

This procedure can be formulated in matrix form with the *folding transformation matrix*  $\check{\mathbf{H}}^{jk} \in \mathbb{R}^{4 \times 4}$ , given by:

$$\check{\mathbf{H}}^{jk} = \mathbf{T}(\check{\mathbf{b}}^{jk})\mathbf{Q}_3(\varphi(\check{\mathbf{m}}^{jk}))\mathbf{Q}_1(\check{\theta}_{jk})\mathbf{Q}_3^{-1}(\varphi(\check{\mathbf{m}}^{jk}))\mathbf{T}^{-1}(\check{\mathbf{b}}^{jk}), \quad (2.21)$$

where  $\mathbf{T}(\mathbf{b}) \in \mathbb{R}^{4 \times 4}$  is the transformation matrix associated with the translation by vector  $\mathbf{b} \in \mathbb{R}^{3 \times 3}$  with components  $b_1, b_2, b_3$ , given by:

$$\mathbf{T}(\mathbf{b}) = \left[ \begin{array}{ccc|c} 1 & 0 & 0 & b_1 \\ 0 & 1 & 0 & b_2 \\ 0 & 0 & 1 & b_3 \\ \hline 0 & 0 & 0 & 1 \end{array} \right] = \begin{bmatrix} \mathbf{I}_3 & \mathbf{b} \\ \mathbf{0}_3^\top & 1 \end{bmatrix}. \quad (2.22)$$

$\mathbf{Q}_1(\phi) \in \mathbb{R}^{4 \times 4}$  is the transformation matrix associated with a rotation by  $\phi$  radians about an axis of rotation aligned to  $\mathbf{e}_1$ , given by:

$$\mathbf{Q}_1(\phi) = \left[ \begin{array}{ccc|c} 1 & 0 & 0 & 0 \\ 0 & \cos(\phi) & -\sin(\phi) & 0 \\ 0 & -\sin(\phi) & \cos(\phi) & 0 \\ \hline 0 & 0 & 0 & 1 \end{array} \right] = \begin{bmatrix} \mathbf{R}_1(\phi) & \mathbf{0}_3 \\ \mathbf{0}_3^\top & 1 \end{bmatrix}. \quad (2.23)$$

$\mathbf{Q}_3(\phi) \in \mathbb{R}^{4 \times 4}$  is the transformation matrix associated with a rotation by  $\phi$  radians about an axis of rotation aligned to  $\mathbf{e}_3$ , given by:

$$\mathbf{Q}_3(\phi) = \left[ \begin{array}{ccc|c} \cos(\phi) & -\sin(\phi) & 0 & 0 \\ -\sin(\phi) & \cos(\phi) & 0 & 0 \\ 0 & 0 & 1 & 0 \\ \hline 0 & 0 & 0 & 1 \end{array} \right] = \begin{bmatrix} \mathbf{R}_3(\phi) & \mathbf{0}_3 \\ \mathbf{0}_3^\top & 1 \end{bmatrix}. \quad (2.24)$$

From here, it is possible to obtain the folding map used to transform the position vector of any point in the sheet from the reference configuration  $\mathcal{S}_0$  to a current configuration  $\mathcal{S}_t$  with the following equation:

$$\boxed{\begin{bmatrix} \mathbf{x} \\ 1 \end{bmatrix}} = \left( \prod_{k=1}^{\check{n}_j} \check{\mathbf{H}}^{jk} \right) \begin{bmatrix} \mathbf{X} \\ 1 \end{bmatrix}, \quad (2.25)$$

where  $\mathbf{X} \in \text{span}(\mathbf{e}_1, \mathbf{e}_2)$  is the position vector of a point in a facet  $\mathcal{P}_0^j \subset \mathcal{S}_0$  and  $\mathbf{x} \in \mathbb{R}^3$  is the position vector of the same point in a facet  $\mathcal{P}_t^j \subset \mathcal{S}_t$ .

## 2.5 Computational Implementation of the Model

After having introduced the theory behind the kinematics of origami structures with creased folds it is now possible to develop a procedure to simulate the folding motion of an origami sheet on MATLAB. However, in order to do so, it is necessary to partition the continuous folding motion of the sheet into *increments*, hence the simulation is performed by incrementally updating the values of the fold angles using input guess increments, in agreement with Peraza et al. [1, 8].

The input of the models are:

- The fold pattern data, that is:
  - Position vectors of the vertices  $\mathbf{v}^1, \dots, \mathbf{v}^{N_I+N_B}$  in Section 2.2;
  - Fold connectivity matrix  $\mathbf{C}^{\mathcal{F}}$  in Section 2.2;
  - Fold intersection connectivity matrix  $\mathbf{C}^{\mathcal{F}}$  in Section 2.2;
- The guess increment vector for the fold angles  $\Delta \hat{\boldsymbol{\theta}}^l \in \mathbb{R}^{N_{\mathcal{F}}}$ , with components  $\Delta \hat{\theta}_1^l, \dots, \Delta \hat{\theta}_{N_{\mathcal{F}}}^l$ ,  $l = 1, \dots, N_{inc}$ , where  $N_{inc}$  is the number of guess increments.

Let  $\hat{\boldsymbol{\theta}}^l \in \mathbb{R}^{N_{\mathcal{F}}}$  be the vector whose components correspond to the values of the fold angles at the  $l$ -th increment  $\hat{\theta}_1^l, \dots, \hat{\theta}_{N_{\mathcal{F}}}^l$ . This vector must satisfy the kinematic constraints in Section 2.3, be greater than the *lower bound vector*  $\hat{\boldsymbol{\theta}}^L \in \mathbb{R}^{N_{\mathcal{F}}}$  and lower than the *upper bound vector*  $\hat{\boldsymbol{\theta}}^U \in \mathbb{R}^{N_{\mathcal{F}}}$ , considering that  $\hat{\boldsymbol{\theta}}^l \in [-\pi, \pi]$  to prevent self-intersection of the pairs of facets connected by each fold.

The configurations obtained by the simple addition of the guess increment for the fold angles may not satisfy the kinematic constraints, so an *iterative procedure* to apply corrections is needed, considering:

- $\hat{\boldsymbol{\theta}}^{l(k)} \in \mathbb{R}^{N_{\mathcal{F}}}$ : vector whose components correspond to the values of the fold angles at the  $k$ -th iteration of the  $l$ -th increment;
- $\boldsymbol{\mathfrak{R}}(\hat{\boldsymbol{\theta}}^{l(k)}) = \mathbf{R}^j(\hat{\boldsymbol{\theta}}^{l(k)}) - \mathbf{I}_3 \in \mathbb{R}^{3N_{\mathcal{I}}+2N_{\mathcal{F}}}$ ,  $j = 1, \dots, N_{\mathcal{I}}$ : residual vector from the loop closure constraint in Section 2.3.2, where the  $3N_{\mathcal{I}}$  comes from the kinematic constraint, while  $2N_{\mathcal{F}}$  from the upper and lower bounds of each fold angle.

### 2.5.1 Iterative Process

The numerical procedure to determine valid configurations at each increment in the folding motion for origami sheets with creased folds (ref. to Fig. 2.9) is the following:

1. Knowing  $\Delta\hat{\boldsymbol{\theta}}^l$  and the initial point  $\boldsymbol{\mathfrak{R}}(\hat{\boldsymbol{\theta}}^{l-1})$ , at the start of each increment it is possible to calculate the projected fold angle increment  $\Delta\hat{\boldsymbol{\theta}}^{l*}$  from the equation:

$$\Delta\hat{\boldsymbol{\theta}}^{l*} = \left( \mathbf{I}_{N_{\mathcal{F}}} - \left( \frac{\partial \boldsymbol{\mathfrak{R}}(\hat{\boldsymbol{\theta}}^{l-1})}{\partial \hat{\boldsymbol{\theta}}} \right)^\dagger \left( \frac{\partial \boldsymbol{\mathfrak{R}}(\hat{\boldsymbol{\theta}}^{l-1})}{\partial \hat{\boldsymbol{\theta}}} \right) \right) \Delta\hat{\boldsymbol{\theta}}^l, \quad (2.26)$$

where  $(\cdot)^\dagger$  is the Moore-Penrose pseudoinverse [58], a linear algebra technique used to approximate the inverse of non-invertible matrices, equal to the inverse if the matrix is invertible.

2. Knowing the fold angles of the previously determined configuration  $\hat{\boldsymbol{\theta}}^{l-1}$ , the guess fold angle of iteration 0 ( $\hat{\boldsymbol{\theta}}^{l(0)}$ ) is calculated from:

$$\hat{\boldsymbol{\theta}}^{l(0)} = \hat{\boldsymbol{\theta}}^{l-1} + \Delta\hat{\boldsymbol{\theta}}^{l*}. \quad (2.27)$$

3. If  $\|\boldsymbol{\mathfrak{R}}(\hat{\boldsymbol{\theta}}^{l(0)})\|/(3N_{\mathcal{I}} + 2N_{\mathcal{F}}) < tol1$ , where  $tol1$  is a numerical tolerance,  $\hat{\boldsymbol{\theta}}^l$  is set to  $\hat{\boldsymbol{\theta}}^{l(0)}$  and it is possible to exit from the process.
4. If  $\|\boldsymbol{\mathfrak{R}}(\hat{\boldsymbol{\theta}}^{l(0)})\|/(3N_{\mathcal{I}} + 2N_{\mathcal{F}}) \geq tol1$  it is possible to determine the correction of the fold angles at iteration  $k$  ( $\Delta\hat{\boldsymbol{\theta}}^{l(k)}$ ) from the equation:

$$\Delta\hat{\boldsymbol{\theta}}^{l(k)} = - \left( \frac{\partial \boldsymbol{\mathfrak{R}}(\hat{\boldsymbol{\theta}}^{l(k)})}{\partial \hat{\boldsymbol{\theta}}} \right)^\dagger \boldsymbol{\mathfrak{R}}(\hat{\boldsymbol{\theta}}^{l(k)}). \quad (2.28)$$

5. Finally, the fold angles are corrected as follows:

$$\hat{\boldsymbol{\theta}}^{l(k+1)} = \hat{\boldsymbol{\theta}}^{l(k)} + \Delta\hat{\boldsymbol{\theta}}^{l(k)}. \quad (2.29)$$

6. The procedure is repeated from point 4 until

$$\|\mathfrak{R}(\hat{\boldsymbol{\theta}}^{l(k+1)})\|/(3N_{\mathcal{I}} + 2N_{\mathcal{F}}) < tol1 \quad \text{or} \quad \|\Delta\hat{\boldsymbol{\theta}}^{l(k)}\|/N_{\mathcal{F}} < tol2 \quad (2.30)$$

(where  $tol2$  is another numerical tolerance), when  $\hat{\boldsymbol{\theta}}^l$  is set to  $\hat{\boldsymbol{\theta}}^{l(k+1)}$ .

## 2.6 Simulation Example of the Kinematic Model

This Section shows an example of the described model for kinematic simulation of origami with creased folds, considering the sheet with eight creased folds, enumerated in counterclockwise order, converging in one interior fold intersection ( $N_{\mathcal{I}} = 1$ ) in Fig. 2.10a. The folded configuration shown in Fig. 2.10b are obtained through the following guess increment for the fold angles:

$$\Delta\hat{\boldsymbol{\theta}}^l = \frac{\pi}{40}[0 \ 0 \ 1 \ 0 \ 0 \ 0 \ 1 \ 0]^{\top}, \quad (2.31)$$

while the folded configuration shown in Fig. 2.10c are obtained through:

$$\Delta\hat{\boldsymbol{\theta}}^l = \frac{\pi}{40}[0 \ 1 \ 0 \ 0 \ 0 \ 1 \ 0 \ 0]^{\top}. \quad (2.32)$$

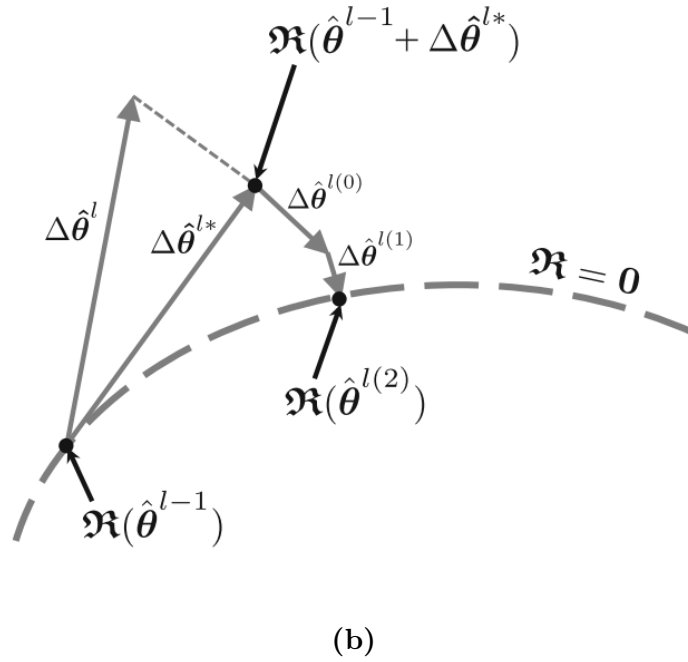
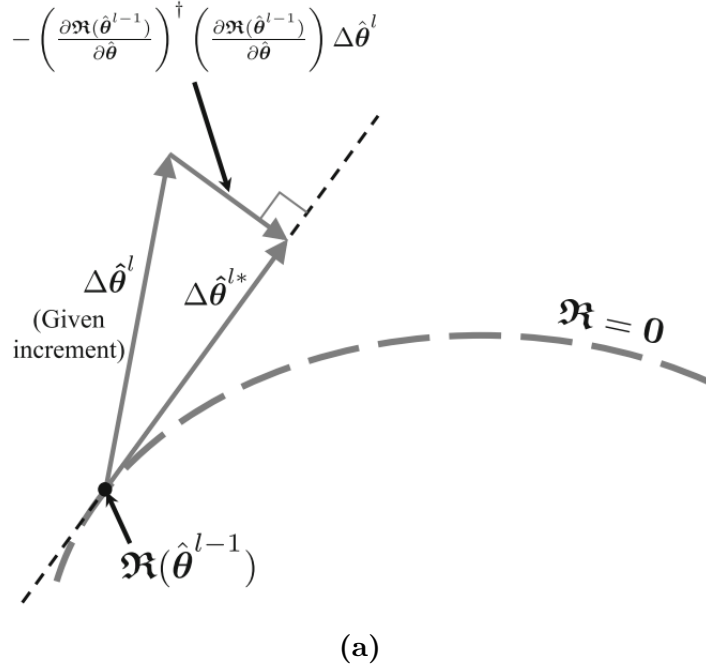
These represent simple cases, where the fold angle correction procedure converged before performing an initial correction iteration (i.e.  $\|\mathfrak{R}(\hat{\boldsymbol{\theta}}^{l(0)})\|/(3N_{\mathcal{I}} + 2N_{\mathcal{F}}) < tol1$  for  $l = 1, \dots, 20$ ).

Fig. 2.10d shows the trend of fold angles and sum of guess increments for the fold angles vs. increment number of a more complex folding motion that requires the iterative correction process in Section 2.5.1. In this case, the guess increment for the fold angles is:

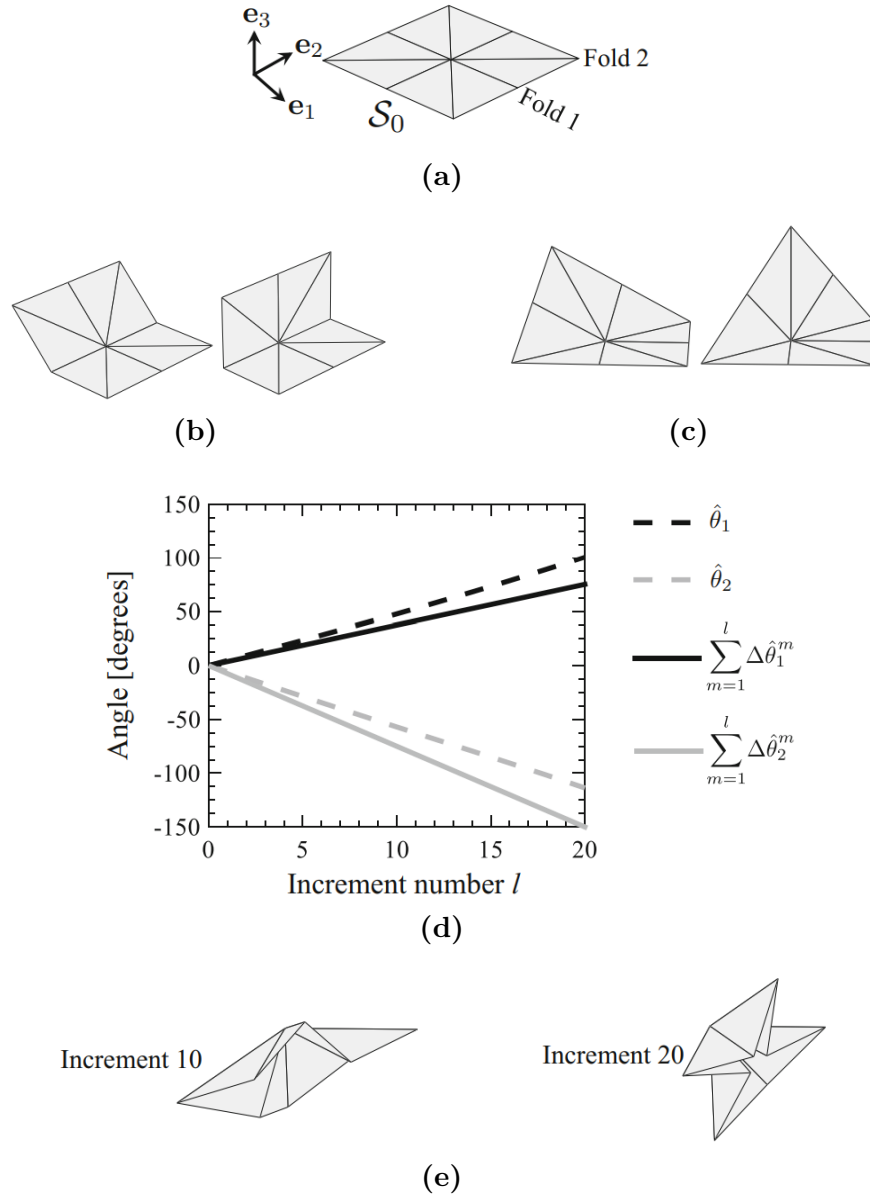
$$\Delta\hat{\boldsymbol{\theta}}^l = \frac{5\pi}{240}[1 \ -2 \ -1 \ -2 \ 1 \ -2 \ 1 \ -2]^{\top}. \quad (2.33)$$

From the graph, it can be confirmed that the fold angles obtained from the iterative process are different from the simple addition of guess increments for the fold angles (without considering the kinematic constraints), as stated in Section 2.3. In Fig. 2.10e it is possible to observe the final configurations of the sheet obtained from the guess increments for the fold angles in Eq. (2.33).

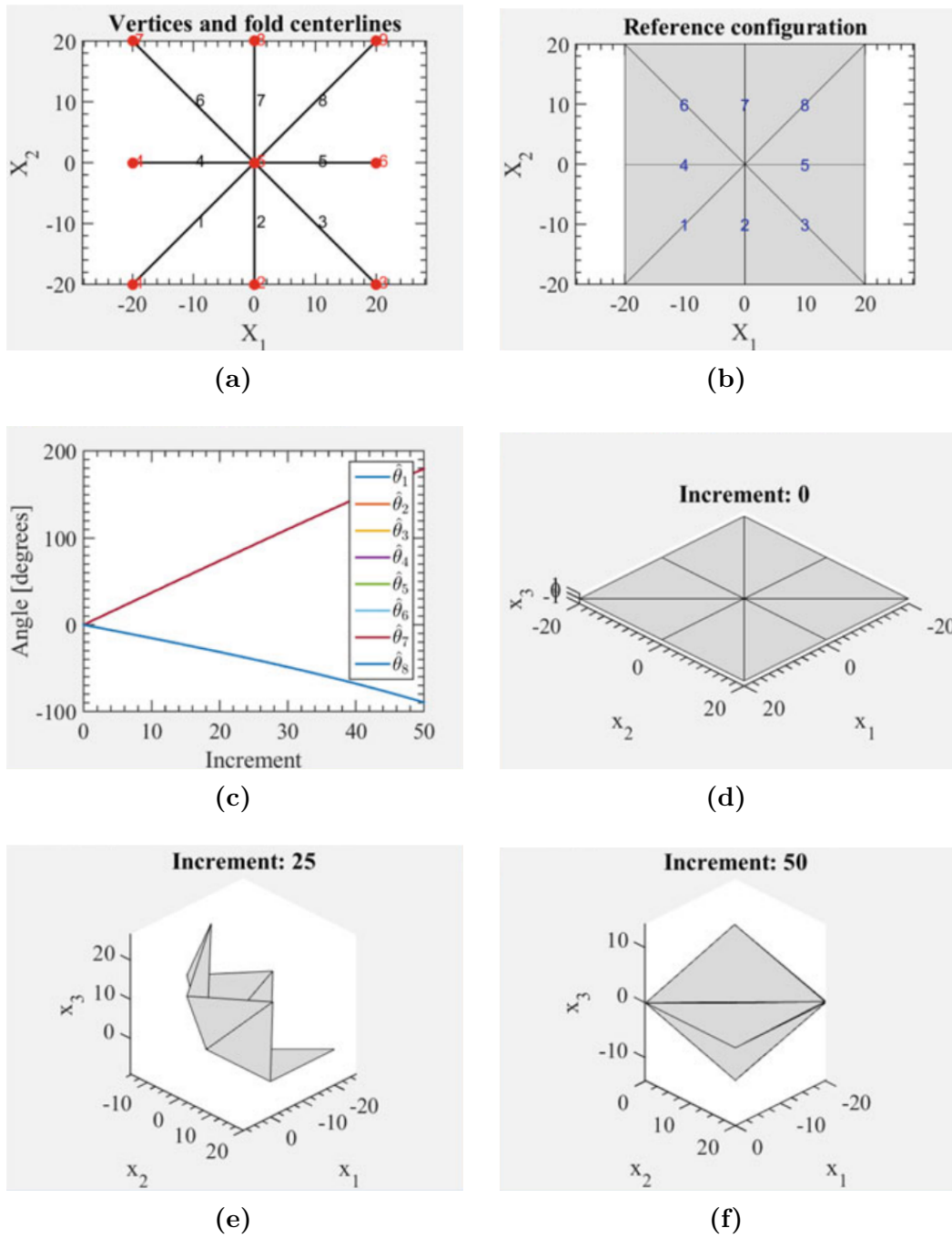
Lastly, Fig. 2.11 presents the outputs obtained from the implementation of the described kinematic model on MATLAB for the same sheet with eight creased folds described above, provided in the Supplement Data in Reference [1].



**Figure 2.9:** Numerical procedure to determine valid configurations at each increment in the folding motion for origami sheets with creased folds. (a) Illustration of the hypersurface  $\mathfrak{R} = \mathbf{0}_{3N_I+2N_F}$ , the initial point  $\mathfrak{R}(\hat{\theta}^{l-1})$  and the projected fold angle increment  $\Delta\hat{\theta}^{l*}$ ; (b) Subsequent corrections  $\Delta\hat{\theta}^{l(k)}$  [1].



**Figure 2.10:** (a) Configurations of a sheet with eight creased folds, enumerated in counterclockwise order, converging in one interior fold intersection ( $N_{\mathcal{I}} = 1$ ); (b) Folded configuration from the guess increment in Eq. (2.31); (c) Folded configuration from the guess increment in Eq. (2.32); (d) Trend of fold angles and sum of guess increments for the fold angles vs. increment number of the more complex guess increment in Eq. (2.33); (e) Final configurations of the sheet obtained from the guess increments in Eq. (2.33) [1].



**Figure 2.11:** Output plots of the kinematic model implemented on MATLAB from the Supplement Data in Reference [1] for a sheet with eight creased folds: (a) Vertices and fold lines positions; (b) Reference configuration  $\mathcal{S}_0$ ; (c) Fold angles vs. number of increments; (d),(e),(f) Configurations at the requested increments.

## Chapter 3

# Topology Optimization Based on Linear Analysis

To improve on the kinematic approach and discuss the mechanics of non-rigid origami structures, in this Chapter, a topology optimization method based on linear analysis is described.

### 3.1 Introduction on Topology Optimization

*Topology optimization* [59] is a mathematical method that consists in optimizing the spatial distribution of material within a defined domain, for given loads and boundary conditions, in order to minimize a predefined characteristic of the system. The methods used for the optimization can be *gradient-based* or *non-gradient-based*. Two examples of gradient-based methods are the Method of Moving Asymptotes (MMA) as implemented in Svanberg's MATLAB code [53] and the Sequential Quadratic Programming (SQP) introduced by Wilson [60]. MMA uses a special type of convex approximation. It replaces difficult nonlinear problems with a sequence of strictly convex approximating subproblems. It is able to separate the variables of a problem, linearize it, avoid inversions in large matrix and restore symmetry. SQP is an iterative method for constrained nonlinear optimization for which the objective function and the constraints need to be twice continuously differentiable. Using the MATLAB function "fmincon", it solves a sequence of optimization subproblems, each of which optimizes a quadratic model of the objective subject to a linearization of the constraints. An example of a non-gradient-based method is the Genetic Algorithm (GA) [61], which solves both constrained and unconstrained optimization problems based on biologically inspired operators such as mutation, crossover and selection (described in Appendix A).



Topology optimization has been widely used in aerospace applications [62, 63, 64, 65], mainly in the design process. However, due to the non-conventional shapes that this process leads to, it is necessary to add constraints to the formulation in order to permit manufacturability.

In general, a topology optimization problem consists in the minimization of an objective function subject to some constraints, and its main parameters are:

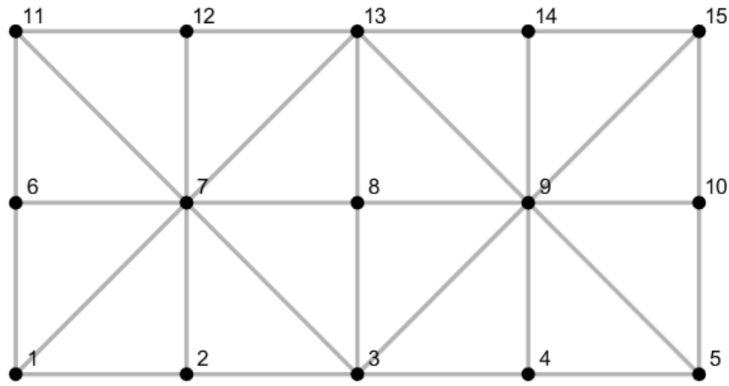
- The *objective function*: characteristic that needs to be minimized to enhance the performances;
- The *design variable*: characteristic that leads to the minimization of the objective function, usually evaluated with Finite Element Methods (FEM);
- The *material distribution variable*: density of the material at each location, that can be either present (marked as 1), or absent (marked as 0);
- The *design space*: indicates the domain where the structure can be defined;
- The *constraints*: characteristics that the design must satisfy in order to obtain a valid configuration.

Usually, structural topology optimization targets the rigidity of the structure by minimizing compliance or strain energy [11]. Another valid choice, which will be used in this Chapter, involves the design of compliant mechanisms, a kind of mechanisms that achieve mobility through compliance, i.e. elastic deformation of one or more of their links. The objective function in this case could be displacements, shape, modal controllability, and geometric/mechanical advantages.

The design approach presented in this Chapter was used by Fuchi et al. [11], where a procedure to find an origami crease pattern that achieves desired deformation through folding for a given input force was provided, applying a constraint on the number of fold lines, but penalizing the stretching phenomenon. This work aims to improve this study by introducing axial rigidity as a design variable, thus allowing each truss to stretch in an optimized way. The objective is therefore to find both the axial rigidity distribution of the trusses and the origami crease pattern that maximizes the displacement at set locations. The Method of Moving Asymptotes (MMA) is used to perform the optimization.

### 3.2 Linear truss model

In this Section, a linear truss method is used to study small displacements and small rotations in flexible origami structures. Fig. 3.1 shows a general starting configuration of origami with this method. Each fold line and external segment in the sheet (grey lines in Fig. 3.1) is represented by a truss element, while each vertex, i.e. each node in the starting configuration (black points in Fig. 3.1) is represented by a pin-joint, connection between the trusses that allow only relative rotation about a single axis.



**Figure 3.1:** Reference grid of an origami sheet in the linear truss method.

Following the method introduced by Schenk and Guest [66], modeling the folding patterns as a pin-jointed framework allows the use of established structural engineering methods to study the mechanics of origami. The mechanical properties of the Reference grid are described by introducing a stiffness formulation, that relates the nodal displacements  $\mathbf{u}$  with the applied nodal forces  $\mathbf{F}$  through the material stiffness matrix  $\mathbf{K}$ :

$$\mathbf{K}\mathbf{u} = \mathbf{F}. \tag{3.1}$$

The matrix  $\mathbf{K}$  can be obtained from:

$$\mathbf{K} = \mathbf{K}_J + \mathbf{K}_T, \tag{3.2}$$

where  $\mathbf{K}_J$  and  $\mathbf{K}_T$  are the stiffness matrices obtained from the fold constraint [6] and the truss model respectively.

In this Chapter, a *linear analysis* will be carried out, i.e. the stiffness matrix remains constant and independent of  $\mathbf{u}$  during the formulation. This has the advantage of having a low computational cost, but the drawback is that the applied loads are required to be small, leading to small deformations. Also, this analysis cannot be used in origami designs that involve a sequence of folding with altering overall directions of deformation. Even though origami folds usually generate large deformation, this analysis can determine the optimal topology for the initiation of folding.

Lastly, the thickness of the origami structure is not considered in the described linear model, and the trusses are one-dimensional. However, thickness has been studied by Zirbel et al. [45].

### 3.3 Optimization Methods

#### 3.3.1 Fold Constraint

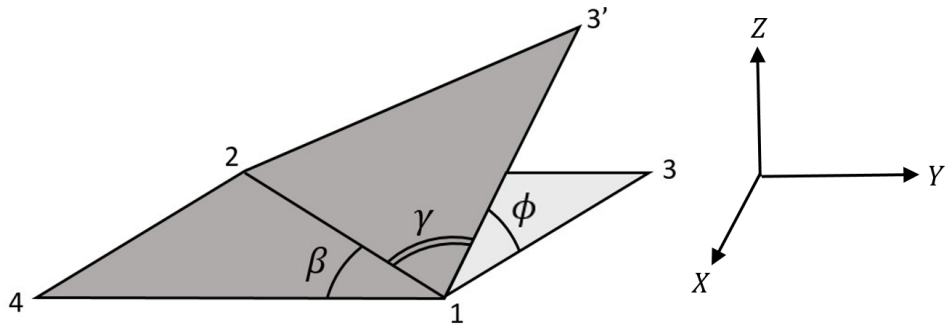
The folding mechanism is derived from constraints on the relationship between the dihedral angles ( $\phi$ ) and the nodal coordinates ( $\mathbf{X}$ ):

$$\mathbf{J} = \frac{d\phi}{d\mathbf{X}}. \quad (3.3)$$

This Jacobian can be evaluated considering each dihedral angle  $\phi$  relative to adjacent facets, like in Fig. 3.2, that is:

$$\phi = \sin^{-1} \left[ \frac{\mathbf{v}_{12} \times (\mathbf{v}_{14} \times \mathbf{v}_{12}) \cdot (\mathbf{v}_{12} \times \mathbf{v}_{13'})}{\sin \gamma \sin \beta \|\mathbf{v}_{12}\|^3 \|\mathbf{v}_{13'}\| \|\mathbf{v}_{14}\|} \right] \quad (3.4)$$

where  $\mathbf{v}_{ij}$  is the vector from node  $i$  to  $j$ .



**Figure 3.2:** Scheme of the origami element in the linear truss model.

For each fold line  $k$ , the fold stiffness  $K_J^k$  can be computed as:

$$K_J^k = (J^k)^T G_k J^k, \quad (3.5)$$

where  $k = 1, \dots, N_f$ ,  $N_f$  is the number of fold lines and  $G_k$  is the fold stiffness relative to folding, hence it is equal to zero in the trusses at the boundaries. By changing this coefficient, it is possible to regulate the importance of the fold constraint along each fold line  $k$ : folding is allowed using a small  $G_k$  ( $G_{soft}$ ), while it is prevented using a large  $G_k$  ( $G_{stiff}$ ).

Fuchi et al. [11] proposed a design method for origami structures using topology optimization considering the fold stiffness  $G$  as a design element, to discover the *optimized crease pattern*, i.e. the configuration of fold lines in the origami that allows to achieve the greatest actuation. Only the fold lines required to obtain this actuation are revealed after the analysis, considering a constraint on the maximum allowable number of fold lines that can be active (i.e. soft folds with small values of  $G$  that allow folding), hiding the remaining inactive fold lines (i.e. stiff folds with large values of  $G$  that do not allow folding).

The fold stiffness is represented by the following function

$$\boxed{G_k = 10^{a_0 + \alpha_k(a_1 - a_0)}}, \quad (3.6)$$

which is continuous and differentiable to allow to use gradient-based optimization algorithms. The design variable  $\alpha_k \in [0,1]$  (i.e. the fold stiffness exponent associated with folding) is considered, while  $a_0$  and  $a_1$  are constants and  $G_k$  takes on values from  $G_{soft} = 10^{a_0}$  to  $G_{stiff} = 10^{a_1}$ .

### 3.3.2 Truss Model with Axial Rigidity as Design Variable

The stiffness matrix from the truss model is the sum of every elemental stiffness matrix of the truss elements  $k_e^j$ , as follows:

$$\mathbf{K}_T = \sum_{j=1}^{N_e} k_e^j, \quad (3.7)$$

where  $k_e^j$  is a function of the axial rigidity  $EA_j$  ( $j = 1, \dots, N_e$ ) and  $N_e$  is the number of truss elements.

In this Chapter, the optimization method introduced by Fuchi et al. [11] is improved to consider also the axial rigidity  $EA$  as a design variable, discovering both the optimized crease pattern and the *axial rigidity distribution*, i.e. the origami configuration in terms of the axial rigidity of each truss that allows to achieve the greatest actuation.

To obtain the axial rigidity, a density-based approach to topology optimization can be considered, similar to the modified SIMP approach applied by Andreassen et al. [57]. The design domain is discretized by finite elements with an assigned axial rigidity density  $\beta$ :

$$\boxed{EA_j = EA_{min} + \beta_j^p (EA_0 - EA_{min})}, \quad (3.8)$$

where  $N_e$  is the number of truss elements,  $EA_0$  the axial solid rigidity of the material (or maximum axial rigidity),  $EA_{min}$  the axial void rigidity (or minimum axial rigidity) assigned to avoid singularity and  $p$  a penalization factor that ensures black-and-white solutions.

The difference between this approach and the one used by Andreassen et al. [57] is that the axial rigidity is the design variable instead of the Young's Modulus. This procedure leads to manufacturing advantages of the trusses in the structure since it is possible to decide whether to act on their Young's Modulus (changing material) or on their area (keeping the same material).

Lastly, in the non-modified SIMP approach [67, 56], elements with zero stiffness are avoided by imposing a limit value on the densities  $\beta$ . In this method, this is done by the factor  $EA_{min}$ , which allows for a more straightforward implementation.

### 3.4 Optimization Framework

The aim of this optimization is to find the axial rigidity distribution of the trusses and the origami crease pattern that maximizes the displacement at set locations, achieving the desired deformations through folding and stretching for a given input force.

The *optimization problem* is the following:

Find  $\mathbf{x} = \alpha_1, \dots, \alpha_{N_f}, \beta_1, \dots, \beta_{N_e}$  that

Minimize  $f = -\mathbf{c}^T \mathbf{u}$

Subject to

$$g_1 = v_{0,1} - \frac{1}{N_f} \sum_{i=1}^{N_f} x_i \leq 0; \quad g_2 = v_{0,2} - \frac{1}{N_e} \sum_{i=N_f+1}^{N_f+N_e} x_i \leq 0; \quad (3.9)$$

$$0 \leq x_i \leq 1; \quad \forall i = 1, \dots, N_f + N_e;$$

$$\mathbf{K}\mathbf{u} = \mathbf{F}.$$

$f$  is the objective function, hence minimizing  $f$  means maximizing the displacements along a direction.  $\mathbf{c}$  is a vector that indicates the position of the prescribed nodes of the structure where the displacement needs to be computed, taking on values of either 1, -1 or 0 to indicate the associated direction of optimal actuation.  $g_1 \leq 0$  and  $g_2 \leq 0$  are the two inequality constraints:

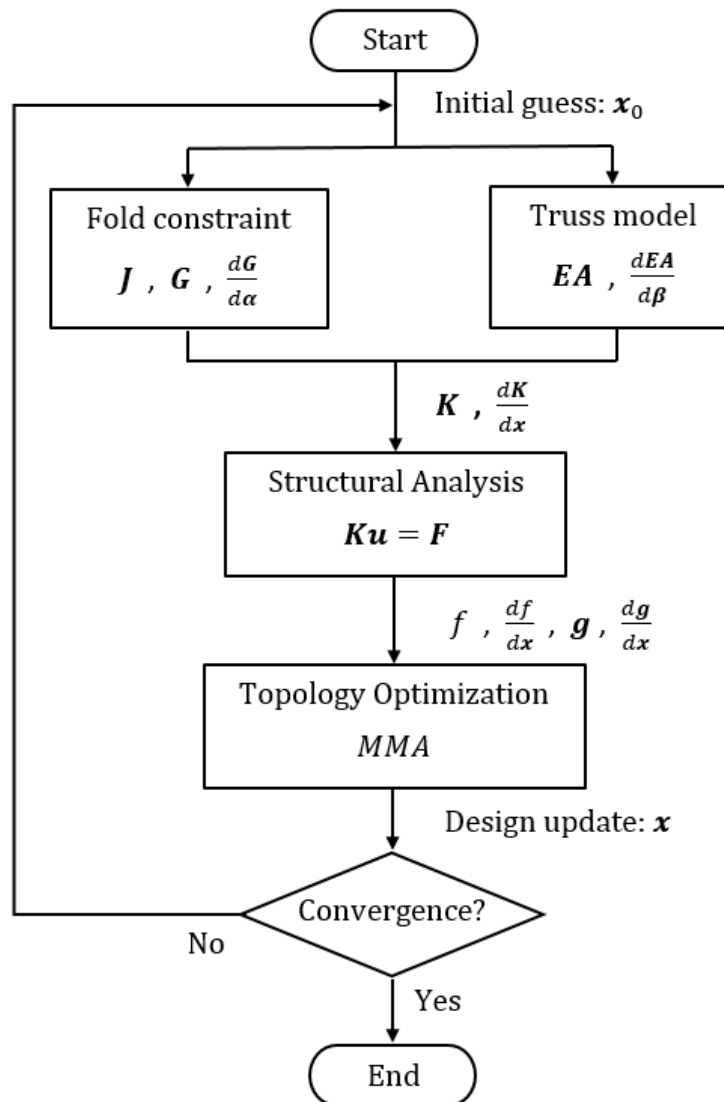
- $g_1$  is the constraint function for the active fold lines given a total of  $N_f$  available lines, while  $v_{0,1}$  is a factor that limits the fold stiffness of the fold lines.
- $g_2$  is the constraint function on the minimum axial rigidity given a total of  $N_e$  available lines, while  $v_{0,2}$  is a factor that limits the axial rigidity of the trusses.

The objective function varies according to two parameters:

- $l_0 = 1 - v_{0,1}$ : constraint on the number of active fold lines allowed. If  $l_0 = 0$  no fold line of the starting configuration is active, while if  $l_0 = 1$  all the fold lines are active;
- $m_0 = 1 - v_{0,2}$ : constraint on the number of trusses that are allowed to have a minimum axial rigidity. If  $m_0 = 0$  every truss member has axial rigidity  $EA = EA_0$ , while if  $m_0 = 1$  every truss member has axial rigidity  $EA = EA_{min}$ .

The value of the design variables is limited to take on values between 0 and 1 from the second constraint. The final constraint is the governing equation of the system.

A flowchart of the algorithm is shown in Fig. 3.3.



**Figure 3.3:** Flow chart of the linear optimization process.

### 3.4.1 Sensitivity analysis

To use the aforementioned gradient-based algorithms, a sensitivity analysis needs to be carried out, i.e. the evaluation of how and how much the parameters of the optimization problem modify the objective function value and the point where the optimum is achieved, therefore the derivative of the objective function with respect to the design variables needs to be computed.

The addition of the second set of design variables implies the use of two constraint functions ( $g_1$  and  $g_2$ ), as shown in the Optimization Framework (3.9), that are assembled in a vector

$$\mathbf{g} = [g_1; g_2]. \quad (3.10)$$

However, a gradient-based optimization also needs the gradient of the constraint function with respect to the design variables

$$\frac{d\mathbf{g}}{d\mathbf{x}} = \begin{bmatrix} dg_1/d\mathbf{x} & dg_2/d\mathbf{x} \end{bmatrix}, \quad (3.11)$$

which is a matrix containing two vectors with the same length of  $\mathbf{x}$ . Considering the definition of  $\mathbf{x}$  in the Optimization Framework (3.9):

- $dg_1/d\mathbf{x}$  has the first  $N_f$  elements equal to  $-1/N_f$ , while the remaining  $N_e$  elements are equal to 0 since  $g_1$  does not depend on  $\beta_j$ ;
- $dg_2/d\mathbf{x}$  has the first  $N_f$  elements equal to 0 since  $g_1$  does not depend on  $\alpha_k$ , while the remaining  $N_e$  elements are equal to  $-1/N_e$ ;

The derivative of the stiffness matrix is found as:

$$\frac{\partial \mathbf{K}}{\partial \mathbf{x}} = \frac{\partial \mathbf{K}_J}{\partial \boldsymbol{\alpha}} + \frac{\partial \mathbf{K}_T}{\partial \boldsymbol{\beta}}, \quad (3.12)$$

where  $\boldsymbol{\alpha} = x_1, \dots, x_{N_f}$  and  $\boldsymbol{\beta} = x_{N_f+1}, \dots, x_{N_f+N_e}$ . The first term in Eq. (3.12) comes from the fold constraint

$$\frac{\partial \mathbf{K}_J}{\partial \alpha_k} = \mathbf{J}^T \frac{\partial G_k}{\partial \alpha_k} \mathbf{J} = \mathbf{J}^T \left[ (a_1 - a_0) 10^{a_0 + \alpha_k(a_1 - a_0)} \log(10) \right] \mathbf{J}, \quad (3.13)$$

while the second one from the truss model, using a chain rule

$$\frac{\partial \mathbf{K}_T}{\partial \beta_j} = \frac{\partial \mathbf{K}_T}{\partial EA_j} \frac{\partial EA_j}{\partial \beta_j}. \quad (3.14)$$



In Eq. (3.14),  $\partial\mathbf{K}_T/\partial EA_j$  is obtained from the gradient of the elemental stiffness matrix of the truss elements and

$$\frac{\partial EA_j}{\partial \beta_j} = p\beta_j^{(p-1)}(EA_0 - EA_{min}). \quad (3.15)$$

The gradient is obtained from the following adjoint method:

$$\mathbf{K} \left( \frac{\partial \mathbf{u}}{\partial x_i} \right) = - \left( \frac{\partial \mathbf{K}}{\partial x_i} \right) \mathbf{u}. \quad (3.16)$$

Solving Eq. (3.16) with  $\mathbf{u}$  and  $\mathbf{K}$  obtained from Eq.s (3.1) and (3.2) respectively,  $\partial\mathbf{u}/\partial x_i$  is found, and the gradients  $df/dx_i$  can be computed as:

$$\frac{df}{dx_i} = - \left( \frac{\partial \mathbf{u}}{\partial x_i} \right)^T \mathbf{c}. \quad (3.17)$$

Lastly, the optimization problem can be solved using the Method of Moving Asymptotes (MMA).

The whole process, schematized in Fig. 3.3, is described here:

1. At the start of each iteration,  $\mathbf{G}$  and  $\mathbf{EA}$  along with their gradients, are computed from the fold constraint and the truss model respectively, in order to evaluate the stiffness matrix  $\mathbf{K}$  and its gradient from Eq.s (3.2) and (3.12).
2. Through Eq. (3.1), the structural analysis is carried out with the purpose of finding the nodal displacement field  $\mathbf{u}$ , while its gradient is obtained from Eq. (3.16);
3. The objective function and its gradient from Eq.s (3.9) and (3.17) are computed, as well as the constraint functions and their gradients;
4. The gradient-based topology optimization is carried out with the MMA method, in order to obtain the design variables  $x_i$  for the next iteration;
5. This iterative process is repeated until convergence is reached, i.e. the relative error between the objective functions at the current and at the previous iteration is lower than a set tolerance. Therefore, the axial rigidity distribution of the trusses and the origami crease pattern that maximizes the displacement at set locations are obtained.

## 3.5 Numerical Examples

The capabilities of the described method are shown through three different starting configurations, each of which is composed of truss members. In these examples, the stiffness coefficients are set to  $a_0 = 2$  and  $a_1 = 6$ . Moreover, the applied forces must be small enough to remain in a linear regime, thus obtaining displacements within a 10% range of the length of the structure.

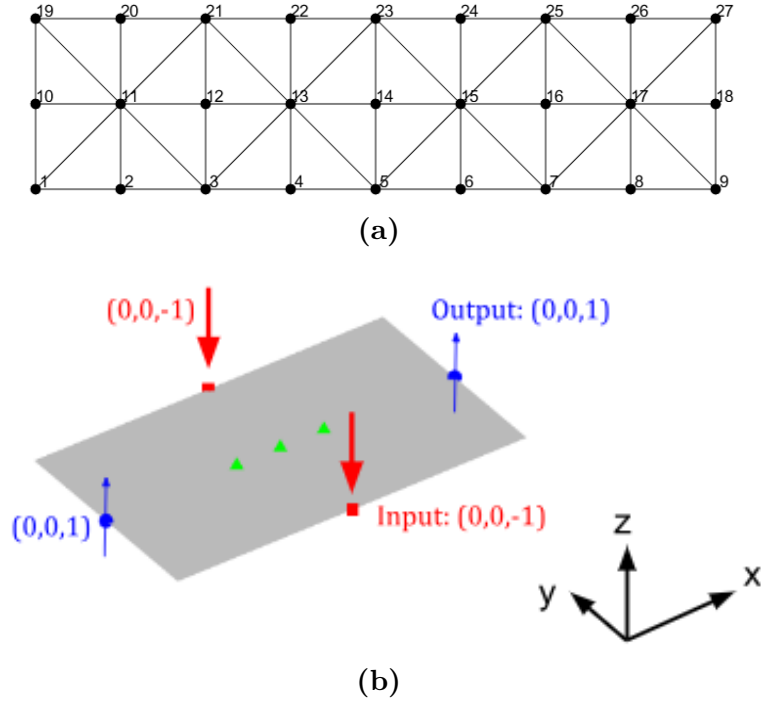
Each case is studied first using the Origami Mechanism Topology Optimizer (OMTO) in Reference [68] that uses only the fold stiffness exponent ( $\alpha$ ) as design variable and the constraint on the number of active fold lines allowed ( $l_0$ ), then with a modified OMTO, which uses the method described in this Chapter, that also considers the axial rigidity density ( $\beta$ ) as design variable and the constraint on the number of trusses that are allowed to have a minimum axial rigidity ( $m_0$ ).

In Reference [11],  $l_0$  alone is sufficient to carry out the analyses, while in this method also  $m_0$  needs to be used since there are now two sets of design variables. However, when  $m_0 = 0$  (or sufficiently close to 0 to avoid matrix singularities), the axial rigidity is kept equal among each truss, hence the second set of design variables is not considered and the same results as using only one set of design variables are obtained.

Lastly, the dashed and dotted-dashed lines in the optimized crease pattern indicate the mountain and valley folds of the origami, while the black and magenta lines in the optimized axial rigidity distribution indicate that the truss members have an axial rigidity  $EA = EA_0$  or  $EA = EA_{min}$  respectively.

### 3.5.1 Chomper Fold Pattern

The first example considers the *Chomper*, a famous fold pattern that has been used as a gripping mechanism for surgical tools [69], miniature robots [70], soft robotics [71] and deployable structures. The problem has 96 design variables ( $N_f = 38$  relative to  $\alpha$ ,  $N_e = 58$  relative to  $\beta$ ). Fig. 3.4a shows the reference truss distribution in the reference grid, while Fig. 3.4b shows the three-dimensional representation of the starting configuration with the load and boundary conditions.



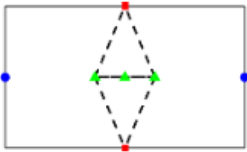
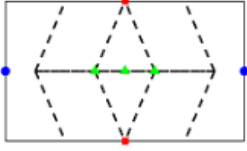
**Figure 3.4:** Starting configuration of the Chomper pattern. (a) Reference grid; (b) Load and boundary conditions ( $L_x = 1.7 \text{ m}$ ,  $L_y = 1.0 \text{ m}$ ,  $F = 100 \text{ N}$ ).

The green triangles are the fixed nodes, the red squares are the applied loads  $\mathbf{F}$  (with the direction indicated by the red arrows) and the blue dots are the nodes where the displacements  $\mathbf{u}$  need to be evaluated (with the direction indicated by the blue arrows). Lastly, the length of the structure is  $L_x = 1.7 \text{ m}$ , while its width is  $L_y = 1.0 \text{ m}$ .

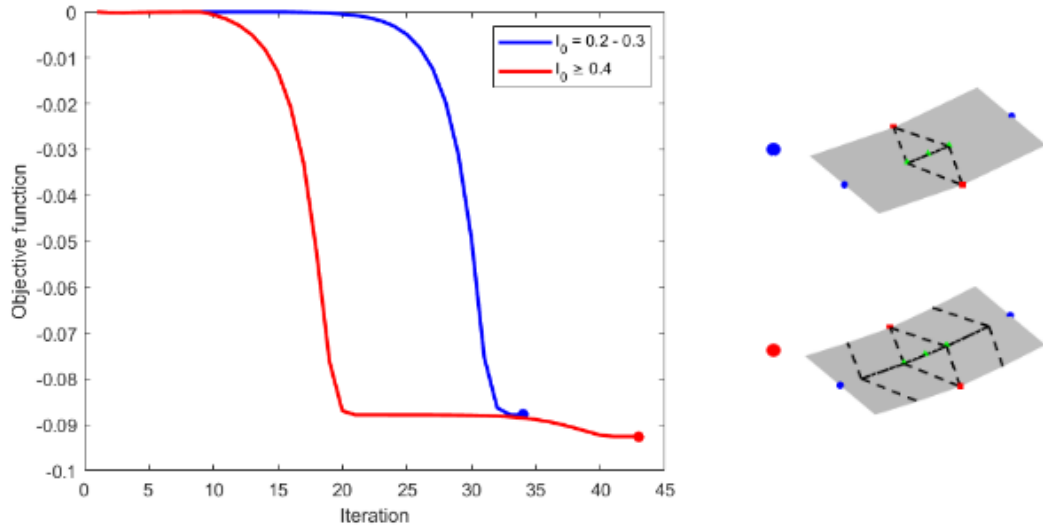
As a first example, the effect of the fold stiffness is studied. The load and boundary conditions in Fig. 3.4b are chosen so that the stretching of the trusses can be neglected in the small deformation analysis, in order to emphasize the effect of the folding of the sheet. Tab. 3.1 shows the results of the objective function and the optimized crease pattern. Under a fold line fraction ( $l_0$ ) of around 0.20 (corresponding to 6, i.e. 20% of the active fold lines allowed), the number of active folds is insufficient to obtain convergence.

As predictable, it can be noted that, if more fold lines are allowed (i.e. a higher fold line fraction  $l_0$  is considered), the value of the objective function decreases since the origami can be folded along more lines. This leads to an increase in the displacement field in the output nodes, while still remaining within a 10% range of the length of the structure, hence in a linear regime.

**Table 3.1:** Final configurations of the Chomper pattern (design variable:  $\alpha$ ). Dashed lines in Optimized Crease Pattern: active folds with  $G = G_{soft} = 10^2 \text{ Pam}^2$ .

$l_0$ [-]	Optimized Crease Pattern	$f$ [mm]
0.20		- 87.8
0.30		
$\geq 0.40$		- 92.6

In Fig. 3.5, the objective function over the iteration is displayed, underlying that the second crease pattern design leads to more significant actuation, for the cost of more iteration steps. A larger  $l_0$  has higher performances, but the drawback is that it leads to more design complexity.

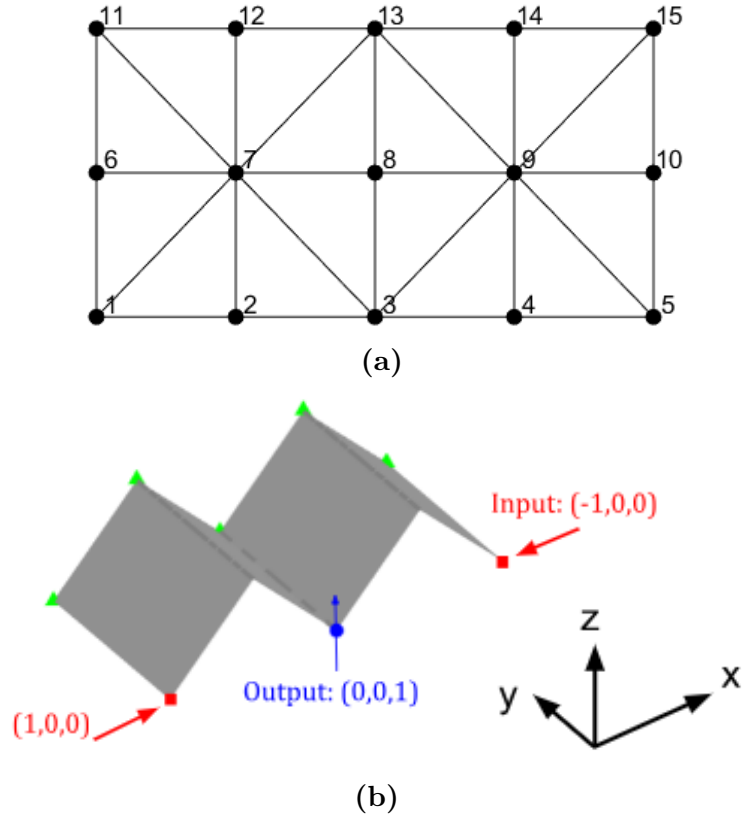


**Figure 3.5:** Objective function over iteration for different  $l_0$  in the Chomper pattern.

Since in this configuration approximately no stretching occurs, the value of the axial rigidity  $EA$ , along with the parameter  $m_0$ , have no influence over the results. Therefore, the outputs of the OMTO (where only  $\alpha$  is design variable) and the modified OMTO (where  $\alpha$  and  $\beta$  are design variables) are the same.

### 3.5.2 Zigzag Structure

The second example considers an already folded zigzag structure. The problem has 48 design variables ( $N_f = 18$  relative to  $\alpha$ ,  $N_e = 30$  relative to  $\beta$ ). The starting configuration, with the trusses distributed as in Fig. 3.6a, is already folded around the second, third and fourth vertical lines as in Fig. 3.6b. Lastly, the length of the structure is  $L_x = 2.0$  m, while its width is  $L_y = 1.0$  m.


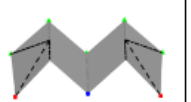







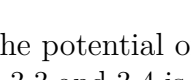


**Figure 3.6:** Starting configuration of the zigzag structure. (a) Reference grid; (b) Load and boundary conditions ( $L_x = 2.0$  m ,  $L_y = 1.0$  m ,  $F = 250$  N).

The effect of varying the axial rigidity is now studied. The load and boundary conditions in Fig. 3.6b are chosen so that folding can be neglected in the analysis, in order to emphasize the stretching of the trusses. In fact, folding is not the main phenomenon since changing the values of the coefficients in Eq. (3.6) has a limited influence over the results (remaining in a linear regime). Therefore, using only  $\alpha$  as design variable ( $m_0 = 0$ ) it is not possible to reach convergence. Nevertheless, keeping  $l_0$  constant and equal for example to 0.50 and increasing  $m_0$  the axial rigidity  $EA$  is allowed to vary among the trusses, therefore the effect of the addition of the second set of design variables can be assessed.

Considering values of  $m_0$  from 0.10 to 0.50, new optimized configurations can be analyzed, as shown in Tab. 3.2. Higher values of  $l_0$  and  $m_0$  are not recommended since they can lead to large displacements and uncertain results. Usually, the desired deformation is obtained with small  $l_0$  and  $m_0$ .

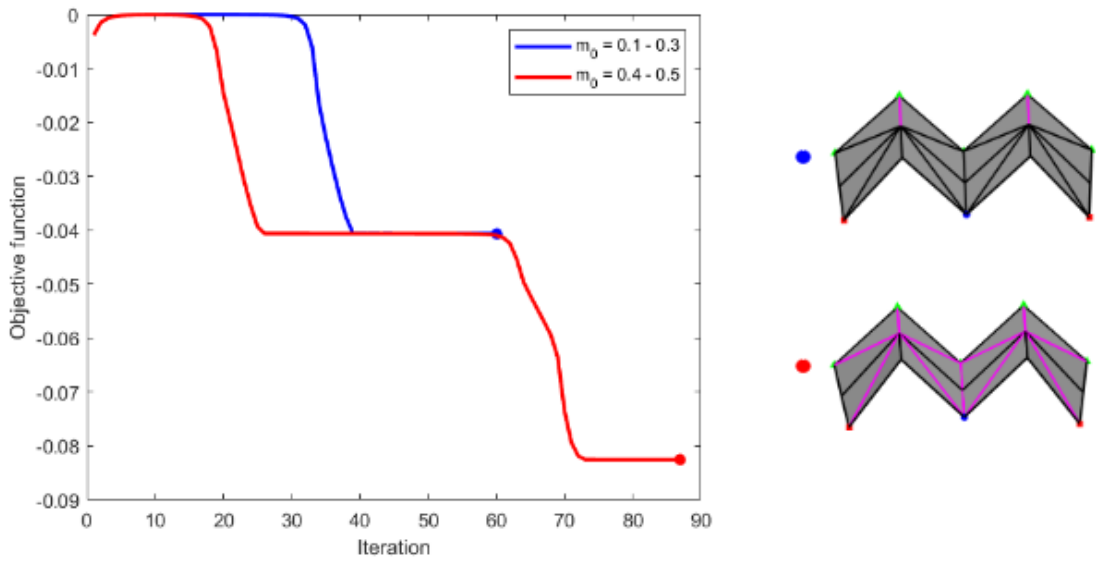
**Table 3.2:** Final configurations of the zigzag structure. Dashed lines in Optimized Crease Pattern: active folds with  $G = G_{soft} = 10^2 Pa \cdot m^2$ . Magenta and black lines in Axial Rigidity Distribution:  $EA = EA_{min} = 10^4 Pa \cdot m^2$  and  $EA = EA_0 = 10^8 Pa \cdot m^2$ .

$l_0$ [-]	$m_0$ [-]	Optimized Crease Pattern	Axial Rigidity distribution	$f$ [mm]
<b>1 set of design variables (<math>a</math>)</b>				
0.50	0	NO CONVERGENCE	NO CONVERGENCE	/
<b>2 sets of design variables (<math>a, \beta</math>)</b>				
0.50	0.10			<b>- 40.60</b>
	0.20			
	0.30			
0.50	0.40			<b>- 82.50</b>
	0.50			

These results underline the potential of the method. Even if the optimization problem described in Section 3.3 and 3.4 is more complex than the one in Reference [11], using also the axial rigidity as a design variable it is now possible to study new configurations.

Tab. 3.2 displays that, if  $m_0$  is increased, more trusses are allowed to have an axial rigidity  $EA = EA_{min} = 10^4 Pa \cdot m^2$ , thus leading to a more flexible structure that can sustain larger displacements but with more design complexity and iteration steps, as shown in Fig. 3.7.

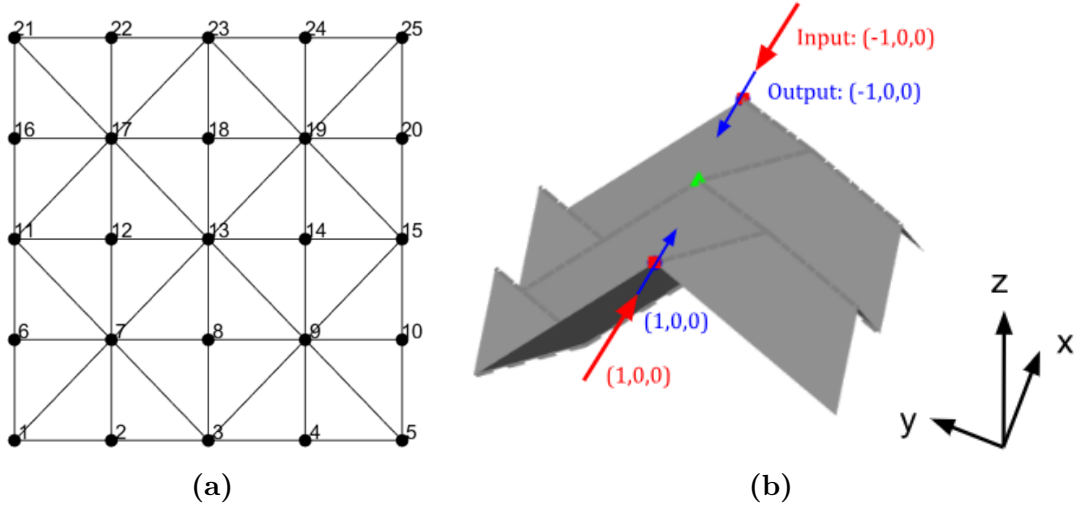
It is also interesting to notice that, since the load condition and  $l_0$  are kept constant during this analysis, the optimized crease pattern is the same for the considered material fractions. However, in some cases (like in the next example) different optimized crease patterns are obtained for the same  $l_0$  increasing  $m_0$  due to the modified behavior of the more flexible structure.



**Figure 3.7:** Objective function over iteration for different  $m_0$  in the zigzag structure ( $l_0 = 0.5$ ).

### 3.5.3 Miura-Ori Fold Pattern

This last example is chosen to explore both the folding and stretching phenomena. The trusses in the starting configuration are displayed in Fig. 3.8a, and the sheet is folded like in Fig. 3.8b to obtain a unit cell of the *Miura-Ori* fold pattern. As previously mentioned in Chapter 1, this configuration, repeated a number of times along the  $x$  and  $y$  direction, has inspired many solar sails designs in the past. This problem has 96 design variables ( $N_f = 40$  relative to  $\alpha$ ,  $N_e = 56$  relative to  $\beta$ ) and the length of the structure is  $L_x = 1.7 m$ , while its width is  $L_y = 1.0 m$ .



**Figure 3.8:** Starting configuration of the Miura-Ori pattern. (a) Reference grid; (b) Load and boundary conditions ( $L_x = 1.0 \text{ m}$ ,  $L_y = 1.0 \text{ m}$ ,  $F = 600 \text{ N}$ ).

In this example, neither folding nor stretching of the folds can be neglected. Tab. 3.3 shows the results obtained from the optimizer in Reference [68]. Under a fold line fraction ( $l_0$ ) of around 0.30, the number of active fold lines allowed is insufficient to obtain convergence. Here, the axial rigidity is kept constant and equal to  $EA = 10^8 \text{ Pa} \cdot \text{m}^2$ . As expected, a higher fold line fraction leads to an optimized crease pattern with more folds and larger displacements (Fig. 3.9).

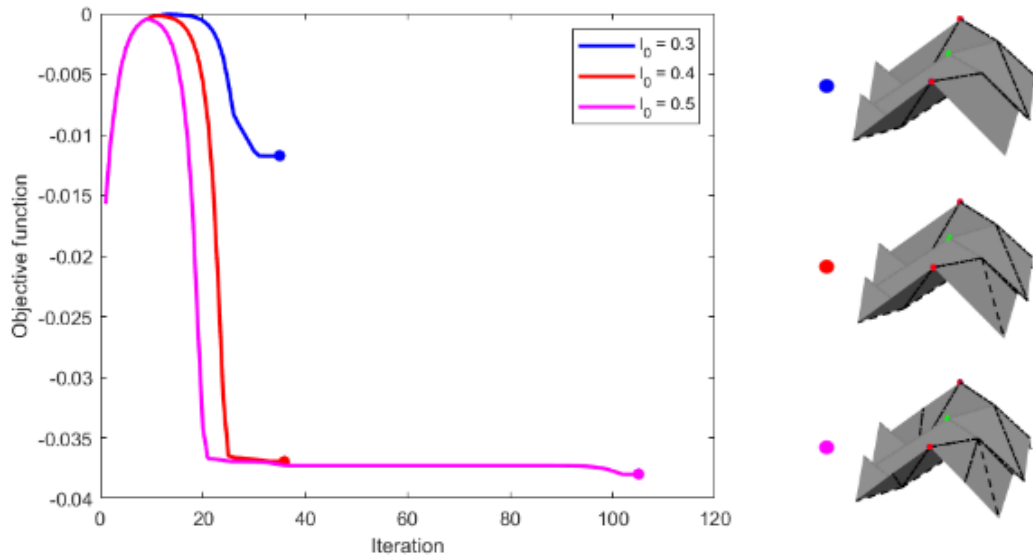
From Tab. 3.4, it is possible to assess the effects of the addition of the second set of design variables over the final configuration and the objective function. For example,  $m_0$  is changed from 0.30 to 0.50, maintaining  $l_0$  constant and equal to 0.50. Under these conditions, if  $m_0$  is increased more trusses are allowed to have a minimum axial rigidity. Therefore, the structure is more flexible and can sustain larger displacements (Fig. 3.10), which indicates that in this case the topology optimization carried out with the optimization method in Section 3.3 and 3.4 leads to a more significant actuation with respect to the one in Reference [11].

Lastly, as mentioned in the previous example, even if the load condition and  $l_0$  are kept constant during this analysis, due to the complexity of this configuration a more flexible structure implies that the origami needs to be folded along different fold lines, leading to new optimized crease patterns than Tab. 3.3.



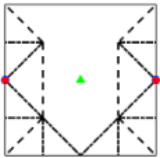
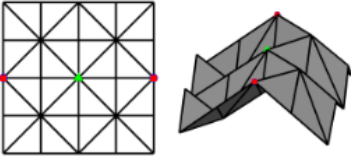
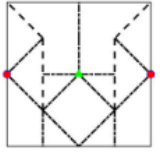
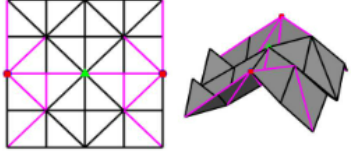
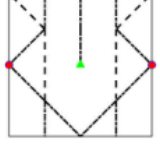
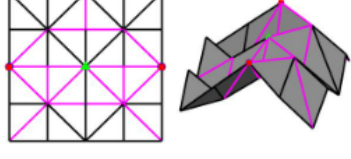
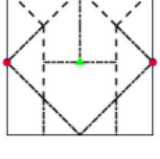
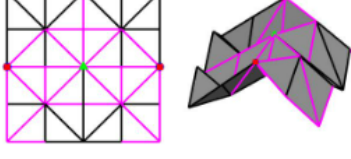
**Table 3.3:** Final configurations of the Miura-Ori pattern (design variable:  $\alpha$ ). Dashed lines in Optimized Crease Pattern: active folds with  $G = G_{soft} = 10^2 \text{ Pam}^2$ .

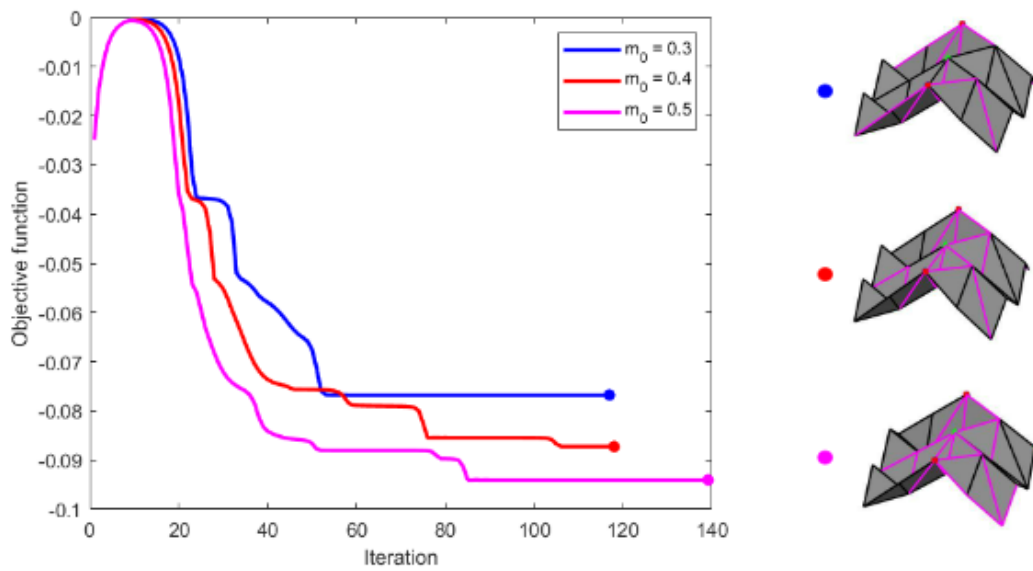
$l_0$ [-]	Optimized Crease Pattern	$f$ [mm]
0.30		- 11.8
0.40		- 37.0
0.50		- 38.0



**Figure 3.9:** Objective function over iteration for different  $l_0$  in the Miura-Ori pattern.

**Table 3.4:** Final configurations of the Miura-Ori pattern. Dashed lines in Optimized Crease Pattern: active folds with  $G = G_{soft} = 10^2 Pa \cdot m^2$ . Magenta and black lines in Axial Rigidity Distribution:  $EA = EA_{min} = 10^4 Pa \cdot m^2$  and  $EA = EA_0 = 10^8 Pa \cdot m^2$ .

$l_0$ [-]	$m_0$ [-]	Optimized Crease Pattern	Axial Rigidity distribution	$f$ [mm]
<b>1 set of design variables (<math>a</math>)</b>				
0.50	0			-38.00
<b>2 sets of design variables (<math>a, \beta</math>)</b>				
0.50	0.30			-76.80
0.50	0.40			-87.20
0.50	0.50			-94.00



**Figure 3.10:** Objective function over iteration for different  $m_0$  in the Miura-Ori pattern ( $l_0 = 0.5$ ).

## Chapter 4

# Topology Optimization Based on Nonlinear Analysis

Building on top of the topology optimization through linear analysis described in Chapter 3, an optimization method based on nonlinear analysis is described in this Chapter to study large displacements and large rotations in origami structures.

### 4.1 Nonlinear truss model

In large displacement origami, the structure does not follow the traditional linear mechanics and a different optimization method than the one described in Chapter 3 is needed.

As extensively discussed by Kim [72], there are four main categories of *mechanical nonlinearities*:

1. *Geometric nonlinearities*: take place when the deformation of the structure is so large that it causes significant changes in the shape, therefore the relationship between strain and displacement is no longer linear;
2. *Material nonlinearities*: take place when the material properties of a structure change during the deformation, therefore the relationship between stress and strain (i.e. the constitutive relationship) of the material is no longer linear;
3. *Kinematic nonlinearities*: take place when the boundary conditions change during the deformation process, for example during contacts;
4. *Force nonlinearities*: take place when the load changes direction according to the movement of the structure during the deformation process (follower forces).

The most common algorithm to deal with nonlinearities is the *Newton-Raphson method* [73], usually used with the introduction of a step-force control to guarantee better stability. This method converges if and only if the first-order derivative is known and there are no points of inflection, local maxima, or minima around the starting point or the root.

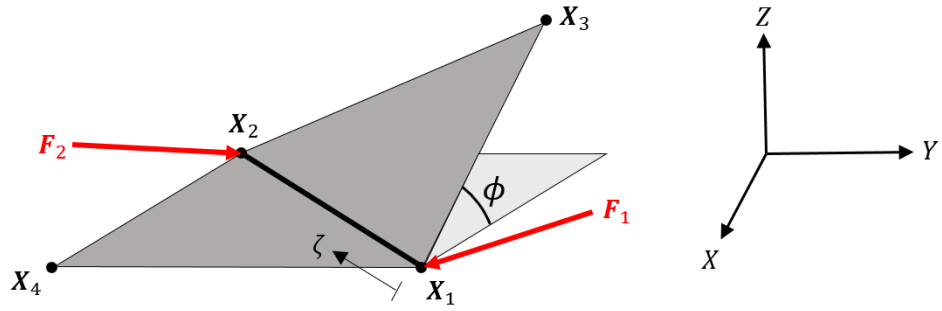
Gillman et al. [15] successfully introduced a modified nonlinear truss model to consider large displacements and large rotations in origami, while optimizing efficiency and accuracy to face the increased difficulty given by the nonlinearity of the problem.

This model is based on the positional finite element truss by Greco et al. [16], which presented a geometric nonlinear formulation for static problems involving space trusses, based on the Finite Element Method (FEM), that uses nodal positions rather than nodal displacements to describe the problem. The model was modified including a torsional spring around the truss element, so that the fold stiffness between two adjacent facets can be considered.

Liu and Paulino [13] also introduces a torsional spring in their analysis, however using nodal displacements rather than nodal positions to describe the problem. Nevertheless, the positional formulation is simpler and more advantageous for the assignment of position-based constraints and a more direct representation of the fold angles.

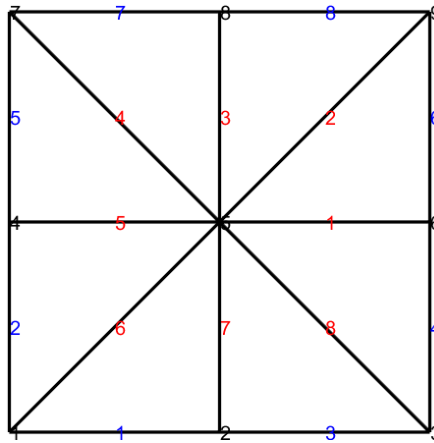
A scheme of the origami element of the modified nonlinear truss model is shown in Fig. 4.1, where:

- The fold angle  $\phi$  is the dihedral angle that defines the inclination of a facet with respect to its original position;
- $\mathbf{X}_l = (X_l, Y_l, Z_l)$  (with  $l = 1, \dots, 4$ ) is the global position of the  $l$ -th node.  $X_{tri} = \{\mathbf{X}_1, \mathbf{X}_2, \mathbf{X}_3, \mathbf{X}_4\}$  is the set of global coordinates of the local nodes required to define the fold angle  $\phi$ ;
- The black line that connects nodes 1 and 2 is the fold line, a truss element that contains an axial strain term with axial rigidity  $EA$  and a bending energy term with fold stiffness  $G$ ;
- $\mathbf{F}_i = (F_{X_i}, F_{Y_i}, F_{Z_i})$  is the nodal force applied in one of the nodes of the fold line;
- $\zeta$  is the nondimensional integration length dimension along the axial direction of the truss.



**Figure 4.1:** Scheme of the origami element in the modified nonlinear truss model.

The ground structure, i.e. the reference grid of a generic origami with the described nonlinear truss model is shown in Fig. 4.2, where the black lines represent the trusses, enumerated in blue at the boundaries and in red in the interior (fold lines), while the nodes are enumerated in black.



**Figure 4.2:** Reference grid of the nonlinear truss model.

Lastly, the thickness of the origami structure is not considered in the described nonlinear model, and the trusses are one-dimensional. However, thickness has been studied Zirbel et al. [45].

## 4.2 Principle of Minimum Energy

To study the nonlinear problem, the principle of minimum energy associated with the single element in Fig. 4.1 is presented, and it can be extended to a generic origami truss structure through assembly.

The total energy ( $\Pi$ ) is defined as

$$\Pi = U_t - P, \quad (4.1)$$

where  $U_t$  is the potential energy and  $P$  is the external energy.

The potential energy is

$$U_t = t_0 \int_0^1 \left[ \frac{EA}{2} \varepsilon(\mathbf{X}_1, \mathbf{X}_2)^2 + \frac{G}{2} \tilde{\phi}(\mathbf{X}_1, \mathbf{X}_2, \mathbf{X}_3, \mathbf{X}_4)^2 \right] d\zeta = t_0 \int_0^1 [u_t + u_h] d\zeta, \quad (4.2)$$

where  $u_t$  and  $u_h$  are the energies per length of the truss and hinge, respectively. The axial strain  $\varepsilon$  quantifies the axial deformation of the truss element

$$\varepsilon = \frac{1}{t_0} (|\mathbf{X}_2 - \mathbf{X}_1| - t_0) = \frac{1}{t_0} (\sqrt{(X_2 - X_1)^2 + (Y_2 - Y_1)^2 + (Z_2 - Z_1)^2} - t_0), \quad (4.3)$$

while  $\tilde{\phi}$  quantifies the torsional deformation of the spring

$$\tilde{\phi}(\mathbf{X}_1, \mathbf{X}_2, \mathbf{X}_3, \mathbf{X}_4) = \phi(\mathbf{X}_1, \mathbf{X}_2, \mathbf{X}_3, \mathbf{X}_4) - \phi_0, \quad (4.4)$$

where  $t_0$  and  $\phi_0$  are the length and the angle of the structure in their undeformed state, while  $\phi$  is a nonlinear function that represents the current fold angle.

A linear constitutive model is assumed in Eq.s (4.3) and (4.4), however  $\varepsilon$  and  $\tilde{\phi}$  depend on the global position of the nodes, hence they are subjected to the geometric nonlinearities of the motion. Therefore, a penalty function is introduced to avoid singularities and to enforce that the two facets are kept in contact.

$$p(\phi) = C((\phi/\pi)^B) + 1, \quad (4.5)$$

with  $B$  and  $C$  constants that influence the fold stiffness of the structure. Introducing the penalty function, the potential energy becomes

$$U_t^p = t_0 \int_0^1 [u_t + p(\phi)u_h] d\zeta, \quad (4.6)$$

hence, the total energy

$$\Pi = U_t^p - P. \quad (4.7)$$

The external energy is

$$\begin{aligned}
 P = & F_{X_1}(X_1 - X_1^0) + F_{X_2}(X_2 - X_2^0) \\
 & + F_{Y_1}(Y_1 - Y_1^0) + F_{Y_2}(Y_2 - Y_2^0) , \\
 & + F_{Z_1}(Z_1 - Z_1^0) + F_{Z_2}(Z_2 - Z_2^0)
 \end{aligned} \tag{4.8}$$

where for example  $X_1^0$  is the node location along the  $X$  axis of node 1 in the undeformed state. The forces are therefore multiplied by the displacements of the nodes:  $\mathbf{u}_1 = \mathbf{X}_1 - \mathbf{X}_1^0$  and  $\mathbf{u}_2 = \mathbf{X}_2 - \mathbf{X}_2^0$ .

Lastly, the principle of minimum energy states that the equilibrium state of the structure is reached when the following equation is satisfied

$$\frac{\partial \Pi}{\partial X_l} = t_0 \int_0^1 \left[ \frac{EA}{2} \frac{d\varepsilon}{dX_l} + \left( Gp(\phi)\tilde{\phi} + G\frac{\tilde{\phi}^2}{2} \frac{\partial p(\phi)}{\partial \phi} \right) \frac{\partial \phi}{\partial X_l} \right] d\zeta - F_{X_l} = q_l - F_{X_l} = 0. \tag{4.9}$$

### 4.3 Linearization of the nonlinear problem

The principle of minimum energy introduces a system of nonlinear equations. To numerically solve them, the Newton-Raphson method is applied. Linearizing Eq. (4.9) through a Taylor's series expansion the residual  $R_l(X_{tri})$  is obtained

$$\begin{aligned}
 R_l(X_{tri}) &= \frac{\partial \Pi}{\partial X_l} = q_l(X_{tri}) - F_l = 0; \\
 R_l(X_{tri}) &\approx R_l(X_{tri}^0) + \nabla R_l(X_{tri}^0) \Delta X_{tri} = 0,
 \end{aligned} \tag{4.10}$$

where the term  $\nabla R_l(X_{tri}^0)$  is the tangent stiffness

$$\begin{aligned}
 K_{lm} = \nabla R_l(X_{tri}^0) &= t_0 \int_0^1 \left[ \frac{EA}{2} \frac{d^2\varepsilon}{dX_l dX_m} + Gp(\phi) \left( \frac{\partial \phi}{\partial X_m} \frac{\partial \phi}{\partial X_l} + \tilde{\phi} \frac{\partial^2 \phi}{\partial X_m \partial X_l} \right) \right. \\
 &\quad \left. + G \frac{\partial^2 p(\phi) \tilde{\phi}^2}{\partial \phi^2} \left( \frac{\partial \phi}{\partial X_m} \frac{\partial \phi}{\partial X_l} + \tilde{\phi} \frac{\partial^2 \phi}{\partial X_m \partial X_l} \right) + 2G\tilde{\phi} \frac{\partial p(\phi)}{\partial \phi} \left( \frac{\partial \phi}{\partial X_m} \frac{\partial \phi}{\partial X_l} \right) \right] d\zeta.
 \end{aligned} \tag{4.11}$$

where the indices  $l$  and  $m$  iterate through all the components of  $\mathbf{X}_{tri}$ . Therefore, from Eq. (4.10), the following equation is obtained

$$K_{lm} \Delta X_{tri} = -R_l(X_{tri}^0), \tag{4.12}$$

that is solved iteratively until the equilibrium is reached (within a prescribed tolerance).



Furthermore, at each iteration, the residual  $R_l$  and the tangent stiffness  $K_{lm}$  are computed both for the trusses at the interior (fold lines) and for the trusses at the boundary, since those at the boundary do not fold, hence their bending energy term (the fold stiffness  $G$ ) is equal to zero. They are later summed like in Eq.s (4.13) and (4.14) to obtain the global residual and the global tangent stiffness

$$R_l = R_l^F + R_l^B; \quad (4.13)$$

$$K_{lm} = K_{lm}^F + K_{lm}^B. \quad (4.14)$$

Additionally, in their space applications, origami structures are frequently used with tessellation patterns, where a crease pattern is repeated along various directions. A procedure to adjust the described method to take into account these configurations is given in Reference [15] and summarized in Appendix B.

Lastly, increment loads are considered in this Chapter in order to follow the complex nonlinear loading behavior of origami structures subjected to large displacements. During every iterative cycle, the load is increased until a set number of iterations is reached, taking into account that the maximum load magnitude applied should be of the same order as the fold stiffness, in order to allow the structure to be folded while suppressing too large deformations of truss members, leading to more realistic designs.

However, to explore more complex behaviors of origami structures with intricate nonlinear profiles, using a monotonically increasing force field is not enough. In these cases, an arc-length method as described in Reference [15] and summarized in Appendix C should be applied, where a scalar Lagrange multiplier is introduced to scale the applied force vector.

## 4.4 Optimization Framework

Similarly to what Fuchi et al. [11] did with linear analysis, Gillman et al. [25] proposed a design method to apply nonlinear analysis to origami structures using topology optimization considering the fold stiffness of every truss element in the structure (modeled through the torsional spring stiffness  $G$ ) as a design variable. Through this method, the optimized crease pattern is obtained, revealing only the active fold lines required to obtain the greatest actuation after the analysis.

Furthermore, even if the inactive fold lines are not shown, they indicate that the two adjacent facets are considered as one, therefore, if their angle  $\phi$  is not zero, it is possible to observe a coarse representation of *facet bending*. The fold stiffness is displayed in Eq. (3.6).

Following the linear method described in Chapter 3, in this Chapter, the optimization method introduced by Gillman et al. [25] is improved including also the axial rigidity  $EA$  as a design variable through the SIMP method, considering Eq. (3.8). Nevertheless, due to the nonlinearity of the problems, this method does not provide only black-and-white results, leading also to some in-between values.

The *optimization problem* is the following:

Find  $\mathbf{x} = \alpha_1, \dots, \alpha_{N_f}, \beta_1, \dots, \beta_{N_e}$  that

Minimize  $f = -\mathbf{c}^T \mathbf{u}$

Subject to

$$g_1 = v_{0,1} - \frac{1}{N_f} \sum_{i=1}^{N_f} x_i \leq 0; \quad g_2 = v_{0,2} - \frac{1}{N_e} \sum_{i=N_f+1}^{N_f+N_e} x_i \leq 0; \quad (4.15)$$

$$0 \leq x_i \leq 1; \quad \forall i = 1, \dots, N_f + N_e;$$

$$R_l(\mathbf{X}) = 0; \quad u_l = X_l - X_l^0; \quad l = 1, \dots, 3N_n.$$

The difference with the linear optimization in the previous Chapter lies in the governing equation of the system. The final constraint is the linearization of the residual to solve the system of nonlinear equations introduced in Eq. (4.9), where the distance between the deformed and undeformed location of the  $l$ -th node is the displacement of that node. Lastly,  $N_n$  is the number of nodes, hence  $3N_n$  are the degrees of freedom of the structure. Two gradient-based optimization algorithms are used to perform the analyses: the Method of Moving Asymptotes (MMA) and the Sequential Quadratic Programming (SQP).

An overview of the algorithm is shown in Fig. 4.3.

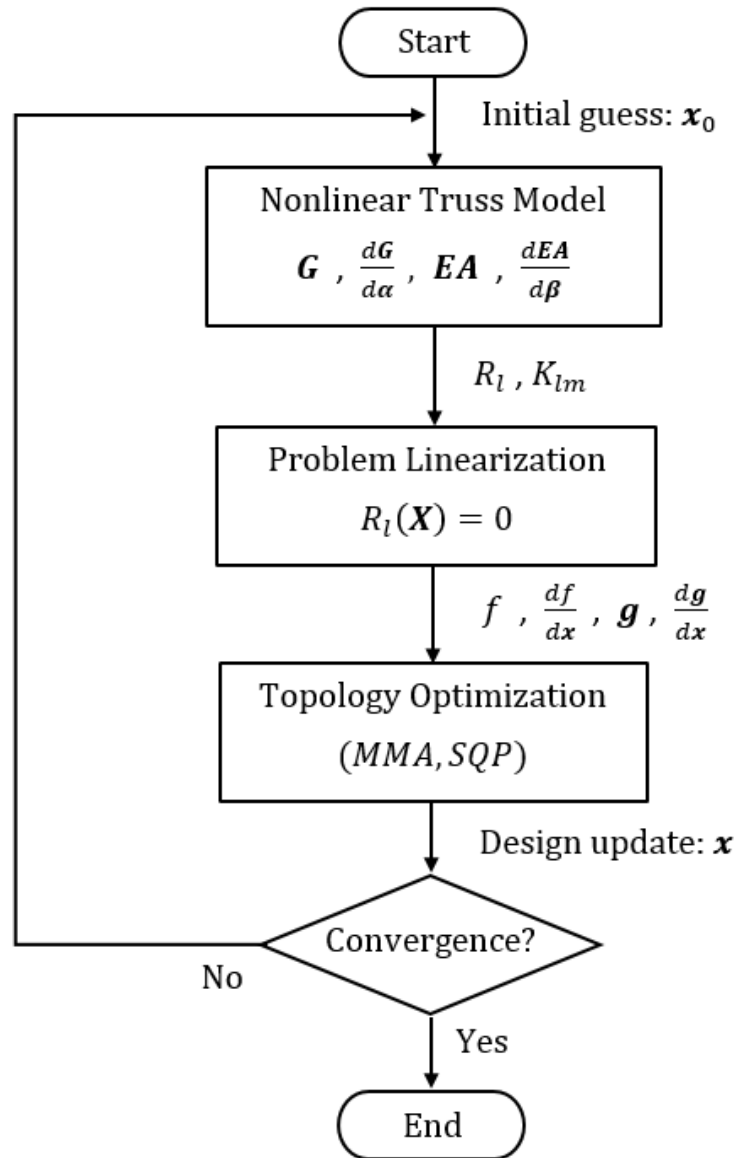


Figure 4.3: Flow chart of the linear optimization process.

#### 4.4.1 Sensitivity analysis

To carry out the sensitivity analysis, the constraint functions are evaluated as in Section 3.4.1. Moreover, the derivative of the objective function with respect to the design variables is obtained as follows:

$$\frac{df}{dx_i} = \frac{\partial f}{\partial x_i} + \frac{\partial f}{\partial X_m} \frac{dX_m}{dx_i}, \quad (4.16)$$

where  $\partial f/\partial x_i = 0$  since  $f$  does not explicitly depend on  $x_i$ ,  $\partial f/\partial X_m$  is found by directly differentiating the objective function  $f$  and  $dX_m/dx_i$  is determined solving the following system of equations:

$$K_{lm} \frac{dX_m}{dx_i} = -\frac{\partial R_l}{\partial x_i}. \quad (4.17)$$

The vector  $\partial R_l/\partial x_i \in [3N_n, N_f + N_e]$  has the first  $N_f$  columns equal to

$$\frac{\partial R_l}{\partial \alpha_k} = t_0 \int_0^1 \left[ \frac{\partial G_k}{\partial \alpha_k} p(\phi) \tilde{\phi} + \frac{\partial G_k}{\partial \alpha_k} \frac{\tilde{\phi}^2}{2} \frac{\partial p(\phi)}{\partial \phi} \right] \frac{\partial \phi}{\partial X_l} d\zeta, \quad (4.18)$$

where

$$\frac{\partial G_k}{\partial \alpha_k} = (a_1 - a_0) 10^{a_0 + \alpha_k(a_1 - a_0)} \log(10), \quad (4.19)$$

while the remaining  $N_e$  columns are equal to

$$\frac{\partial R_l}{\partial \beta_j} = t_0 \int_0^1 \frac{1}{2} \frac{\partial EA_j}{\partial \beta_j} \frac{d\varepsilon}{dX_l} d\zeta, \quad (4.20)$$

where

$$\frac{\partial EA_j}{\partial \beta_j} = p\beta_j^{(p-1)}(EA_0 - EA_{min}). \quad (4.21)$$

The whole process, schematized in Fig. 4.3, is described here:

1. At the start of each iteration,  $\mathbf{G}$ ,  $\mathbf{EA}$  and their gradients are computed for each fold line and truss member respectively. The residual  $R_l$  and the tangent stiffness  $K_{lm}$  are evaluated from Eq.s (4.10) and (4.11), along with the gradient of the residual  $\partial R_l/\partial x_i$  from Eq.s (4.18) and (4.20);
2. Through Eq. (4.14), the nonlinear problem is linearized with the purpose of finding the displacement field  $\Delta X_{tri}$ , while its gradient is obtained from Eq. (4.17);

3. The objective function and its gradient from Eq.s (4.15) and (4.16) are computed, as well as the constraint functions and their gradients from Eq.s (3.10) and (3.11);
4. The gradient-based topology optimization is carried out both with the MMA and the SQP method, in order to obtain the new set of design variables  $\boldsymbol{x}$  for the next iteration;
5. This iterative process is repeated until the relative error between the objective functions at the current and at the previous iteration is lower than a set tolerance. Therefore, the equilibrium state of the structure is reached, and the axial rigidity distribution of the trusses along with the origami crease pattern that maximizes the displacement at set locations are obtained.

Furthermore, the described method can be expanded including modal analysis to distinguish and follow multiple bifurcation branches, as described in Reference [15] and summarized in Appendix D.

Lastly, topology optimization can be functional to the discovery of origami patterns that manifest a negative Poisson's ratio, i.e. *auxetic origami*, modifying the described method as illustrated in Reference [26] and summarized in Appendix E.

## 4.5 Numerical Examples

To assess the capability of the nonlinear truss model with the introduction of axial rigidity as a design variable, two different starting configurations of well-known origami actuator designs ("Chomper" and "Square Twist" patterns) are studied.

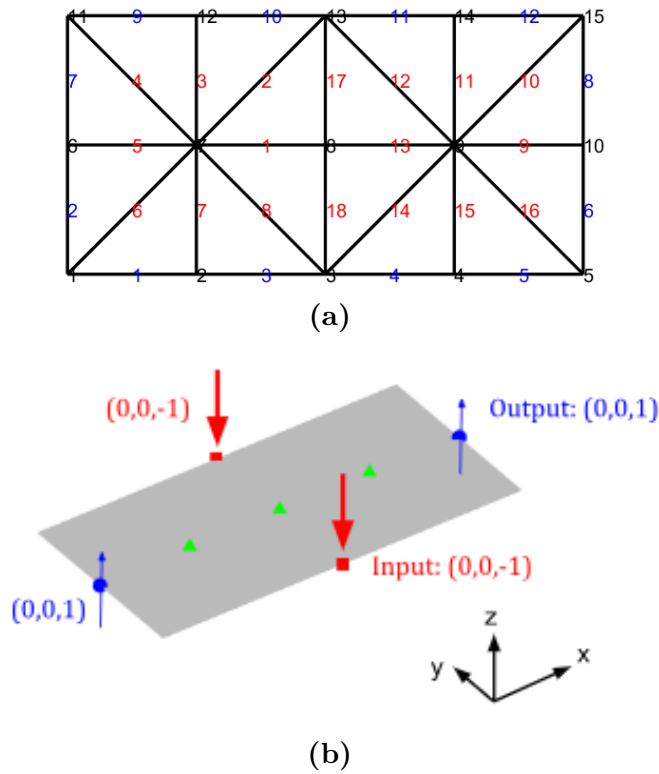
The optimization is evaluated through comparisons with the works of Gillman et al. [24, 25], where only one set of design variables is considered. Each case is studied first using the Origami Topology Optimization with Nonlinear Truss Model (OTON) in Reference [74] that uses only the fold stiffness exponent ( $\boldsymbol{\alpha}$ ) as design variable and the constraint on the number of active fold lines allowed ( $l_0$ ), then with a modified OTON, which uses the method described in this Chapter, that also considers the axial rigidity density ( $\boldsymbol{\beta}$ ) as design variable and the constraint on the number of trusses that are allowed to have a minimum axial rigidity ( $m_0$ ).

Furthermore, the dashed lines in the optimized crease pattern indicate the active folds that remain after the optimization (soft folds with  $G = G_{soft}$ ). Lastly, the color of the trusses in the axial rigidity distribution is given in a scale of gray, where white and black indicate an axial rigidity  $EA = EA_{min}$  or  $EA = EA_0$  respectively.

However, a "projected" axial rigidity distribution is presented, where the black and magenta lines indicate that the truss members have an axial rigidity with a relative error within 10% close to  $EA = EA_0$  or  $EA = EA_{min}$  respectively, while greater than 10% for the gray lines.

### 4.5.1 Chomper fold pattern

The first example considers a simple *Chomper* fold pattern. The problem has 48 design variables ( $N_f = 18$  relative to  $\alpha$ ,  $N_e = 30$  relative to  $\beta$ ). Fig. 4.4a shows the reference grid of the structure, while Fig. 4.4b shows the three-dimensional representation of the starting configuration with the load and boundary conditions, where the central green triangle is a fixed node, while the other two are allowed to move along  $x$ . Lastly, the length of the structure is  $L_x = 0.2 m$ , while its width is  $L_y = 0.1 m$ .



**Figure 4.4:** Starting configuration of the Chomper pattern. (a) Reference grid; (b) Load and boundary conditions ( $L_x = 0.2 m$ ,  $L_y = 0.2 m$ ,  $F = 10\,000 N$ ).

In this example, the following parameters are considered:

- $EA = 10^7 Pa \cdot m^2$  for one set of design variables;
- $EA_{min} = 10^5 Pa \cdot m^2$  and  $EA_0 = 10^7 Pa \cdot m^2$  for two sets of design variables;
- $l_0 = 0.44$  (equivalent to 6 active fold lines allowed);
- $G_{stiff}/G_{soft} = 10^3$ .

To demonstrate the effect that material properties have on the optimal actuation motion, two sets of material properties are considered, varying  $G_{soft}$  and  $G_{stiff}$ :

1. Case 1:  $EA/G_{stiff} = 10^1$  (or  $EA_0/G_{stiff} = 10^1$  for two sets of design variables);
2. Case 2:  $EA/G_{stiff} = 10^3$  (or  $EA_0/G_{stiff} = 10^3$  for two sets of design variables).

For each case, different values of the constraint  $m_0$  are used to study the effect of the addition of the second set of design variables.


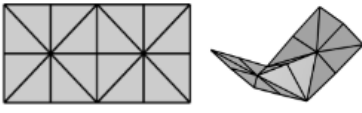

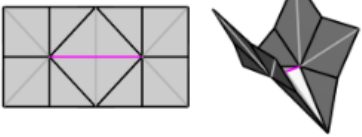

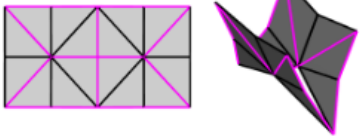

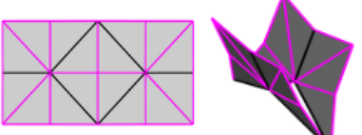
### Case 1

Tab. 4.1 shows the values of the objective functions and the final configurations of the Chomper problem for Case 1 obtained with the MMA method.

All the configurations in Tab. 4.1 discover the Chomper fold pattern. Like in the linear case, if  $m_0$  is increased more trusses are allowed to have a minimum axial rigidity, thus leading to a more flexible structure that can sustain larger displacements but with more iteration steps, as shown in Fig. 4.5.

The improvement of the described nonlinear method with respect to the linear method in Chapter 3 is evident, since greater displacements than within a 10% range of the length of the structure can now be obtained. Therefore, even though the load and boundary conditions in Fig. 4.4b penalize the stretching of the trusses in the small displacement analysis (emphasizing only the effect of the folding of the sheet), for the large displacements in the nonlinear analysis stretching becomes relevant and the effect of increasing  $m_0$  can now be assessed.

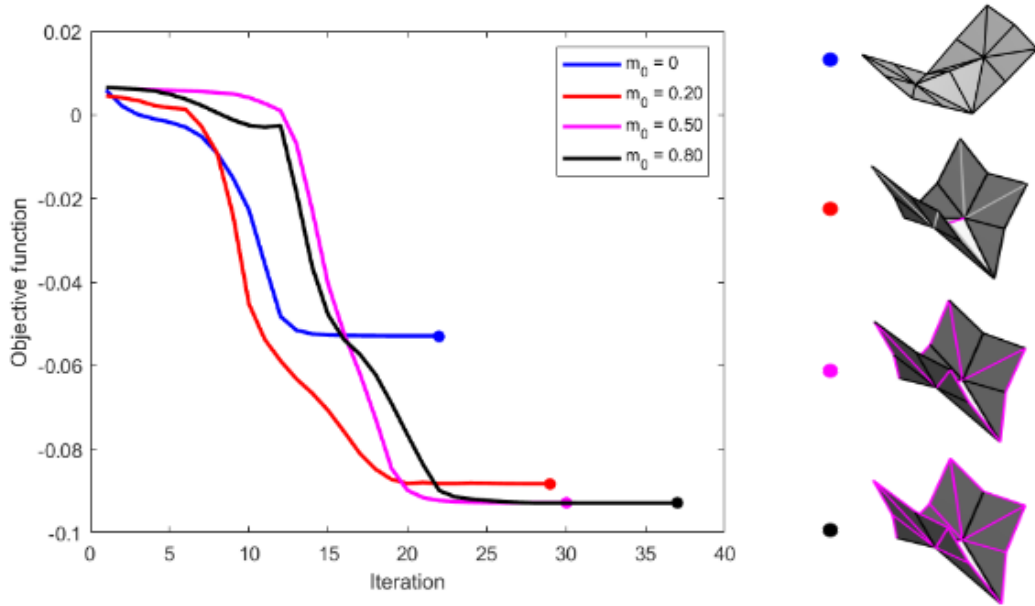
**Table 4.1:** Final configurations of the Chomper pattern, Case 1. Dashed lines in Optimized Crease Pattern: active folds with  $G = G_{soft} = 10^3 Pa \cdot m^2$ . Magenta and black lines in Projected Axial Rigidity Distribution:  $EA = EA_{min} = 10^5 Pa \cdot m^2$  and  $EA = EA_0 = 10^7 Pa \cdot m^2$ .

$l_0$ [-]	$m_0$ [-]	Optimized Crease Pattern	Projected Axial Rigidity distribution	$f$ [mm]
<b>1 set of design variables (<math>\alpha</math>)</b>				
0.44	0			- 52.92
<b>2 sets of design variables (<math>\alpha, \beta</math>)</b>				
0.44	0.20			- 88.30
0.44	0.50			- 92.84
0.44	0.80			- 92.92

The small ratio considered in Case 1 between the axial rigidity of the truss element and a stiff fold ( $EA/G_{stiff} = 10^1$ ) favors facet stretching over facet bending since a greater fold stiffness  $G$  penalizes the bending of the structure. Therefore, continuous regions of the structure with  $G_{stiff}$  (area in sheet with no dashed lines) do not exhibit bending as described in the first part of Section 4.4, and the structure appears to be slightly stretched along some trusses while compressed along others.

It must be noted that, for  $l_0 = 0.44$ , with one set of design variables (hence with the formulation in Reference [25]) the value of the objective function is  $f = -52.92 mm$ , while with two sets of design variables is  $f = -92.92 mm$  (for  $m_0 = 0.80$ ), thus with the topology optimization carried out with the method in Section 4.4 a greater actuation than the one in Reference [25] is obtained.





**Figure 4.5:** Case 1, objective function over iteration for different  $m_0$  ( $l_0 = 0.44$ ).

It is also interesting to notice that, since the load condition and  $l_0$  are kept constant during this analysis, the optimized crease pattern is the same for the considered material fractions.

Lastly, soft fold lines are not discovered between the fixed nodes since the facets that connect the input nodes to the fixed nodes form two symmetric moment arms that lead to the same motion, regardless of the fold stiffnesses of these elements. However, due to the large angle between these two faces, the soft fold lines are added in post-optimization.

## Case 2

Tab. 4.2 shows the values of the objective functions and the final configurations of the Chomper problem for Case 2 obtained with the MMA method.

The ratio considered in Case 2 between the axial rigidity of the trusses and a stiff fold ( $EA/G_{stiff} = 10^3$ ) is larger than the one considered in Case 1, hence facet bending is favored over facet stretching. However, the gradient-based optimization using one set of design variables fails to discover an origami configuration that leads to positive vertical actuation in the output nodes.

**Table 4.2:** Final configurations of the Chomper pattern, Case 2. Dashed lines in Optimized Crease Pattern: active folds with  $G = G_{soft} = 10^1 Pa \cdot m^2$ . Magenta and black lines in Projected Axial Rigidity Distribution:  $EA = EA_{min} = 10^5 Pa \cdot m^2$  and  $EA = EA_0 = 10^7 Pa \cdot m^2$ .


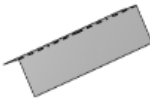
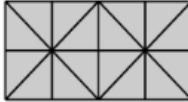
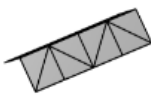
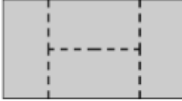

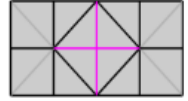
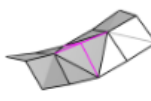
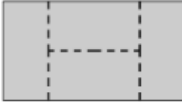

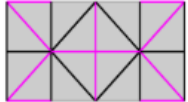
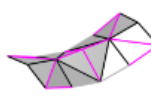
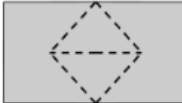
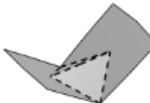


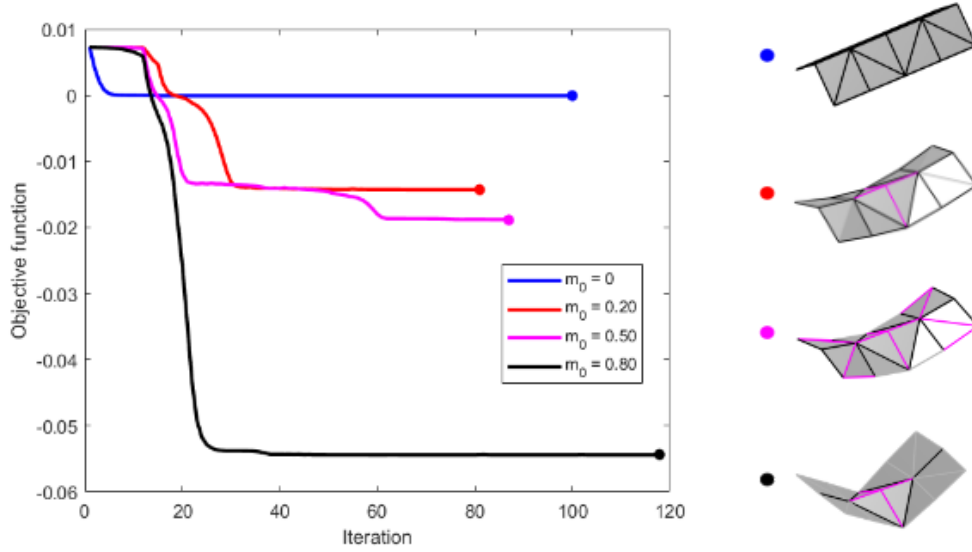
$l_0$ [-]	$m_0$ [-]	Optimized Crease Pattern	Projected Axial Rigidity distribution	$f$ [mm]
<b>1 set of design variables (<math>a</math>)</b>				
0.44	0	 	 	- 9.0e-5
<b>2 sets of design variables (<math>a, \beta</math>)</b>				
0.44	0.20	 	 	- 14.23
0.44	0.50	 	 	- 18.79
0.44	0.80	 	 	- 54.42

Fig. 4.6 shows that in this case the problem does not converge and the iterative process is stopped at 100 iterations, resulting in an objective function value close to zero.

Nevertheless, as shown in Tab. 4.2, using two sets of design variables it is possible to observe a vertical actuation of the output nodes and the bending of the structure (change in angle between some facets with no soft fold lines between them). Furthermore, if  $m_0$  is increased, more trusses are allowed to have a minimum axial rigidity, thus the final configuration tends to lean toward that of Case 1. Therefore, for  $m_0 = 0.80$ , the Chomper fold pattern is discovered, obtaining a larger actuation than with lower  $m_0$  values, but for the cost of more iteration steps, as shown in Fig. 4.6. Lastly, since the ratio  $EA/G_{stiff}$  decreases if  $m_0$  increases, facet stretching tends to be more favored than facet bending. Therefore, for  $m_0 = 0.80$  no bending can be observed in the structure.



**Figure 4.6:** Case 2, objective function over iteration for different  $m_0$  ( $l_0 = 0.44$ ).

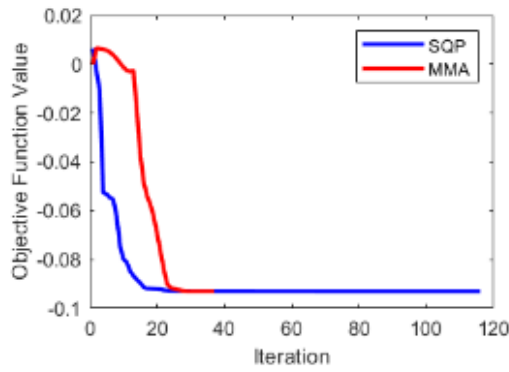
As mentioned in this Section, the SIMP method does not lead to a black-and-white solution for the problem, hence the axial rigidity  $EA$  of the trusses takes on values different from  $EA_{min}$  and  $EA_0$ . Therefore, Tab. 4.3 shows the real axial rigidity distribution of the structure, where the color of the trusses in the axial rigidity distribution is given in a scale of gray, with white and black indicating an axial rigidity  $EA = EA_{min}$  or  $EA = EA_0$  respectively. Moreover, as expected, it can be observed that the color of the trusses becomes slightly lighter if  $m_0$  is increased.

Lastly, the analysis is repeated with the SQP method, obtaining the same final configurations. In Fig. 4.7, both optimization methods converge to the same results, but the SQP method needs more iterations to converge due to its higher computational cost, as described by Fanni et al. [75].

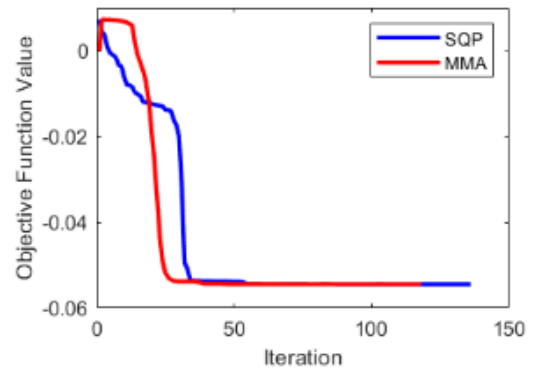
In order to discover the Chomper fold pattern, Gillman et al. [25] implements a Genetic Algorithm (GA) that enables the exploration of the bending phenomenon and obtains vertical actuation with less facet deformation. Although the superior performance of GA for these origami topology optimization problems, the trade-off is in the amount of computational cost required with respect to gradient-based methods, since four orders of magnitude more evaluations of the objective function are required.

**Table 4.3:** Axial rigidity distribution of Case 1 and Case 2 of the Chomper pattern.

$l_0$ [-]	$m_0$ [-]	Axial rigidity distribution		Colorbar
		Case 1	Case 2	
0.44	0.20			
0.44	0.50			
0.44	0.80			



(a)

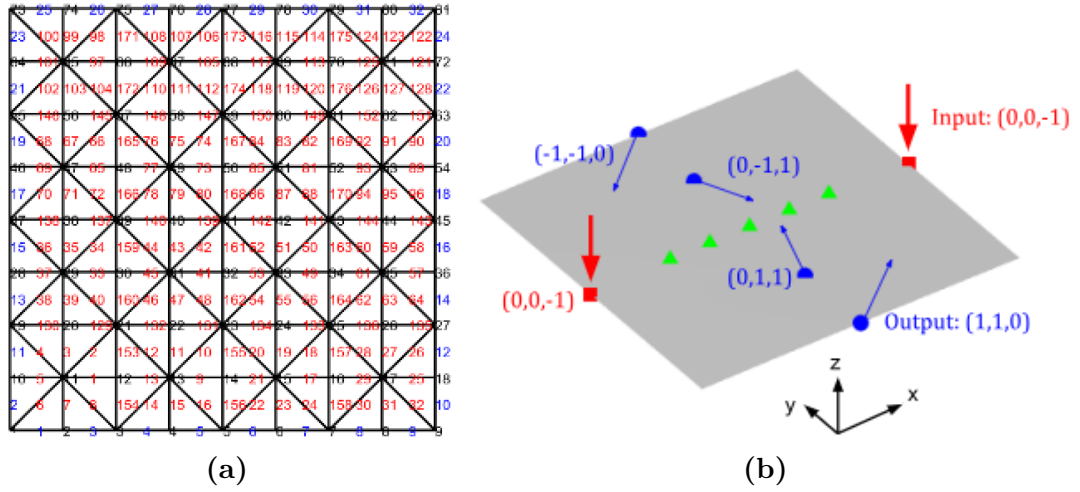


(b)

**Figure 4.7:** Objective function over iteration with SQP and MMA methods of the Chomper pattern, for  $l_0 = 0.44$ ,  $m_0 = 0.80$ . (a) Case 1; (b) Case 2.

### 4.5.2 Square Twist fold pattern

The second example considers the famous *Square Twist* (introduced in Chapter 1) fold pattern, a fold that has been studied by scientists, mathematicians, and origami artists. One of its key aspects is the fact that it cannot be folded rigidly, therefore, if the trusses were made too stiff, it would not be able to fold [76]. The problem has 384 design variables ( $N_f = 176$  relative to  $\alpha$ ,  $N_e = 208$  relative to  $\beta$ ). Fig. 4.8a shows the reference grid of the structure, while Fig. 4.8b shows the three-dimensional representation of the starting configuration with the load and boundary conditions, where the central green triangle is a fixed node, while the other four are allowed to move along  $x$ . Lastly, the length of the structure is  $L_x = 0.4 m$ , while its width is  $L_y = 0.4 m$ .



**Figure 4.8:** Starting configuration of the Square Twist pattern. (a) Reference grid; (b) Load and boundary conditions ( $L_x = 0.4 m$ ,  $L_y = 0.4 m$ ,  $F = 10\,000 N$ ).

The loads and boundary conditions in Fig. 4.8b should result in an inward folding followed by a twisting motion to achieve a flat folded configuration where the facets are parallel and in contact with each other, as shown in Fig. 1.12. In this example, the following parameters are considered:

- $EA = 10^8 Pa \cdot m^2$  for one set of design variables;
- $EA_{min} = 10^6 Pa \cdot m^2$  and  $EA_0 = 10^8 Pa \cdot m^2$  for two sets of design variables;
- $l_0 = 0.20$  (equivalent to 32 active fold lines allowed);
- $m_0 = 0.50$  (equivalent to 104 trusses that are allowed to have axial rigidity  $EA = EA_{min}$ );

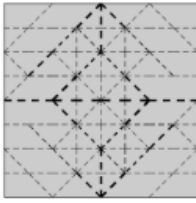
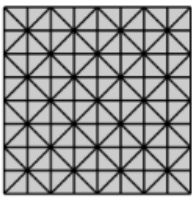
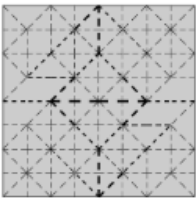
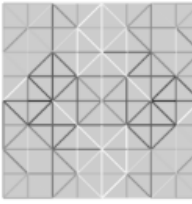
- $EA/G_{stiff} = 10^4$  (or  $EA_0/G_{stiff} = 10^4$  for two sets of design variables);
- $G_{stiff}/G_{soft} = 10^3$ .

The number of design variables is increased with respect to the previous examples, thus the problem is now more complex and the convergence rate of the algorithm is significantly slowed.

Again, the optimization was carried out both with MMA and SQP methods. However, the objective function obtained with MMA oscillates without reaching convergence since it presents multiple subsequent local minima between the lower and upper bounds of the approximated objective function at each iteration. Therefore, only the results obtained with the SQP method are shown as follows.

Tab. 4.4 shows the objective functions and the final configurations obtained for one and two sets of design variables.

**Table 4.4:** Final configuration of the Square Twist pattern. Dashed lines in Optimized Crease Pattern: active folds with  $G = G_{soft} = 10^1 Pa \cdot m^2$ . White and black lines in Axial Rigidity Distribution:  $EA = EA_{min} = 10^6 Pa \cdot m^2$  and  $EA = EA_0 = 10^8 Pa \cdot m^2$ .

$l_o$ [-]	$m_o$ [-]	Optimized Crease Pattern	Axial Rigidity distribution	$f$ [mm]
<b>1 set of design variables (<math>a</math>)</b>				
<b>0.20</b>	<b>0</b>			<b>-468.6</b>
<b>2 sets of design variables (<math>a, \beta</math>)</b>				
<b>0.20</b>	<b>0.50</b>			<b>-489.9</b>

As it can be noted, the two optimized crease patterns do not match like in the previous example, even though the same  $l_0$  is considered. However, under the same conditions, adding the second set of design variables, the new configuration leads to an increase of the 5% in the actuation.

Nevertheless, the optimized crease patterns in Tab. 4.4 fail to satisfy the constraint on the allowable number of active fold lines ( $l_0$ ), since the amount of active fold lines obtained after the optimization process is greater than 20%. This is likely due to numerical instability phenomena during the optimization process related to the nonlinearity of the problem. Therefore, the results need to be projected. The projected final configurations are obtained in the following way:

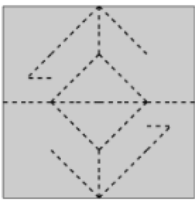
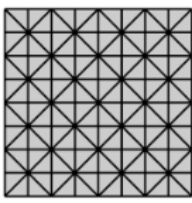
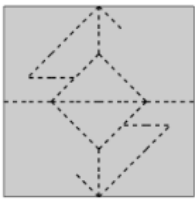
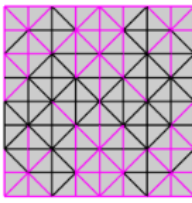
- For one set of design variables: the 32 fold lines (corresponding to  $l_0 = 0.20$ ) with the lowest fold stiffnesses are selected. The values of  $\alpha$  relative to these folds are set equal to 0 to represent the soft active fold lines, while the remaining values are set to 1 (stiff inactive folds);
- For two sets of design variables: the 32 fold lines with the lowest fold stiffnesses and the 104 trusses (corresponding to  $m_0 = 0.50$ ) with the lowest axial rigidities are selected. The values of  $\alpha$  relative to these folds and that of  $\beta$  relative to these trusses are set equal to 0, while the remaining values are set to 1.

The results obtained after the projection are displayed in Tab. 4.5.

The actuation has decreased since a smaller number of active fold lines is registered, i.e. the structure is allowed to fold along fewer fold lines. However, under the same conditions, adding the second set of design variables, the new configuration leads to an increase of about 20% in the actuation.

Nevertheless, the aforementioned flat folded configuration is not achieved using gradient-based optimizations. To obtain a perfectly flat configuration, Gillman et al. [25] introduces a Genetic Algorithm (GA) which utilizes uniform (random) crossover. This procedure is discussed in Appendix A. Overall, even if gradient-based algorithms converge quicker to local minima, GA is proven to show superior performance. Therefore, further analyses are required to study the effect of applying the optimization process described in Section 4.4 to a non-gradient-based method.

**Table 4.5:** Projected final configuration of the Square Twist pattern. Dashed lines in Optimized Crease Pattern: active folds with  $G = G_{soft} = 10^1 Pa \cdot m^2$ . Magenta and black lines in Projected Axial Rigidity Distribution:  $EA = EA_{min} = 10^6 Pa \cdot m^2$  and  $EA = EA_0 = 10^8 Pa \cdot m^2$ .

$l_o$ [-]	$m_o$ [-]	Projected Optimized Crease Pattern	Projected Axial Rigidity distribution	$f$ [mm]
<b>1 set of design variables (<math>a</math>)</b>				
0.20	0			- 280.8
<b>2 sets of design variables (<math>a, \beta</math>)</b>				
0.20	0.50			- 336.3



# Chapter 5

## Conclusions and Future Works

### 5.1 Conclusions

The present thesis introduced an improved design method for origami structures using topology optimization. While previous works considered the fold stiffness related to the bending energy of the structure as the only design variable, penalizing the stretching phenomenon, the novelty introduced in the proposed method is that it takes into account also the axial rigidity, expanding the design space.

A truss model was employed, where origami are constituted by truss elements connected by pin joints. This model proved to be simple yet effective in analyzing origami structures, allowing the use of established structural engineering methods to study their mechanics. Therefore, the objective of the topology optimization method described in this work was to find both the axial rigidity distribution of the trusses and the origami fold pattern that maximizes the displacement at set locations in origami structures, under prescribed forces and boundary conditions.

The capabilities of the method were assessed through study cases of well-known origami fold patterns, assessing the advantage of including axial rigidity as a design variable through comparisons with previous works. Moreover, the optimization process was performed through two gradient-based optimization algorithms to emphasize convergence speed and all the results were obtained from a modified optimizer on MATLAB.

In the first part, topology optimization based on linear analysis was carried out, to study small deformations and small rotations mechanics in origami. Even though origami usually undergo large displacements during their folding motion, this analysis provides a low computational cost method, functional to determine the optimal topology for the initiation of folding. The results demonstrated that, if the axial rigidity is allowed to vary among the trusses of the structure, each truss is allowed to stretch and compress in an optimized way, thus allowing to take into account the stretching phenomenon. Therefore, it is now possible to explore new configurations for origami that could not be explored before. Moreover, if the constraint on the number of trusses that are allowed to have a minimum axial rigidity, i.e.  $m_0$ , is increased, the structure becomes more flexible and can sustain a targeted larger actuation, resulting in a more efficient origami design with respect to the ones obtained in previous works. In any case, if the constraint  $m_0$  is set to zero, axial rigidity is kept constant among the trusses, thus the same results as using only one design variable are obtained.

In the second part, a nonlinear analysis model was presented employing a positional formulation for the truss elements to consider large displacements and large rotations in origami, while optimizing the efficiency and accuracy of the results. From the analyses, the same conclusions of the linear method can be drawn since a larger actuation was achieved by increasing  $m_0$ . Furthermore, the improvement given by the inclusion of the second design variable was further demonstrated, since a targeted origami design was discovered under the conditions for which only one design variable could not succeed. Nevertheless, in the last example, the targeted final configuration was not achieved using gradient-based optimization, motivating further developments to the described method.

Lastly, by allowing axial rigidity to vary among the trusses of the structure, multi-material topology optimization can be achieved, since it is now possible to manufacture the trusses of the origami with different materials (or with different sections) to obtain the optimized configurations.

## 5.2 Future Works

The proposed design method can be expanded to examine more elaborated origami configurations and to analyze more complex origami behavior during their folding motions.

In this study, only gradient-based optimizations were applied. However, this kind of optimization does not always lead to optimal solutions for complex origami

configurations involving highly nonlinear motions. Therefore, for future studies, the application of the described method to non-gradient-based optimizations like the Genetic Algorithm (GA) needs to be assessed.

Also, in their various applications, origami structures usually present repeating patterns. These configurations could be examined considering periodic boundary conditions in the design process.

Moreover, an arc-length method with a scalar Lagrange multiplier needs to be applied to the optimization process. This would allow to explore more complex behaviors of origami structures with intricate nonlinear profiles and to capture origami equilibrium paths beyond limit points.

Additionally, origami usually exhibit equilibrium bifurcations off the flat state. Hence, to explore these phenomena, the described method can be improved including modal analysis.

Lastly, using topology optimization for analyzing origami structures can be functional to the discovery of auxetic metamaterials. Therefore the presented method could lead to the design of new origami patterns that manifest a negative Poisson's ratio.

In any case, more realistic fold patterns should include a fully connected network of fold lines, in contrast to the designs obtained in the presented work. Therefore, further developments in origami topology optimization should include the enforcement of this type of geometric constraint within the optimization algorithm.

# Bibliography

- [1] Edwin A Peraza Hernandez, Darren J Hartl, and Dimitris C Lagoudas. «Active origami: modeling, design, and applications». In: *Cham: Springer* (2018) (cit. on pp. 2, 5–7, 15, 18, 19, 21, 22, 24–26, 28, 30–33).
- [2] Koryo Miura and Michihiro Natori. «2-D array experiment on board a space flyer unit». In: *Space Solar Power Review* 5.4 (1985), pp. 345–356 (cit. on p. 2).
- [3] Robert J Lang. «Origami: Complexity in creases (again)». In: *Engineering and Science* 67.1 (2004), pp. 5–19 (cit. on p. 2).
- [4] Sandra Häuplik, Petra Gruber, Barbara Imhof, Kürsad Özdemir, Rene Wacławicek, and Maria Antoinetta Perino. «Deployable Structures for a Human Lunar Base». In: *57th International Astronautical Congress*, pp. D3–2 (cit. on p. 2).
- [5] Arthur Lebé. «From folds to structures, a review». In: *International journal of space structures* 30.2 (2015), pp. 55–74 (cit. on p. 2).
- [6] Thomas C Hull et al. «Modelling the folding of paper into three dimensions using affine transformations». In: *Linear Algebra and its applications* 348.1-3 (2002), pp. 273–282 (cit. on pp. 2, 36).
- [7] Tomohiro Tachi. «Simulation of rigid origami». In: *Origami* 4.08 (2009), pp. 175–187 (cit. on p. 2).
- [8] Edwin A Peraza Hernandez, Darren J Hartl, and Dimitris C Lagoudas. «Kinematics of origami structures with smooth folds». In: *Journal of Mechanisms and Robotics* 8.6 (2016), p. 061019 (cit. on pp. 2, 15–17, 21, 28).
- [9] Mark Schenk, Simon D Guest, et al. «Origami folding: A structural engineering approach». In: *Origami* 5 (2011), pp. 291–304 (cit. on pp. 3, 97).
- [10] Kazuko Fuchi, Philip R Buskohl, James J Joo, Gregory W Reich, and Richard A Vaia. «Topology optimization for design of origami-based active mechanisms». In: *International Design Engineering Technical Conferences and Computers and Information in Engineering Conference*. Vol. 46377. American Society of Mechanical Engineers. 2014, V05BT08A049 (cit. on p. 3).

- [11] Kazuko Fuchi, Philip R Buskohl, Giorgio Bazzan, Michael F Durstock, Gregory W Reich, Richard A Vaia, and James J Joo. «Origami actuator design and networking through crease topology optimization». In: *Journal of Mechanical Design* 137.9 (2015), p. 091401 (cit. on pp. 3, 13, 35, 38, 39, 44, 48, 50, 59).
- [12] ET Filipov, K Liu, Tomohiro Tachi, Mark Schenk, and Glaucio H Paulino. «Bar and hinge models for scalable analysis of origami». In: *International Journal of Solids and Structures* 124 (2017), pp. 26–45 (cit. on pp. 3, 94).
- [13] Ke Liu and Glaucio H Paulino. «Nonlinear mechanics of non-rigid origami: an efficient computational approach». In: *Proceedings of the Royal Society A: Mathematical, Physical and Engineering Sciences* 473.2206 (2017), p. 20170348 (cit. on pp. 3, 55, 94).
- [14] Evgueni T Filipov, Glaucio H Paulino, and Tomohiro Tachi. «Origami tubes with reconfigurable polygonal cross-sections». In: *Proceedings of the Royal Society A: Mathematical, Physical and Engineering Sciences* 472.2185 (2016), p. 20150607 (cit. on p. 3).
- [15] Andrew Gillman, Kazuko Fuchi, and PR Buskohl. «Truss-based nonlinear mechanical analysis for origami structures exhibiting bifurcation and limit point instabilities». In: *International Journal of Solids and Structures* 147 (2018), pp. 80–93 (cit. on pp. 3, 55, 59, 63, 91, 93, 95–98, 101).
- [16] Marcelo Greco, Francisco Antonio Romero Gesualdo, Wilson Sérgio Venturini, and Humberto Breves Coda. «Nonlinear positional formulation for space truss analysis». In: *Finite elements in analysis and design* 42.12 (2006), pp. 1079–1086 (cit. on pp. 3, 55).
- [17] Eduard Riks. «The application of Newton’s method to the problem of elastic stability». In: (1972) (cit. on pp. 3, 94).
- [18] Eduard Riks. «An incremental approach to the solution of snapping and buckling problems». In: *International journal of solids and structures* 15.7 (1979), pp. 529–551 (cit. on pp. 3, 94).
- [19] Gerald A Wempner. «Discrete approximations related to nonlinear theories of solids». In: *International Journal of Solids and Structures* 7.11 (1971), pp. 1581–1599 (cit. on pp. 3, 94).
- [20] Sofie E Leon, Glaucio H Paulino, Anderson Pereira, Ivan FM Menezes, and Eduardo N Lages. «A unified library of nonlinear solution schemes». In: (2011) (cit. on pp. 3, 94).
- [21] Sofie E Leon, Eduardo N Lages, Catarina N De Araújo, and Glaucio H Paulino. «On the effect of constraint parameters on the generalized displacement control method». In: *Mechanics Research Communications* 56 (2014), pp. 123–129 (cit. on pp. 3, 94, 95).

- [22] Tomohiro Tachi and Thomas C Hull. «Self-foldability of rigid origami». In: *Journal of Mechanisms and Robotics* 9.2 (2017), p. 021008 (cit. on p. 3).
- [23] Christian D Santangelo. «Extreme mechanics: Self-folding origami». In: *Annual Review of Condensed Matter Physics* 8 (2017), pp. 165–183 (cit. on p. 3).
- [24] Andrew Gillman, Kazuko Fuchi, Giorgio Bazzan, Edward J Alyanak, and Philip R Buskohl. «Discovering origami fold patterns with optimal actuation through nonlinear mechanics analysis». In: *International Design Engineering Technical Conferences and Computers and Information in Engineering Conference*. Vol. 58189. American Society of Mechanical Engineers. 2017, V05BT08A052 (cit. on pp. 3, 13, 63, 88).
- [25] Andrew S Gillman, Kazuko Fuchi, and Philip R Buskohl. «Discovering sequenced origami folding through nonlinear mechanics and topology optimization». In: *Journal of Mechanical Design* 141.4 (2019), p. 041401 (cit. on pp. 3, 13, 59, 60, 63, 66, 69, 73, 88–90).
- [26] Andrew Gillman, Kazuko Fuchi, Alexander Cook, Alexander Pankonien, and Philip R Buskohl. «Topology optimization for discovery of auxetic origami structures». In: *International Design Engineering Technical Conferences and Computers and Information in Engineering Conference*. Vol. 51814. American Society of Mechanical Engineers. 2018, V05BT07A059 (cit. on pp. 4, 63, 91, 102–108).
- [27] Songlin Yue. «A Review of Origami-Based Deployable Structures in Aerospace Engineering». In: *Journal of Physics: Conference Series*. Vol. 2459. 1. IOP Publishing. 2023, p. 012137 (cit. on pp. 4, 7).
- [28] Irene Iwasaki. *Japanese Origami: History, Facts and Purpose*. 2022. URL: <https://study.com/learn/lesson/japanese-origami-history-facts-purpose.html#:~:text=Origami%20is%20derived%20from%20the,China%20in%20the%206th%20century>. (visited on 09/18/2023) (cit. on p. 4).
- [29] Wikipedia. *File:The Alice (origami butterfly).jpg*. 2011. URL: [https://commons.wikimedia.org/wiki/File:The\\_Alice\\_%28origami\\_butterfly%29.jpg](https://commons.wikimedia.org/wiki/File:The_Alice_%28origami_butterfly%29.jpg) (visited on 09/17/2023) (cit. on p. 4).
- [30] Wikipedia. *File:Origami-crane.jpg*. 2006. URL: <https://it.m.wikipedia.org/wiki/File:Origami-crane.jpg> (visited on 09/17/2023) (cit. on p. 4).
- [31] Edwin A Peraza Hernandez, Darren J Hartl, Ergun Akleman, and Dimitris C Lagoudas. «Modeling and analysis of origami structures with smooth folds». In: *Computer-Aided Design* 78 (2016), pp. 93–106 (cit. on p. 5).

- [32] Edwin A Peraza Hernandez, Darren J Hartl, Dimitris C Lagoudas, Edwin A Peraza Hernandez, Darren J Hartl, and Dimitris C Lagoudas. «Kinematics of origami structures with smooth folds». In: *Active Origami: Modeling, Design, and Applications* (2019), pp. 201–268 (cit. on p. 5).
- [33] Marco Meloni, Jianguo Cai, Qian Zhang, Daniel Sang-Hoon Lee, Meng Li, Ruijun Ma, Teo Emilov Parashkevov, and Jian Feng. «Engineering Origami: A comprehensive review of recent applications, design methods, and tools». In: *Advanced Science* 8.13 (2021), p. 2000636 (cit. on pp. 6, 10, 11).
- [34] Miura Koryo. «Method of packaging and deployment of large membranes in space». In: *The Institute of Space and Astronautical Science report 618* (1985), pp. 1–9 (cit. on p. 7).
- [35] XM Xiang, G Lu, and Z You. «Energy absorption of origami inspired structures and materials». In: *Thin-Walled Structures* 157 (2020), p. 107130 (cit. on p. 7).
- [36] Koryo MIURA, Makoto NAGATOMO, Yoshinari MASUMOTO, Yuzo SHIBAYAMA, and Noboru MURANAKA. «A Conceptual Study on a Solar Sail Racer to the Moon». In: *The Journal of Space Technology and Science* 3.2 (1987), 2\_12–2\_21 (cit. on p. 7).
- [37] Garnett Horner and M Elliott. «A fabrication and deployment approach for a Miura-ori solar sail model». In: *43rd AIAA/ASME/ASCE/AHS/ASC Structures, Structural Dynamics, and Materials Conference*. 2002, p. 1708 (cit. on p. 8).
- [38] Sasaki Takashi. *Origami Techniques Applied to Space Development*. Public Relations Office, Government of Japan (visited on 05/08/2023). 2021. URL: [https://www.gov-online.go.jp/eng/publicity/book/hlj/html/202112/202112\\_05\\_en.html](https://www.gov-online.go.jp/eng/publicity/book/hlj/html/202112/202112_05_en.html) (cit. on p. 8).
- [39] Kyoichi Kuriki, Keiken Ninomiya, Mitsuru Takei, and Shinobu Matsuoka. «Lessons learned from the space flyer unit (SFU) mission». In: *Acta Astronautica* 51.11 (2002), pp. 797–806 (cit. on p. 8).
- [40] Y Shibayama, H Arai, K Matsui, K Hama, A Ushirokawa, M Natori, K Takahashi, N Wakasugi, and T Anzai. «SFU solar array». In: *European Space Power Conference*. Vol. 2. 1989, pp. 557–562 (cit. on p. 8).
- [41] Hajime Yano, S Kibe, SP Deshpande, and MJ Neish. «The first results of meteoroid and debris impact analyses on Space Flyer Unit». In: *Advances in Space Research* 20.8 (1997), pp. 1489–1494 (cit. on p. 8).
- [42] Mark Schenk and Simon D Guest. «Geometry of Miura-folded metamaterials». In: *Proceedings of the National Academy of Sciences* 110.9 (2013), pp. 3276–3281 (cit. on pp. 8, 91).

- [43] Zhiyan Y Wei, Zengcai V Guo, Levi Dudte, Haiyi Y Liang, and Lakshminarayanan Mahadevan. «Geometric mechanics of periodic pleated origami». In: *Physical review letters* 110.21 (2013), p. 215501 (cit. on p. 8).
- [44] Simon D Guest and Sergio Pellegrino. «Inextensional wrapping of flat membranes». In: *Proceedings of the first international seminar on structural morphology*. Vol. 25. 1992 (cit. on p. 9).
- [45] Shannon A Zirbel, Robert J Lang, Mark W Thomson, Deborah A Sigel, Phillip E Walkemeyer, Brian P Trease, Spencer P Magleby, and Larry L Howell. «Accommodating thickness in origami-based deployable arrays». In: *Journal of Mechanical Design* 135.11 (2013), p. 111005 (cit. on pp. 9, 12, 37, 56).
- [46] NASA Science. *Starshade to Enable First Images of Earth-sized Exoplanets*. 2016. URL: <https://science.nasa.gov/technology/technology-highlights/starshade-enable-first-images-earth-sized-exoplanets> (visited on 09/17/2023) (cit. on pp. 9, 10).
- [47] MechStuff. *NASA's Starshade to help find another Earth!* 2016. URL: <https://mechstuff.com/nasas-starshade-to-help-find-another-earth/> (visited on 09/17/2023) (cit. on p. 10).
- [48] Shannon A Zirbel, Brian P Trease, Mark W Thomson, Robert J Lang, Spencer P Magleby, and Larry H Howell. «Hanaflex: a large solar array for space applications». In: *Micro-and Nanotechnology Sensors, Systems, and Applications VII*. Vol. 9467. SPIE. 2015, pp. 179–187 (cit. on pp. 10, 11).
- [49] Tian Chen, Osama R Bilal, Robert Lang, Chiara Daraio, and Kristina Shea. «Autonomous deployment of a solar panel using elastic origami and distributed shape-memory-polymer actuators». In: *Physical Review Applied* 11.6 (2019), p. 064069 (cit. on p. 11).
- [50] National Aeronautics and Space Administration. *Bigelow Expandable Activity Module*. 2017. URL: <https://www.nasa.gov/content/bigelow-expandable-activity-module> (visited on 09/18/2023) (cit. on p. 12).
- [51] Jesse L Silverberg, Jun-Hee Na, Arthur A Evans, Bin Liu, Thomas C Hull, Christian D Santangelo, Robert J Lang, Ryan C Hayward, and Itai Cohen. «Origami structures with a critical transition to bistability arising from hidden degrees of freedom». In: *Nature materials* 14.4 (2015), pp. 389–393 (cit. on pp. 13, 98).
- [52] Li-Chen Wang, Wei-Li Song, Ya-Jing Zhang, Mei-Jun Qu, Zeang Zhao, Mingji Chen, Yazheng Yang, Haosen Chen, and Daining Fang. «Active reconfigurable tristable square-twist origami». In: *Advanced Functional Materials* 30.13 (2020), p. 1909087 (cit. on p. 13).



- [53] Krister Svanberg. «The method of moving asymptotes—a new method for structural optimization». In: *International journal for numerical methods in engineering* 24.2 (1987), pp. 359–373 (cit. on pp. 13, 34).
- [54] Philip E Gill, Walter Murray, and Margaret H Wright. *Numerical linear algebra and optimization*. SIAM, 2021 (cit. on p. 13).
- [55] Martin Philip Bendsøe and Noboru Kikuchi. «Generating optimal topologies in structural design using a homogenization method». In: *Computer methods in applied mechanics and engineering* 71.2 (1988), pp. 197–224 (cit. on p. 13).
- [56] George IN Rozvany, Ming Zhou, and Torben Birker. «Generalized shape optimization without homogenization». In: *Structural optimization* 4 (1992), pp. 250–252 (cit. on pp. 13, 39).
- [57] Erik Andreassen, Anders Clausen, Mattias Schevenels, Boyan S Lazarov, and Ole Sigmund. «Efficient topology optimization in MATLAB using 88 lines of code». In: *Structural and Multidisciplinary Optimization* 43 (2011), pp. 1–16 (cit. on pp. 13, 39).
- [58] João Carlos Alves Barata and Mahir Saleh Hussein. «The Moore–Penrose pseudoinverse: A tutorial review of the theory». In: *Brazilian Journal of Physics* 42.1 (2012), pp. 146–165 (cit. on p. 29).
- [59] Ole Sigmund and Kurt Maute. «Topology optimization approaches». In: *Structural and Multidisciplinary Optimization* 48.6 (2013), pp. 1031–1055 (cit. on p. 34).
- [60] Robert B Wilson. «A simplicial algorithm for concave programming». In: *Ph. D. Dissertation, Graduate School of Business Administration* (1963) (cit. on p. 34).
- [61] Colin Donald Chapman. «Structural topology optimization via the genetic algorithm». PhD thesis. Massachusetts Institute of Technology, 1994 (cit. on p. 34).
- [62] Ji-Hong Zhu, Wei-Hong Zhang, and Liang Xia. «Topology optimization in aircraft and aerospace structures design». In: *Archives of computational methods in engineering* 23 (2016), pp. 595–622 (cit. on p. 35).
- [63] Wenjiong Gu. «On challenges and solutions of topology optimization for aerospace structural design». In: *10th World Congress on Structural and Multidisciplinary Optimization, May*. 2013, pp. 19–24 (cit. on p. 35).
- [64] David J Munk, Douglass J Auld, Grant P Steven, and Gareth A Vio. «On the benefits of applying topology optimization to structural design of aircraft components». In: *Structural and Multidisciplinary Optimization* 60 (2019), pp. 1245–1266 (cit. on p. 35).

- [65] Laura Berrocal et al. «Topology optimization and additive manufacturing for aerospace components». In: *Progress in Additive Manufacturing* 4 (2019), pp. 83–95 (cit. on p. 35).
- [66] Mark Schenk and Simon D Guest. «Origami folding: A structural engineering approach». In: *5OSME, 5th international conference on Origami in Science, Mathematics and Education*. Retrieved from: <http://www.markschenk.com/research/#papers>. 2010 (cit. on p. 36).
- [67] Katsuyuki Suzuki and Noboru Kikuchi. «A homogenization method for shape and topology optimization». In: *Computer methods in applied mechanics and engineering* 93.3 (1991), pp. 291–318 (cit. on p. 39).
- [68] Kazuko Fuchi. *Origami Mechanism Topology Optimizer (OMTO) Ver 1.1n*. MATLAB Central File Exchange (visited on 05/08/2023). 2015. URL: <https://www.mathworks.com/matlabcentral/fileexchange/53037-origami-mechanism-topology-optimizer-omto-ver-1-1n> (cit. on pp. 44, 50).
- [69] Bryce J Edmondson, Landen A Bowen, Clayton L Grames, Spencer P Magleby, Larry L Howell, and Terri C Bateman. «Oriceps: Origami-inspired forceps». In: *Smart Materials, Adaptive Structures and Intelligent Systems*. Vol. 56031. American Society of Mechanical Engineers. 2013, V001T01A027 (cit. on p. 44).
- [70] Shuhei Miyashita, Steven Guitron, Marvin Ludersdorfer, Cynthia R Sung, and Daniela Rus. «An untethered miniature origami robot that self-folds, walks, swims, and degrades». In: *2015 IEEE international conference on robotics and automation (ICRA)*. IEEE. 2015, pp. 1490–1496 (cit. on p. 44).
- [71] Dae-Young Lee, Sa-Reum Kim, Ji-Suk Kim, Jae-Jun Park, and Kyu-Jin Cho. «Origami wheel transformer: A variable-diameter wheel drive robot using an origami structure». In: *Soft robotics* 4.2 (2017), pp. 163–180 (cit. on p. 44).
- [72] Nam-Ho Kim. *Introduction to nonlinear finite element analysis*. Springer Science & Business Media, 2014 (cit. on p. 54).
- [73] Aurel Galántai. «The theory of Newton’s method». In: *Journal of Computational and Applied Mathematics* 124.1-2 (2000), pp. 25–44 (cit. on p. 55).
- [74] Andrew Gillman, Kazuko Fuchi, and PR Buskohl. *Origami Topology Optimization w/ Nonlinear Truss Model*. MATLAB Central File Exchange, Retrieved December 5, 2018 (visited on 06/06/2023). 2018. URL: <https://www.mathworks.com/matlabcentral/fileexchange/69612-origami-topology-optimization-w-nonlinear-truss-model> (cit. on pp. 63, 98–100).
- [75] M Fanni, MN Shabara, and MG Alkalla. «A Comparison between Different Topology Optimization Methods.» In: *MEJ. Mansoura Engineering Journal* 38.4 (2020), pp. 13–24 (cit. on p. 69).

- 
- [76] Thomas Hull. *The Augmented Square Twist*. 2018. URL: <http://origametry.net/ast/ast.html> (visited on 09/17/2023) (cit. on p. 71).
- [77] MathWorks. *How the Genetic Algorithm Works*. 2023. URL: <https://it.mathworks.com/help/gads/how-the-genetic-algorithm-works.html> (visited on 09/18/2023) (cit. on p. 87).
- [78] MathWorks. *What Is the Genetic Algorithm?* 2015. URL: <https://it.mathworks.com/help/gads/what-is-the-genetic-algorithm.html> (visited on 09/17/2023) (cit. on p. 88).
- [79] He Zhang, Chunwei Yang, Ying Yu, Yuhui Zhou, Liwei Quan, Shurong Dong, and Jikui Luo. «Origami-tessellation-based triboelectric nanogenerator for energy harvesting with application in road pavement». In: *Nano Energy* 78 (2020), p. 105177 (cit. on p. 91).
- [80] Scott Waitukaitis, Rémi Menaut, Bryan Gin-ge Chen, and Martin Van Hecke. «Origami multistability: From single vertices to metasheets». In: *Physical review letters* 114.5 (2015), p. 055503 (cit. on p. 91).
- [81] Amir A Zadpoor. «Mechanical meta-materials». In: *Materials Horizons* 3.5 (2016), pp. 371–381 (cit. on p. 91).
- [82] Elisa Boatti, Nikolaos Vasios, and Katia Bertoldi. «Origami metamaterials for tunable thermal expansion». In: *Advanced Materials* 29.26 (2017), p. 1700360 (cit. on p. 91).
- [83] Yves Dubois-Pèlerin and Pierre Pegon. «Linear constraints in object-oriented finite element programming». In: *Computer Methods in Applied Mechanics and Engineering* 154.1-2 (1998), pp. 31–39 (cit. on p. 92).
- [84] Javier Bonet and Richard D Wood. *Nonlinear continuum mechanics for finite element analysis*. Cambridge university press, 1997 (cit. on p. 94).
- [85] Peter Wriggers. *Nonlinear finite element methods*. Springer Science & Business Media, 2008 (cit. on p. 94).
- [86] P Wriggers. *Non-linear finite element analysis of solids and structures, volume 1: Essentials, MA Crisfield, John Wiley. ISBN: 0-471-92956-5*. 1994 (cit. on p. 94).
- [87] Cinthia AG Sousa and Paulo M Pimenta. «A new parameter to arc-length method in nolinear structural analysis». In: *Mecánica Computacional* 29.17 (2010), pp. 1841–1848 (cit. on p. 94).
- [88] K Fuchi, PR Buskohl, JJ Joo, GW Reich, and RA Vaia. «Numerical analysis of origami structures through modified frame elements». In: *Origami6; Miura, K., Kawasaki, T., Tachi, T., Uehara, R., Lang, RJ, Wang-Iverson, P., Eds* (2016), pp. 385–395 (cit. on p. 97).

- [89] Eli Davis, Erik D Demaine, Martin L Demaine, and Jennifer Ramseyer. «Reconstructing David Huffman’s origami tessellations». In: *Journal of Mechanical Design* 135.11 (2013), p. 111010 (cit. on p. 98).
- [90] HC Greenberg, ML Gong, SP Magleby, and LL Howell. «Identifying links between origami and compliant mechanisms». In: *Mechanical Sciences* 2.2 (2011), pp. 217–225 (cit. on p. 98).
- [91] Thomas A Evans, Robert J Lang, Spencer P Magleby, and Larry L Howell. «Rigidly foldable origami gadgets and tessellations». In: *Royal Society open science* 2.9 (2015), p. 150067 (cit. on p. 98).

# Appendix A

## Inclusion of a Genetic Algorithm to the Optimization Process

Gradient-based methods have proven to be efficient algorithms in finding the optimal solution with a fast convergence rate. However, they tend to converge in local minima for non-convex problems. In the Square Twist example in Chapter 4, the SQP method did not discover the targeted flat folded configuration. Therefore, a non-gradient-based method like the *Genetic Algorithm* (GA) must be employed.

GA is based on natural selection from biology and it is able to solve highly nonlinear problems. A population of unique solutions is repeatedly modified, choosing at each iteration step members from the current populations to be parents and using them to produce the children of the next generation. The population "evolves" towards the optimal solution over the course of succeeding generations [77]. To produce the next generation from the existing population, GA applies three rules at each stage:

- *Selection rule*: stochastic selection of the parents of the population;
- *Crossover rule*: combination of the parents to form the next generation children;
- *Mutation rule*: application of random mutation to the parents.

Therefore, unlike gradient-based algorithms where a single point is generated at each iteration to approach the optimal solution, GA generates a population of points at each iteration and the best point of that population approaches the optimal

solution. However, the drawback is that convergence is not guaranteed and the computational cost is high since GA typically needs many functions to converge [78].

Gillman et al. [24, 25] developed the Genetic Algorithm described as follows. The design variable  $\alpha$  is used as the chromosome vector in the optimization process and it is binarized to take on values of 0 or 1 to represent the soft and stiff folds (with  $G = G_{soft}$  and  $G = G_{stiff}$ ), respectively. Fig. A.1 shows both single-point and uniform crossover operators for a starting configuration with eight fold lines (considering the nonlinear truss model in Chapter 4).

It is crucial to consider that crossover may lead to the violation of the inequality constraint  $g_1 \leq 0$ . Therefore, an algorithm is employed to turn randomly a design variable from 0 to 1 to satisfy the constraint. Moreover, a mutation rate of at least a set percentage is applied to ensure that the population at the next iteration is diverse. However, the best designs with respect to the objective function value are maintained to increase the efficiency of the method.

In order to consider also axial rigidity  $EA$  as a design variable in the described optimization method, the design variable  $\beta$  must be included in the chromosome vector following the same procedure used for  $\alpha$ . Therefore, the chromosome vector becomes  $\mathbf{x} = \alpha_1, \dots, \alpha_{N_f}, \beta_1, \dots, \beta_{N_e}$ , where  $N_f$  is the number of folds and  $N_e$  the number of truss elements. However, the design complexity could significantly increase, therefore the computational cost and the convergence rate of the problems must be assessed.

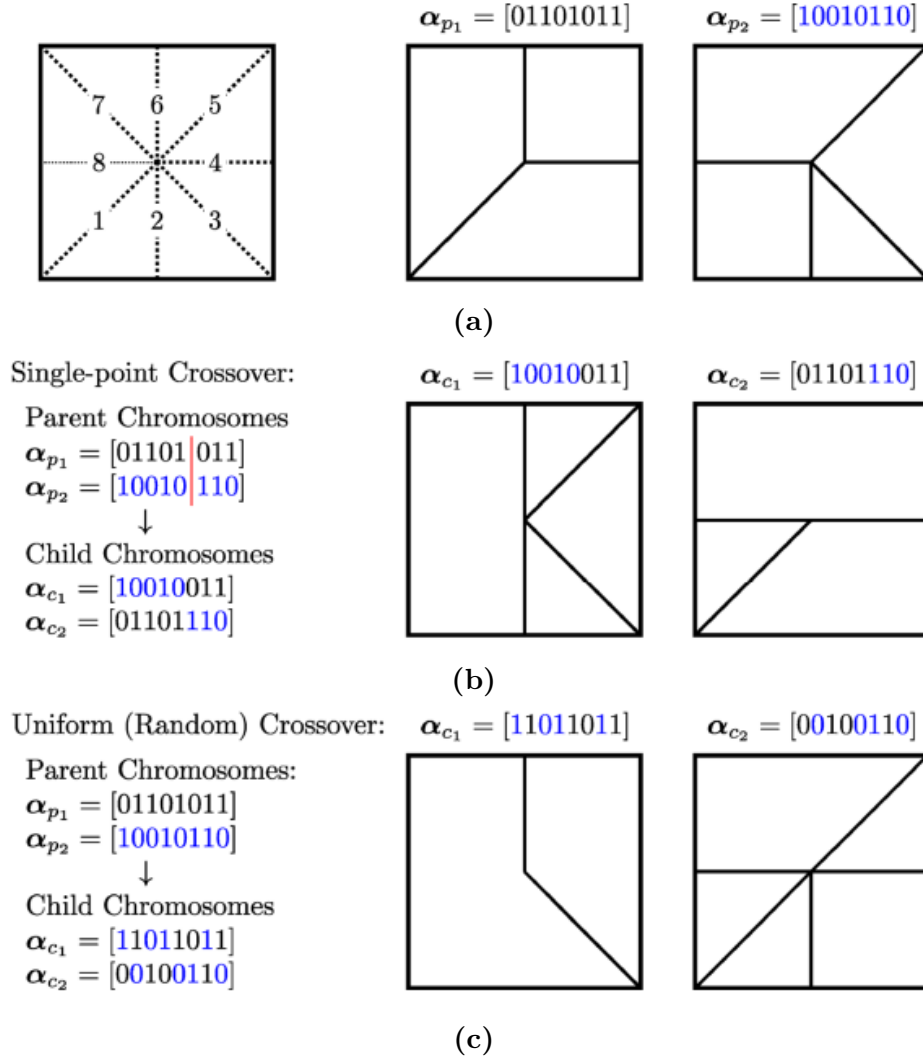
Nevertheless, the potential of the Genetic Algorithm introduced by Gillman et al. [25] is appraised as follows through the results obtained using only the fold stiffness as a design variable for the Square Twist fold pattern shown in Chapter 4.

## **Square Twist Pattern with a Genetic Algorithm**

A uniform (random) crossover is considered in this example. Also, a repair function enforces all members in the populations to have always the same number of active fold lines, satisfying the inequality constraint  $g_1 \leq 0$ .

The results before the post-optimization are displayed in Fig. A.2, where Fig. A.2a shows the asymmetric optimized crease pattern and Fig. A.2b the resulting folded configuration.

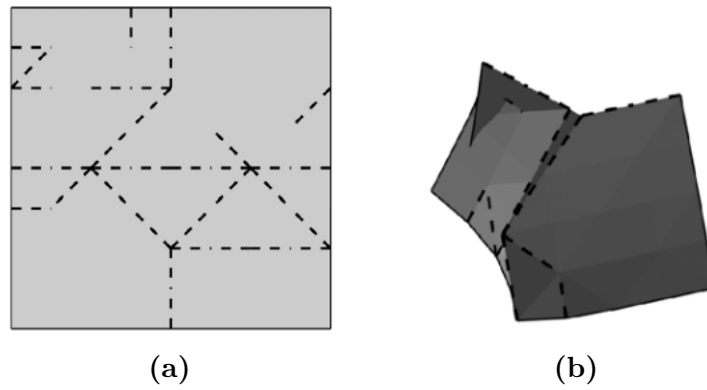
The Genetic Algorithm frequently fails to achieve a symmetric solution. Therefore, to obtain symmetry, the bottom half of the crease pattern obtained is mirrored on the upper half, as in Fig. A.3.



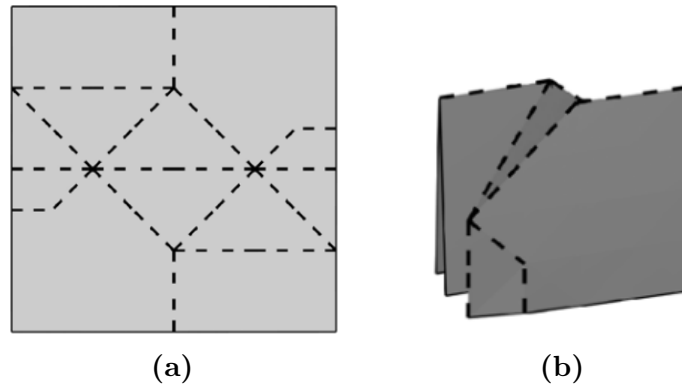
**Figure A.1:** Crossover operators for an origami with eight fold lines, where  $\alpha_k = 0$  represents a soft active fold, while  $\alpha_k = 1$  represents a stiff inactive fold. (a) Reference grid and parent chromosome vectors,  $\alpha_{p_1}$  and  $\alpha_{p_2}$ ; (b) single-point crossover and relative next iteration children,  $\alpha_{c_1}$  and  $\alpha_{c_2}$ ; (c) Uniform crossover and relative next iteration children,  $\alpha_{c_1}$  and  $\alpha_{c_2}$  [25].

The obtained configuration is perfectly flat, yielding nearly equivalent performances to the known square twist fold pattern in Fig. 1.12.

In this case, the addition of axial rigidity as a design variable could lead to the same or different crease patterns that still achieve the targeted flat folded



**Figure A.2:** Results for the Square Twist pattern using GA (design variable:  $\alpha$ ), where the dashed lines are the soft active folds. (a) Optimized Crease Pattern; (b) Folded Configuration ( $f = -0.775 \text{ mm}$ ) [25].



**Figure A.3:** Mirrored results of Fig. A.2. (a) Optimized Crease Pattern; (b) Flat Folded Configuration ( $f = -0.830 \text{ mm}$ ) [25].

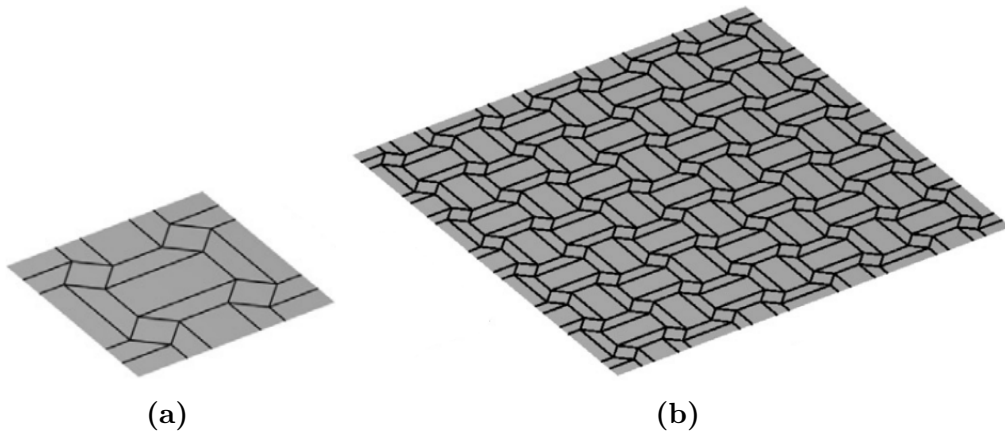
configuration, although requiring a lower actuation load since the structure is allowed to be more flexible.



## Appendix B

# Origami Structures with Tesselation Patterns

In their applications, origami structures are frequently used with *tesselation patterns*, in which a crease pattern is repeated along various directions, crucial for their employment as mechanical metamaterials [42, 79, 80, 81, 82]. An example of a tesselation pattern is the Square Twist Tesselation in Fig. B.1.



**Figure B.1:** Square Twist Tesselation. (a) Single unit cell; (b) Tesselation pattern of (a) [15].

Following the procedure applied by Gillman et al. [15, 26], to analyze these patterns with the nonlinear model introduced in Chapter 4, it is necessary to enforce *periodic boundary conditions* at the boundaries.

Furthermore, a *Lagrange multiplier* is used to relate the strains on opposite boundaries of each unit cell. This approach can be employed together with classical Dirichlet boundary conditions since both types of constraints can be expressed as linear constraints [83] as

$$\begin{aligned} q_l(X_{tri}) - F_l + A_{ls}^T \lambda_s &= 0 \\ A_{ls}^T X_s - \bar{X}_l &= 0 \end{aligned} \quad (B.1)$$

where  $A_{ls}$  is the matrix of the coefficient in the constraint equation and  $\bar{X}_l$  is the location of the selected nodes at a certain load step. With respect to the example in Fig. B.2, to introduce the periodic boundary conditions, the displacements are constrained as follows

$$\mathbf{X}_2 - \mathbf{X}_1 = \mathbf{X}'_1 - \mathbf{X}'_2. \quad (B.2)$$

Nevertheless, "ghost nodes" are required to further ensure that the displacement  $\mathbf{X}'_1 - \mathbf{X}'_2$  matches the displacement  $\mathbf{X}_2 - \mathbf{X}_1$ :

$$\mathbf{X}_4 = \mathbf{X}_2 + (\mathbf{X}'_3 - \mathbf{X}'_1). \quad (B.3)$$

Therefore, the fold angle is now a function of five nodes locations:

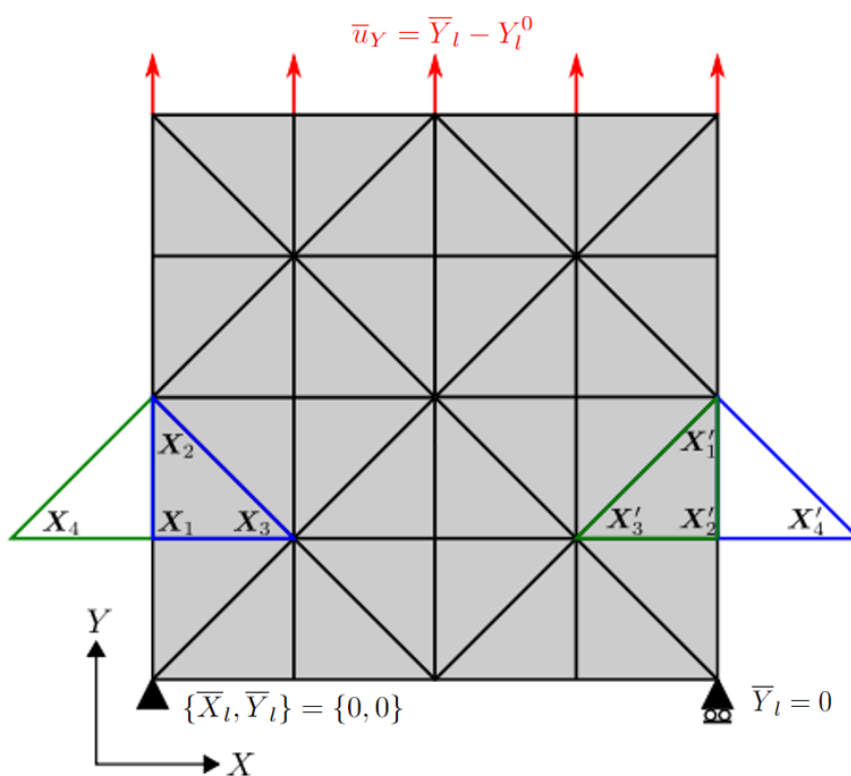
$$\phi = \phi(\mathbf{X}_1, \mathbf{X}_2, \mathbf{X}_3, \mathbf{X}_4) = \phi(\mathbf{X}_1, \mathbf{X}_2, \mathbf{X}_3, \mathbf{X}'_1, \mathbf{X}'_3). \quad (B.4)$$

Lastly, with period boundary conditions, Eq. 4.12 becomes

$$\begin{bmatrix} {}^n \mathbf{K} & \mathbf{A}^T \\ \mathbf{A} & \mathbf{0} \end{bmatrix} \begin{Bmatrix} {}^n_{m+1} \Delta \mathbf{X} \\ {}^n_{m+1} \Delta \lambda \end{Bmatrix} = \begin{Bmatrix} {}^n \mathbf{q} - {}^n \mathbf{F} - \mathbf{A}^T \cdot {}^n_m \lambda \\ {}^n \bar{\mathbf{X}} - \mathbf{A}^T \cdot {}^n_m \lambda \end{Bmatrix}, \quad (B.5)$$

where the subscripts  $m$  and superscripts  $n$  are the nonlinear iteration step and the iteration step, respectively.

The residual  $\mathbf{R}$  and the tangent matrix  $\mathbf{K}$  could be computed as in Eq.s (4.10) and (4.11) to account for the two sets of design variables employed in the optimization method in Chapter 4: the fold stiffness  $G$  and the axial rigidity  $EA$ .



**Figure B.2:** Enforcement of Dirichlet boundary conditions using Lagrange multiplier approach for a unit cell [15].

## Appendix C

# Critical Points Analysis in Origami Structures

As introduced in Section 4.3, during each iteration cycle to solve the linearized system of equations in Eq. (4.12), a Newton-Raphson approach is employed, considering monotonically increasing loads. However, origami structures usually exhibit more complex nonlinear behavior and this approach is unable to capture equilibrium paths beyond limit points [13, 20, 84, 85, 86] like displacement limit points (snap-back points), hence non-monotonic loading path needs to be considered.

A powerful numerical technique for solving systems of nonlinear equations when the problem under consideration exhibits one or more critical points is the *arc-length method*, first introduced by Riks [17, 18] and Wempner [19]. In this approach, the path through a converged solution follows an orthogonal direction to the tangent of the solution curve. Furthermore, both the load vector and the displacement field are additional variables, so the method adds a constraint condition to the set of nonlinear equations to determine them [87].

Various arc-length methods were analyzed by Leon et al. [20], who introduced a *Modified Generalized Displacement Control Method* (MGDCM) in Reference [21], that allowed for the accurate and efficient solution for the system of nonlinear equations while automatically modifying the step size based on the loading profile curvature. Subsequently, Filipov et al. [12] and Liu and Paulino [13] used this nonlinear approach to simulate the loads of truss origami structures.

To apply an arc-length method to the optimization method in Chapter 4, a scalar Lagrange multiplier ( $\lambda_F$ ) is used to scale the applied force vector  $\mathbf{F}$ , resulting in the nonlinear equation system shown below

$$\begin{aligned} q_l(X_{tri}) - \lambda_F F_l + A_{ls}^T \lambda_s &= 0 \\ A_{ls}^T X_s - \bar{X}_l &= 0 \end{aligned} \quad (C.1)$$

Following the procedure in [15, 21], linearizing Eq. (C.1) with respect to the global position  $\mathbf{X}$  the following system is obtained

$${}^n_m \mathbf{K} \cdot {}^n_{m+1} \Delta \mathbf{X} + \mathbf{A}^T \cdot {}^n_{m+1} \Delta \boldsymbol{\lambda} = {}^n_m \Delta \lambda_F \mathbf{F} + {}^n_m \mathbf{q} - {}^n_m \lambda_F \cdot \mathbf{F} - \mathbf{A}^T \cdot {}^n_m \boldsymbol{\lambda}. \quad (C.2)$$

As aforementioned, the arc-length method with the scalar Lagrange multiplier  $\lambda_F$  needs a generalized constraint equation with respect to  ${}^n_{m+1} \Delta \lambda_F$  and  ${}^n_{m+1} \Delta \mathbf{X}$

$${}^n_{m+1} \mathbf{a} \cdot {}^n_{m+1} \Delta \mathbf{X} + {}^n_{m+1} b \cdot {}^n_{m+1} \Delta \lambda_F = {}^n_{m+1} c, \quad (C.3)$$

which is a linear constraint, whose change in global position can be decomposed into two parts that can be solved separately,  $\Delta \mathbf{X}_p$  and  $\Delta \mathbf{X}_r$ :

$${}^n_{m+1} \Delta \mathbf{X} = {}^n_{m+1} \Delta \lambda_F \cdot {}^n_{m+1} \Delta \mathbf{X}_p + {}^n_{m+1} \Delta \mathbf{X}_r. \quad (C.4)$$

In the MGDCM,  $\mathbf{a}$ ,  $b$  and  $c$  are later defined as

$${}^n_{m+1} \mathbf{a} = {}^n_{m+1} \Delta \lambda_F \cdot {}^n_{m+1} \Delta \mathbf{X}_p; \quad (C.5)$$

$${}^n_{m+1} b = 0; \quad (C.6)$$

$${}^n_{m+1} c = ({}^1_1 \Delta \lambda_F)^2 \cdot {}^1_1 \Delta \mathbf{X}_p \cdot {}^1_1 \Delta \mathbf{X}_p. \quad (C.7)$$

Next, the two following systems are solved separately at each nonlinear iteration  $m$

$$\begin{bmatrix} {}^n_m \mathbf{K} & \mathbf{A}^T \\ \mathbf{A} & \mathbf{0} \end{bmatrix} \begin{Bmatrix} {}^n_{m+1} \Delta \mathbf{X}_p \\ {}^n_{m+1} \Delta \lambda_p \end{Bmatrix} = \begin{Bmatrix} \mathbf{F} - \mathbf{A}^T \cdot {}^n_m \boldsymbol{\lambda}_p \\ {}^n_m \bar{\mathbf{X}} - \mathbf{A}^T \cdot {}^n_m \mathbf{X} \end{Bmatrix} \quad (C.8)$$

and

$$\begin{bmatrix} {}^n_m \mathbf{K} & \mathbf{A}^T \\ \mathbf{A} & \mathbf{0} \end{bmatrix} \begin{Bmatrix} {}^n_{m+1} \Delta \mathbf{X}_r \\ {}^n_{m+1} \Delta \lambda_r \end{Bmatrix} = \begin{Bmatrix} {}^n_m \lambda_F \cdot {}^n_m \mathbf{F} - {}^n_m \mathbf{q} - \mathbf{A}^T \cdot {}^n_m \boldsymbol{\lambda}_r \\ {}^n_m \bar{\mathbf{X}} - \mathbf{A}^T \cdot {}^n_m \mathbf{X} \end{Bmatrix}. \quad (C.9)$$

Lastly, the load update is determined as

$${}^n_{m+1}\Delta\lambda_F = \begin{cases} \overline{\Delta\lambda_F} & n = 1 \text{ and } k = 1 \\ -\frac{{}^1_1\Delta\mathbf{X}_p \cdot {}^1_m\Delta\mathbf{X}_r}{{}^1_1\Delta\mathbf{X}_p \cdot {}^1_m\Delta\mathbf{X}_p} & n = 1 \text{ and } k > 1 \\ \pm\overline{\Delta\lambda_F} \left| \frac{{}^1_1\Delta\mathbf{X}_p \cdot {}^1_1\Delta\mathbf{X}_r}{{}^n_1\Delta\mathbf{X}_p \cdot {}^n_1\Delta\mathbf{X}_p} \right|^{1/2} & n > 1 \text{ and } k = 1 \\ -\frac{{}^n_1\Delta\mathbf{X}_p \cdot {}^n_m\Delta\mathbf{X}_r}{{}^n_1\Delta\mathbf{X}_p \cdot {}^n_m\Delta\mathbf{X}_p} & n > 1 \text{ and } k > 1 \end{cases} \quad (\text{C.10})$$

where  $\overline{\Delta\lambda_F}$  is the prescribed initial load factor. An overview of the solution process is displayed in Algorithm 1.

---

**Algorithm 1** MGDCM algorithm overview applied to origami truss finite elements based on global positional formulation [15].

---

- 1: Set  ${}^{n=1}_{m=1}\mathbf{X} = \mathbf{X}_0$ ,  $\mathbf{F} = \overline{\mathbf{F}}$ ,  ${}^1_1\boldsymbol{\lambda} = \mathbf{0}$ ,  ${}^1_1\lambda_F = 0$ ,  $\mathbf{A}$  ▷ Initialize parameters
  - 2: **for**  $n = 1 : N_{load \ step}$  **do**
  - 3:     Set  $k = 1$
  - 4:     Set  ${}^n\overline{\mathbf{X}}$  ▷ Set prescribed position vector
  - 5:     **while**  $|\Delta\mathbf{X}_m|/|\Delta\mathbf{X}_1| > tol$  and  $|\mathbf{R}_m|/|\mathbf{R}_1| > tol$  **do** ▷ Continue until displacement changes and residual are below tolerance
  - 6:         Find  ${}^n_m\mathbf{K}({}^n_m\mathbf{X})$  and  ${}^n_m\mathbf{q}({}^n_m\mathbf{X})$
  - 7:         Solve Eq.s (C.7) and (C.8) for  ${}^n_{m+1}\Delta\mathbf{X}_p$ ,  ${}^n_{m+1}\Delta\mathbf{X}_r$ ,  ${}^n_{m+1}\Delta\boldsymbol{\lambda}_p$  and  ${}^n_{m+1}\Delta\boldsymbol{\lambda}_r$
  - 8:         Compute  ${}^n_{m+1}\Delta\lambda_F$  through Eq. (C.9)
  - 9:         Set  ${}^n_{m+1}\Delta\mathbf{X} = {}^n_{m+1}\Delta\lambda_F \cdot {}^n_m\Delta\mathbf{X}_p + {}^n_m\Delta\mathbf{X}_r$
  - 10:         Set  ${}^n_{m+1}\mathbf{X} = {}^n_m\mathbf{X} + {}^n_{m+1}\Delta\mathbf{X}$
  - 11:         Set  ${}^n_{m+1}\boldsymbol{\lambda}_p = {}^n_m\boldsymbol{\lambda}_p + {}^n_{m+1}\Delta\boldsymbol{\lambda}_p$ ,  ${}^n_{m+1}\Delta\boldsymbol{\lambda}_r = {}^n_m\boldsymbol{\lambda}_r + {}^n_{m+1}\Delta\boldsymbol{\lambda}_r$  and  ${}^n_{m+1}\lambda_F = {}^n_m\lambda_F + {}^n_{m+1}\Delta\lambda_F$
  - 12:         Set  $k = k + 1$
  - 13:     **end while**
  - 14: **end for**
-

## Appendix D

# Equilibrium Bifurcations Analysis in Origami Structures

In the previous Section, Algorithm 1 is described to analyze origami structures with complex nonlinear mechanics. However, this method is insufficient in distinguishing and following multiple *bifurcation branches*, which has long been a problem with nonlinear finite elements. As a remark, for energy or force-displacement, a critical point with bifurcating branches is the point of intersection of multiple equilibrium loading paths.

Regarding origami structures, a critical point is the *flat state*, which frequently presents several bifurcating branches. For example, during an in-plane loading of a two-dimensional sheet, the procedure in Section C can only lead to a flat final configuration, even though more energetically advantageous out-of-plane branches are possible.

To overcome this limitation, Schenk et al. [9] studied *modal analysis* of non-flat origami structures, which was then employed from the flat state in a linear model by Fuchi et al. [88]. To improve on this formulation, Gillman et al. [15] included modal analysis in the modified nonlinear truss model as described as follows. A perturbation force field is introduced to study the bifurcation branches through modal analysis. First, the *augmented stiffness matrix* ( $K_{aug}$ ) is described as

$${}^n_m \mathbf{K}_{aug} = \begin{bmatrix} {}^n_m \mathbf{K} & \mathbf{A}^T \\ \mathbf{A} & \mathbf{0} \end{bmatrix}. \quad (\text{D.1})$$

To carry out the modal analysis, Eq. (D.1) is evaluated at the first nonlinear step ( $k = 1$ ) of the first load step ( $n = 1$ ). Then, the *eigenvalue problem* of modal analysis for the augmented stiffness matrix is presented

$$\boxed{({}_1\mathbf{K}_{aug} - \theta_v \mathbf{I})\mathbf{v} = 0}, \quad (\text{D.2})$$

where  ${}_t\theta_v$  are the eigenvalues and  ${}_t\mathbf{v}$  are the eigenvectors of mode  $t$ . Therefore, the eigenvectors associated with the lowest positive eigenvalues are the lowest energy deformation modes from the flat state. These selected eigenvectors are utilized to evaluate the perturbation force field ( $\mathbf{F}_{perturb}$ ), applied on the initial loading step ( $n = 1$ ) and set to zero for all the subsequent loading steps ( $n > 1$ ).

Algorithm 2 provides a more thorough explanation. Furthermore, this algorithm is used to investigate bifurcation branches between lines 6 and 7 of Algorithm 1.

---

**Algorithm 2** Algorithm to determine the perturbation force to study origami bifurcation off the flat state [15].

---

- 1: **if**  $n = 1$  and  $m = 1$  **then**
  - 2:     Set  ${}_1\mathbf{X} = {}_1\mathbf{X}_0 + (0.01\mathbf{F}/|\mathbf{F}|) \max(\mathbf{X}_0)$   $\triangleright$  Set in-plane loading on boundary
  - 3:     Solve  $({}_1\mathbf{K}_{aug} - \theta_v \mathbf{I})\mathbf{v} = 0 \quad \forall {}_t\theta_v$  and  ${}_t\mathbf{v}$   $\triangleright$  Solve eigenvalue problem
  - 4:     Set  $\mathbf{F}_{perturb} = {}_t\theta_v \cdot {}_1\mathbf{K}_{aug} \cdot {}_t\mathbf{v}$   $\triangleright$  Determine perturbation force for selected mode  $t$
  - 5:     Set  ${}_1X = \mathbf{X}_0 + {}_t\mathbf{v}$
  - 6:     Recompute  ${}_1\mathbf{K}({}_1\mathbf{X})$  and  ${}_1\mathbf{R}({}_1\mathbf{X})$
  - 7: **else if**  $n > 1$  **then**
  - 8:     Set  $\mathbf{F}_{perturb} = \mathbf{0}$
  - 9: **end if**
  - 10: Set  $\mathbf{F} = \mathbf{F} + \mathbf{F}_{perturb}$   $\triangleright$  Update applied force vector
- 

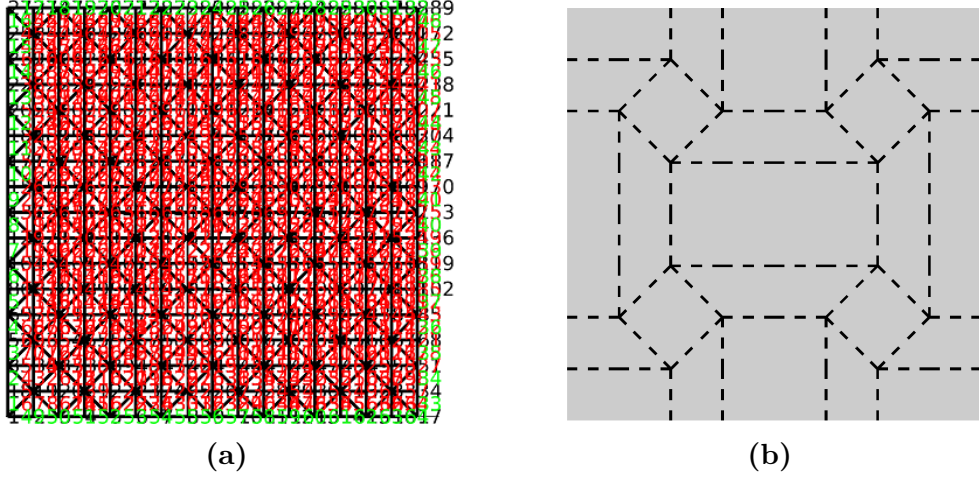
This method can be applied to the optimization process in Chapter 4 considering the tangent stiffness matrix introduced in Eq. (4.11) as a function of the fold stiffness  $G$  and the axial rigidity  $EA$ , in order to analyze new origami bifurcation off the flat state.

Lastly, the potential of the equilibrium bifurcation analysis is briefly assessed in the following example from Gillman et al. [15] with the optimizer in Reference [74] for the unit cell of the Square Twist Tessellation fold pattern shown in Fig. B.1a. This fold pattern was studied in several works [51, 89, 90, 91].



## Modal Analysis of the Unit Cell of the Tessellated Square Twist

The starting configuration in Fig. D.1 presents 736 fold lines and 800 truss elements.

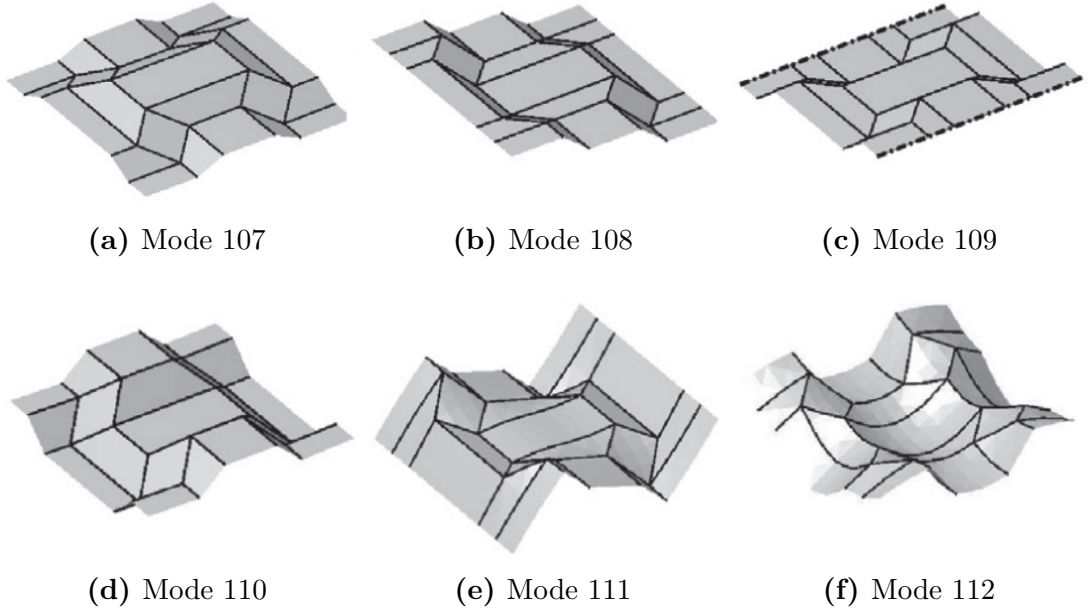


**Figure D.1:** Starting configuration of the unit cell of the Square Twist Tessellation pattern. (a) Reference grid; (b) Crease pattern ( $L_x = 0.8 \text{ m}$ ,  $L_y = 0.8 \text{ m}$ ).

The modal analysis calculates the natural frequencies of the system alone, therefore it is performed without loads and boundary conditions. It can be noted that the fold pattern in Fig. D.1b is already known, where the dashed lines are the soft active folds with  $G = G_{soft} = 10^0 \text{ Pa} \cdot \text{m}^2$ , while the fold lines that are not shown are the stiff inactive fold lines with  $G = G_{stiff} = 10^4 \text{ Pa} \cdot \text{m}^2$ . Moreover, in this case, the axial rigidity among the trusses is kept constant to  $EA = 10^5 \text{ Pa} \cdot \text{m}^2$ .

The arc-length method introduced in Section C and the periodic boundary conditions described in Section B are included in the formulation. Also, the Square Twist unit cell presents many bifurcation paths off the flat state, therefore the perturbation approach in Algorithm 2 is applied.

Through the nonlinear optimizer in Reference [74], the modal analysis can be carried out, obtaining the modes in Fig. D.2.



**Figure D.2:** Modal analysis for the Square Twist unit cell tessellation carried out with the optimizer in Reference [74] to obtain the deformed configurations of the lowest energy positive mode shapes.

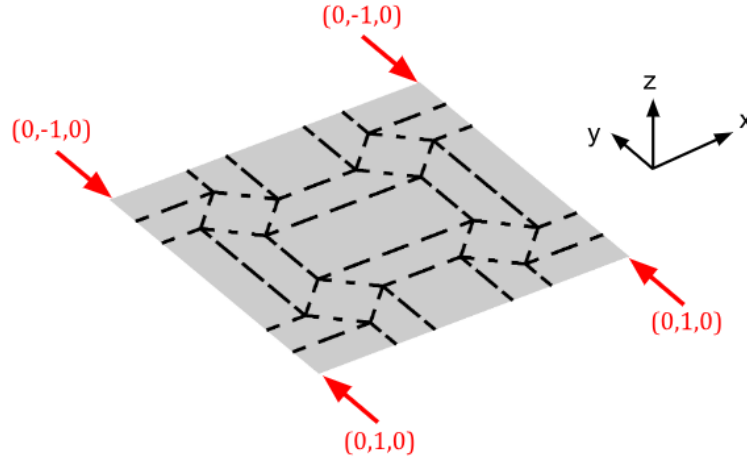
Fig. D.2 presents the resulting lowest positive eigenvalues. As a matter of fact, the first 106 eigenvalues are negative or null since there are:

- 96 degrees of freedom due to the 32 boundary truss elements;
- 10 degrees of freedom due to the fixed nodal constraints of the center panel to remove rigid body motion.

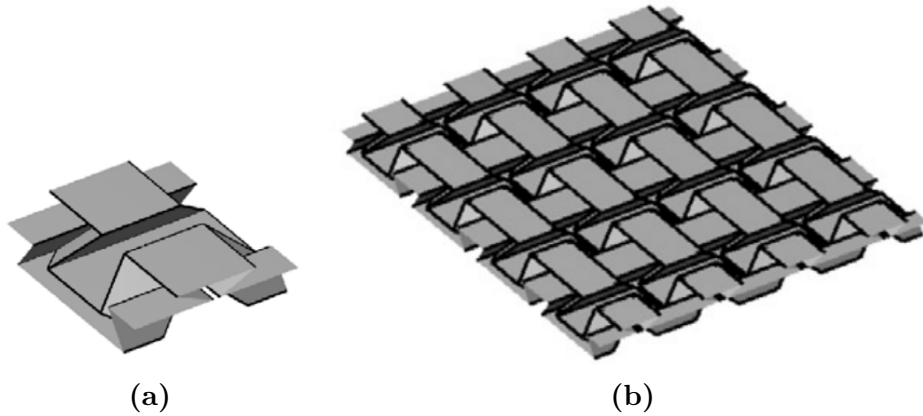
It can be noted that the first four modes (from mode 107 to 110) manifest modest stretching without any facet bending. However, mode 111 registers significant facet stretching, while mode 112 registers significant facet bending, hence they reach considerably higher eigenvalues than the previous modes.

This modal analysis is used to create the perturbation force field and track a bifurcation loading path off the flat state. Therefore, it is possible to perform the nonlinear simulation applying the loading conditions in Fig. D.3 to the structure, where the red arrow are the external nodal forces.

The MGDCM in Section C is used to scale the force in the loading process, while the perturbation force is only applied in the first step, as described by Algorithm 2. Applying the described process to mode 110, the configuration in Fig. D.4a is obtained, which can be mirrored to obtain the final folded Square Twist Tessellation pattern in Fig. D.4b, with four unit cells along  $x$  and  $y$ .



**Figure D.3:** Loading conditions to carry out the nonlinear simulation with periodic boundary conditions and MGDCM.



**Figure D.4:**  $4 \times 4$  Final folded Square Twist Tessellation pattern obtained with periodic boundary conditions [15].

From this example it is possible to deduct that, if axial rigidity would be allowed to vary among the trusses, new modes could be discovered, potentially leading to new folded configurations.

## Appendix E

# Topology Optimization for Auxetic Origami Structures

The topology optimization method in Chapter 4 could also be applied to optimize auxetic structures, like the Miura-Ori fold pattern.

Gillman et al. [26] introduced modal analysis in topology optimization to discover designs of in-plane auxetic structures, i.e. structures that exhibit negative Poisson's ratio. Therefore, in this case, the objective function is different from the one used in Chapter 3 and 4, since it must be formulated to match a given change in width ( $\Delta W^*$ ) under a compressive load.

The *optimization problem* is the following:

Find  $\boldsymbol{\alpha} = \alpha_1, \dots, \alpha_{N_f}$  that

Minimize  $f = (\Delta W_{avg} - \Delta W^*)^2$

Subject to

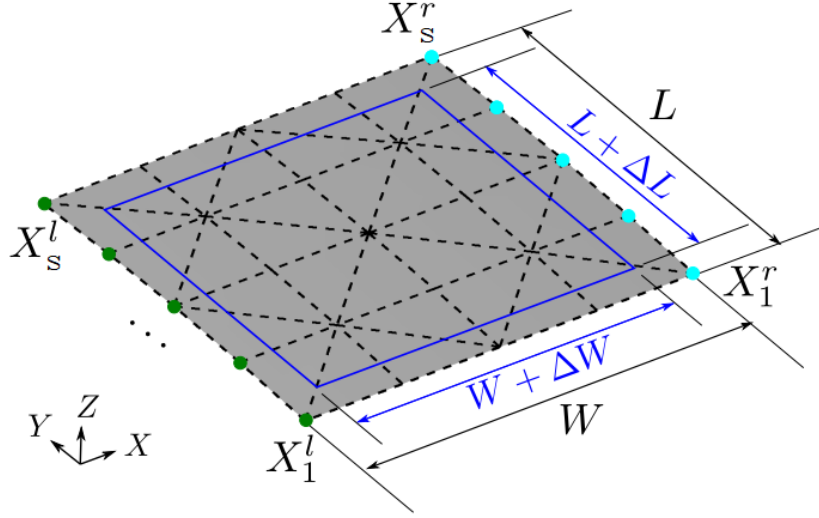
$$\begin{aligned} g_1 &= v_{0,1} - \frac{1}{N_f} \sum_{k=1}^{N_f} \alpha_k \leq 0; & (E.1) \\ 0 &\leq \alpha_k \leq 1; & \forall k = 1, \dots, N_f; \\ R_l(\mathbf{X}) &= 0; & u_l = X_l - X_l^0; & l = 1, \dots, 3N_{nodes}, \end{aligned}$$

$\Delta W_{avg}$  is the average change in width along the left and right sides of the

structure and it is defined as

$$\Delta W_{avg} = W - \frac{1}{N_f} [(X_1^r - X_1^l) + \dots + (X_s^r - X_s^l)], \quad (\text{E.2})$$

where  $N_s$  is the number of nodes along the left and right side, and  $X_s^r$  and  $X_s^l$  are the right and left positions of the nodes along the right and left sides, represented as cyan and green dots respectively in Fig. E.1.



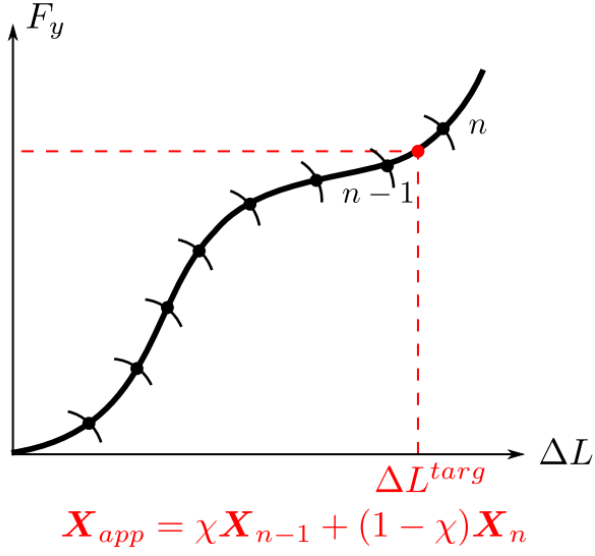
**Figure E.1:** Parameters for the Optimization framework [26].

Taking into account Fig. E.2, the amount of compression along the direction of actuation  $Y$  needs to match a prescribed actuation  $\Delta L^{targ}$ . In order to do so, the compression is controlled by the arc-length method in Section C at each loading step. When  $\Delta L^{targ}$  is exceeded, the configuration  $\mathbf{X}$  is approximated based on the current and previous loading step (namely  $n$  and  $n - 1$ ) as

$$\mathbf{X}_{app} = \chi \mathbf{X}_{n-1} + (1 - \chi) \mathbf{X}_n, \quad (\text{E.3})$$

which is a linear interpolation, with

$$\chi = \frac{\Delta L^{targ} - \Delta L^{n-1}}{\Delta L^n - \Delta L^{n-1}}. \quad (\text{E.4})$$

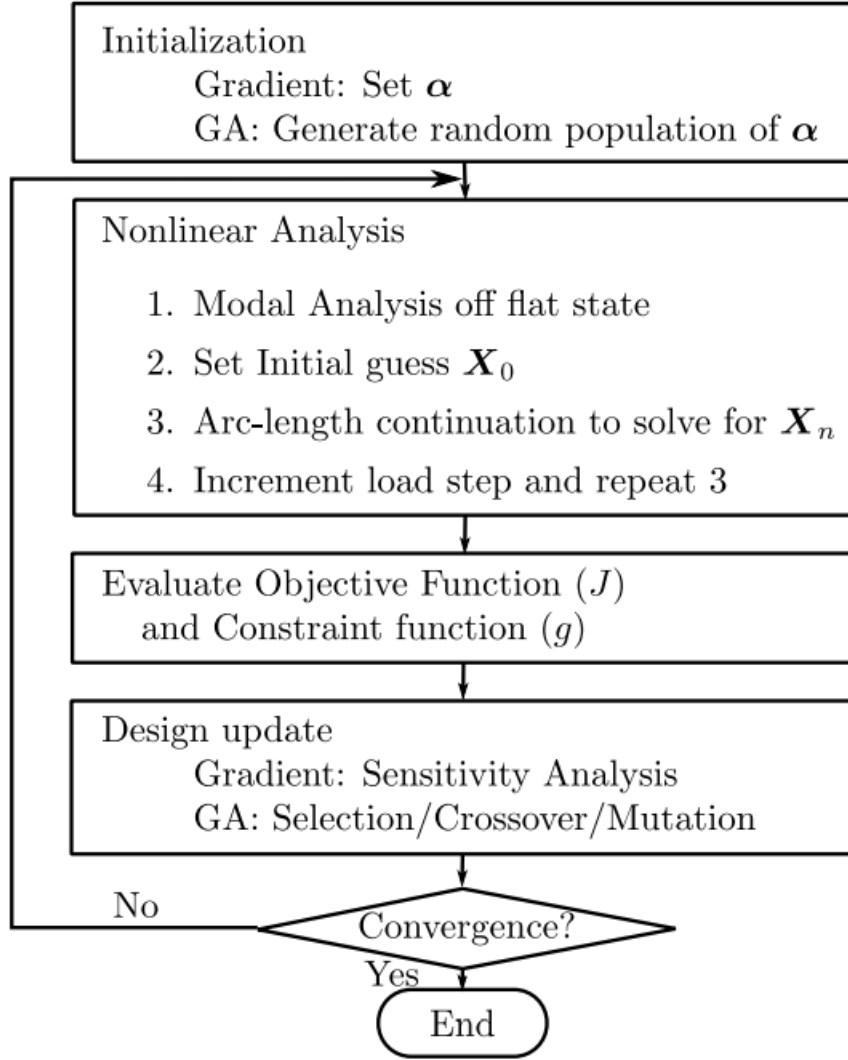


**Figure E.2:** Interpolation of the solution between arc-length steps [26].

The capabilities of this method can be assessed using both a gradient-based optimization and a Genetic Algorithm. Fig. E.3 shows the flowchart of the optimization process.

Lastly, to add axial rigidity  $EA$  as a variable, it is necessary to introduce a second constraint function and the design variable vector  $\mathbf{x}$ , that includes both the fold stiffness exponent ( $\boldsymbol{\alpha}$ ) and the axial rigidity density ( $\boldsymbol{\beta}$ ), analogously to the proceeding in Chapter 4.

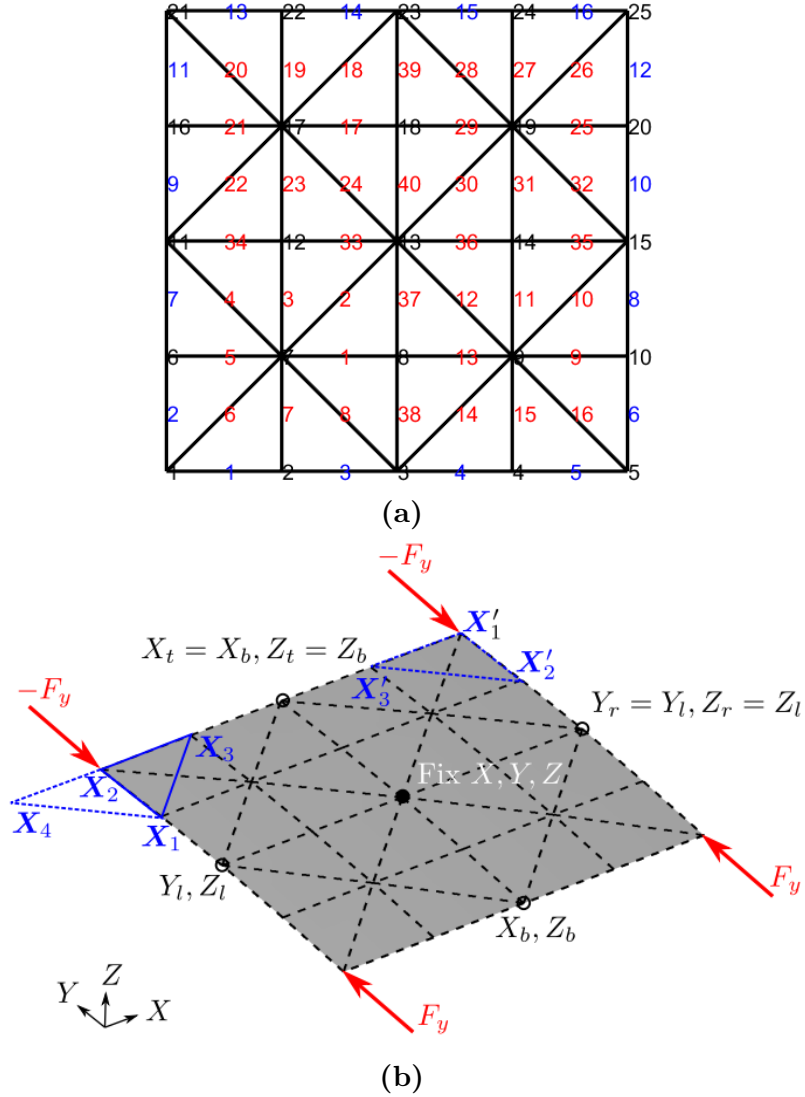
To conclude, the following example provides a brief demonstration of the functionality of the described optimization process on the Miura-Ori fold pattern.



**Figure E.3:** Flowchart of the optimization process for a gradient-based optimization and the Genetic Algorithm [26].

### Miura-Ori, Auxetic Fold Pattern

The starting configuration in Fig. E.4a presents the load and boundary conditions in Fig. E.4b. The node positions in blue are the periodic nodes defined in Section B, the central node is fixed, the position of the nodes in the center of the left and right side along  $Y$  and  $Z$  are constrained to move together, thus  $Y_r - Y_l = 0$  and  $Z_r - Z_l = 0$ , and likewise the position of the nodes in the center of the top and bottom side along  $X$  and  $Z$ , thus  $X_t - X_b = 0$  and  $Z_t - Z_b = 0$ .

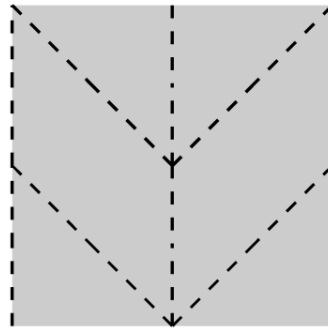


**Figure E.4:** Starting configuration. (a) Reference grid; (b) Load and boundary conditions ( $F = 10^6$  N,  $EA/G_{soft} = 10^6$  and  $EA/G_{stiff} = 10^1$ ) [26].

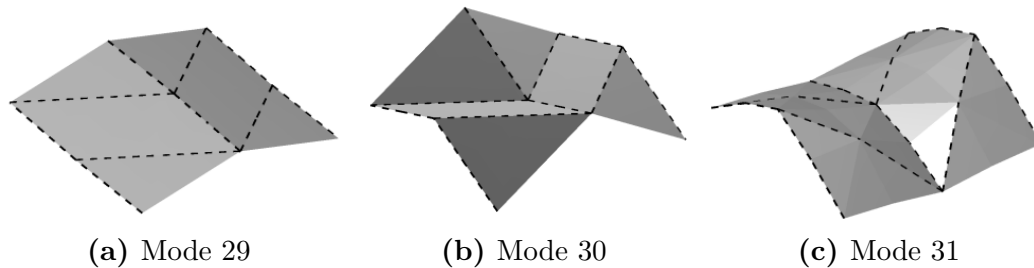
The problem has 40 internal fold lines and 16 periodic boundary fold lines, of which only 8 are unique. Therefore, the total number of design variables is 48.

Fig. E.6 shows the results of the modal analysis as described in Section D, starting from a fold pattern similar to the Miura-Ori (depicted in Fig E.5).





**Figure E.5:** Initial fold pattern for the modal analysis [26].



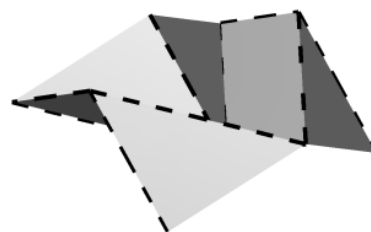
(a) Mode 29

(b) Mode 30

(c) Mode 31

**Figure E.6:** Modal analysis for the fold pattern in Fig. E.5 [26].

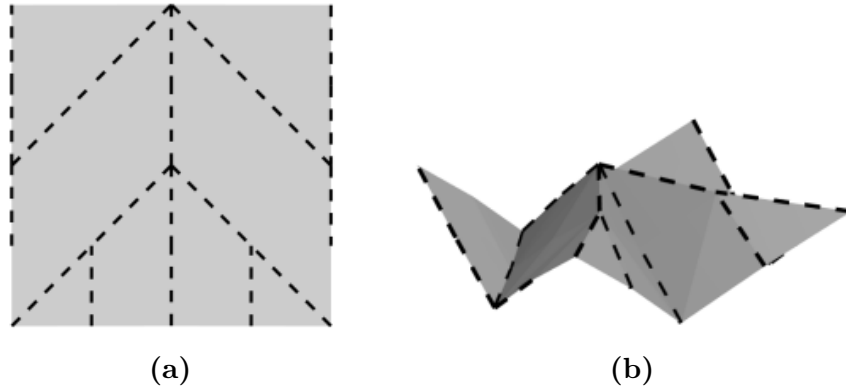
Considering the first three positive modes (mode 29, 30 and 31) it can be noted that mode 30 resembles the Miura-Ori fold pattern. Therefore, since the objective of this optimization is to discover auxetic structures, mode 30 is selected as the initial guess ( $\mathbf{X}_0$ ) to undergo the process introduced in Section D.



**Figure E.7:** Nonlinear actuation of mode 30 [26].

To limit the complexity of the problem, a symmetric solution is assumed about the  $Y$  axis. The design variables are thus reduced to 28, i.e. 22 for the internal and 6 for the periodic fold lines.

Using the SQP method, the starting configuration in Fig. E.4 does not discover the Miura-Ori fold pattern, and the resulting optimized crease pattern is symmetric along the  $X$  and  $Y$  direction. From Fig. E.8 it can be noted that the GA introduces asymmetry along the  $Y$  direction and discovers a Miura-Ori fold pattern.



**Figure E.8:** Miura-Ori auxetic design discovered with the described optimization method based on the Genetic Algorithm [26].

With this design, if the axial compressive actuation is set to  $\Delta L^{targ} = -0.033$  and the target in-plane compression is set to  $\Delta W^* = -0.0497$ , the resulting Poisson's ratio is  $-1.5$ , therefore an origami pattern with auxetic behavior is discovered.

Lastly, it would be of interest to study the effect of the addition of axial rigidity as a design variable in the described optimization process based on GA. This modification could lead to the discovery of the Miura-Ori fold pattern for lower compressive loads since the structure is allowed to be more flexible, or to slightly different crease patterns that still achieve the targeted auxetic behavior.